CIAMTIS

U.S. DOT Region 3 University Transportation Center

Optimized Performance of UHPC Bridge Joints and Overlays

March 18, 2022

Prepared by:

T. Dennis, D. Sundar, E. Chinaka, M. Gac, M. Head, F. Rajapibour, and P. Mondal

r3utc.psu.edu

PennState College of Engineering

LARSON TRANSPORTATION INSTITUTE

Technical Report Documentation Page

1. Report No.	2. Government Accession No.	3. Recipient's Catalog No.
CIAM-UTC-REG4		

4. Title and Subtitle Optimized Performance of UHPC Bridge Joints and Overlays	**5. Report Date** March 18, 2022 **6. Performing Organization Code**
7. Author(s) Tyler Dennis, Deepika Sundar, Emmanuel Chinaka, Madison Gac, Monique Head, Farshad Rajapibour, and Paramita Mondal	**8. Performing Organization Report No.**
9. Performing Organization Name and Address University of Delaware 127 The Green Newark, DE 19716 The Pennsylvania State University 201 Old Main University Park, PA 16802	**10. Work Unit No. (TRAIS)** **11. Contract or Grant No.** 69A3551847103
12. Sponsoring Agency Name and Address U.S. Department of Transportation Research and Innovative Technology Administration 3rd Fl, East Bldg E33-461 1200 New Jersey Ave, SE Washington, DC 20590	**13. Type of Report and Period Covered** Final Report 03/18/2019 – 03/18/2021 **14. Sponsoring Agency Code**

15. Supplementary Notes

Work funded through The Pennsylvania State University through the University Transportation Center Grant Agreement, Grant No. 69A3551847103.

16. Abstract

The use of ultra-high-performance concrete (UHPC) for connections between prefabricated bridge elements (i.e., bridge deck panels) offers fast construction and increased durability and is gaining momentum across the United States. In addition, UHPC overlays can be used for effectively repairing deteriorating concrete bridge decks. UHPC offers significant advantages over conventional concrete, both short and long term. For example, the self-flowing nature of UHPC allows proper filling of formwork that has closely spaced reinforcement, and its quick strength gain allows rapid construction. Durability of UHPC increases due to the impermeable nature of UHPC, which reduces the ingress of water and soluble salts into concrete. Better bonding between UHPC and other elements due to very low shrinkage and creep, and improved crack resistance due to higher fracture toughness, offer increased structural integrity over conventional material. Given the proprietary nature and higher material cost of UHPC compared to conventional concrete, there is a need to better understand the constituent materials to develop more cost-effective mix designs using locally sourced materials while also redesigning the mixture according to the structural performance desired. This research focuses on an integrated structural-material design process to understand these relationships and at what cost while addressing issues at the joint interface related to bond strength and load-slip behavior.

17. Key Words	**18. Distribution Statement**
Ultra-high-performance concrete (UHPC), mix design, fresh and hardened properties, structural performance, durability, bridge joints and overlays	No restrictions. This document is available from the National Technical Information Service, Springfield, VA 22161

19. Security Classif. (of this report)	20. Security Classif. (of this page)	21. No. of Pages	22. Price
Unclassified	Unclassified	101	

Form DOT F 1700.7 **(8-72)** **Reproduction of completed page authorized**

DISCLAIMER

The contents of this report reflect the views of the authors, who are responsible for the facts and the accuracy of the information presented herein. This document is disseminated in the interest of information exchange. The report is funded, partially or entirely, by a grant from the U.S. Department of Transportation's University Transportation Centers Program. However, the U.S. Government assumes no liability for the contents or use thereof.

Table of Contents

1.1 BACKGROUND **1**
1.2 OBJECTIVES **3**
1.3 LITERATURE REVIEW **4**
1.3.1 Preceding UHPC Research 4
1.3.2 Distribution of UHPC Bridge Applications in the United States 4
1.3.3 Composition of UHPC for Bridge Connections and Overlays 7
1.3.4 Standard UHPC Bridge Connection Types 7
1.3.4.1 Link Slab Connection 8
1.3.4.2 Longitudinal Element Connection 8
1.3.4.3 Deck Panel Connection 9
1.3.5 Mixture Proportioning for UHPC 10
1.3.5.1 Materials 10
1.3.5.2 Fine and Coarse Aggregate 13
1.3.5.3 Fibers 13
1.3.5.4 Water/Binder Ratio and Superplasticizers 14
1.3.6 Fresh Properties 16
1.3.6.1 Rheology 16
1.3.6.2 Curing 17
1.3.7 Hardened properties 18
1.3.7.1 Compressive strength 18
1.3.7.2 Tensile strength 18
1.3.8 Experimental Testing 21
1.3.9 High-Performance Concrete 23
2.1 MATERIALS AND METHODS **24**
2.1.1 Binder Components 24
2.1.2 Sand 25
2.1.3 Chemical Admixtures 26
2.1.4 Fiber 26
2.1.5 Mix Design 27
2.1.5.1 Statistical modeling and selection of mixture 27
2.1.5.2 Particle packing models to select the mix design 30
2.1.5.3 Final UHPC Mix design adopted 31
2.1.6 Mixing Procedure 32
2.1.7 Fresh Property Assessment 34
2.1.7.1 Workability 34
2.1.7.2 Fresh air content and setting time 35
2.2 FLEXURAL BOND STRENGTH TESTS **36**

2.2.1 Four-Point Testing 36
2.2.2 Results 37
2.3 COMPRESSIVE STRENGTH TESTS 41
2.4 TENSILE STRENGTH TESTS 47
2.4.1 Direct Tensile Assessment 47
2.4.2 Prism Third-Point Bending Tests 48
2.4.3 Equivalent Bending Stress Versus Midspan Deflection Results 49
2.5 REBAR PULL-OUT TESTS 52
2.5.1 Reinforcement Uniaxial Tensile Testing 52
2.5.2 Analysis of Results 57
3.1 SUMMARY OF EXPERIMENTAL TEST RESULTS 62
3.1.1 Fresh property characterization at Penn State 62
3.1.2 Tensile strength and dispersion of fibers in the cross-section 66
3.2 FINITE ELEMENT MODELING OF UHPC BRIDGE CONNECTION 68
3.2.1 Background 68
3.2.2 Model Development 68
3.2.3 Geometry 69
3.2.4 Material Properties and Models 71
3.2.4.1 Concrete Modeling 71
3.2.4.2 Steel Rebar Modeling 72
3.2.5 Contact Models 72
3.2.6 Loading 73
3.2.7 Meshing and Elements 73
3.2.8 Model Validation 74
3.2.9 Results and Discussion 76
3.3 LIFE CYCLE COST ANALYSIS 80
3.3.1 Overview 80
3.3.2 RealCost Software 80
3.3.2.1 Software Overview 80
3.3.2.2 Input Parameters 80
3.3.2.2.1 Project-Level Inputs 80
3.3.2.2.2 Alternative-Level Inputs 81
3.3.3 Results 82
3.3.4 Discussion 84
3.3.5 Summary and Future Work 85

4 RECOMMENDATIONS 86
REFERENCES 87

List of Figures

Figure 1. Categories of bridge surface area in m^2 (by NBI condition rating) (FHWA, 2018) ... 2
Figure 2. National distribution of UHPC bridge infrastructure projects from 2006-2018 ... 5
Figure 3a. National distribution of UHPC bridge infrastructure projects by application category ... 6
Figure 3b. National distribution of UHPC bridge infrastructure projects by region ... 6
Figure 4. UHPC bridge infrastructure projects by superstructure type in the Mid-Atlantic U.S ... 6
Figure 5. UHPC bridge infrastructure projects by span in the Mid-Atlantic U.S. ... 7
Figure 6. UHPC bridge infrastructure application by type of connection in the Mid-Atlantic U.S ... 8
Figure 7. Particle size and specific area of concrete materials (Shi et al. 2015) ... 11
Figure 8. Comparison of some formulations for NSC, SCC and various UHPCs (Fehling et al. 2014) ... 12
Figure 9. Profiles of steel fibers commonly used in UHPFRC (Katzer 2006) ... 13
Figure 10. Some common types of steel fibers (Graybeal 2018 and Lee et al. 2018) ... 14
Figure 11. (a) Mini-slump cone and (b) mini-slump flow of pastes with differing binder combinations (Azmee and Shafiq 2018) ... 15
Figure 12. A typical mini slump cone (dimensions in mm) (reproduced after [18]) ... 15
Figure 13. Flow table results for thixotropic and non-thixotropic UHPC mixtures ... 16
Figure 14. Slope test as per SIA 2052 (Bruhwiler 2016a) (ASTM C1856 2017) ... 16
Figure 15. Bingham plastic model ... 17
Figure 16. Contec® 5 coaxial viscometer (Feys and Khayat 2015) ... 17
Figure 17. Schematic of direct tension test (Graybeal, 2018) ... 19
Figure 18. Uniaxial tensile response for UHPC (Graybeal, 2018) ... 20
Figure 19. 4-point bending prism test of UHPC ... 20
Figure 20. Particle size distribution of the silica fume, cement and supplemental material used ... 24
Figure 21. Grain size distributions of the sand used ... 26
Figure 22. High shear mixer used for mixing UHPC ... 32
Figure 23. Static spread diameter of UHPC ... 34
Figure 24. Standard filling procedure of brass flow table prior to the measuring UHPC spread ... 35
Figure 25. Measuring UHPC spread during flow test ... 36
Figure 26. Plot of flexural strength vs retarder duration ... 39
Figure 27. Plot of flexural strength vs bond age ... 40
Figure 28. Dimension of steel rings ... 40
Figure 29. Image of dual ring test ... 41
Figure 30. UHPC specimens prepared on the sanding belt prior to testing ... 42
Figure 31. Lab procedure to determine suitability of UHPC cylinders using a level and speed square layout tool ... 42
Figure 32. Cylinder compressive test results for 4-2-21 proprietary UHPC mix ... 44
Figure 33. Cube compressive test results for 4-2-21 proprietary UHPC mix ... 44
Figure 34. Cylinder compressive test results for 5-3-21 proprietary UHPC mix ... 45

Figure 35. Cube compressive test results for 5-3-21 proprietary UHPC mix 45
Figure 36. Cube compressive results for 6-3-21 proprietary UHPC mix used in pull-out tests........ 46
Figure 37. Cylinder compressive results for 6-8-21 non-proprietary UHPC mix used in pull-out tests........ 46
Figure 38. Cube compressive results for 6-8-21 non-proprietary UHPC mix used in pull-out tests........ 47
Figure 39. Direct tension test specimens designed 48
Figure 40. Third-point bending test on Instron Testing Machine with two uniaxial strain gauges at midspan 49
Figure 41. Third-point bending tests for 4-2-21 proprietary UHPC mix 50
Figure 42. Third-point bending tests for 5-3-21 proprietary UHPC mix 50
Figure 43. Third-point bending test for 6-3-21 proprietary UHPC mix........ 51
Figure 44. Third-point bending tests for 6-8-21 non-proprietary UHPC mix........ 51
Figure 45. Completed prism test with crack occurring in the middle third of the specimen 52
Figure 46. Uniaxial tensile stress versus strain for the epoxy-coated and uncoated rebar........ 53
Figure 47. Rebar pull-out test setup 54
Figure 48. Stress versus slip response from the non-proprietary coated rebar pullout tests 55
Figure 49. Stress versus slip response from the non-proprietary uncoated rebar pullout tests 55
Figure 50. Stress versus slip response from the proprietary coated rebar pullout tests........ 56
Figure 51. Stress versus slip response from the proprietary uncoated rebar pullout tests........ 56
Figure 52. Peak bar axial stress for all epoxy-coated rebar pull-out tests........ 58
Figure 53. Peak bar axial stress for all uncoated rebar pull-out tests........ 59
Figure 54. Bar-UHPC bond strength for all epoxy-coated rebar pull-out tests........ 59
Figure 55. Bar-UHPC bond strength for all uncoated rebar pull-out tests........ 60
Figure 56. Stress versus slip response for all epoxy-coated rebar pullout tests 60
Figure 57. Stress versus slip response for all uncoated rebar pullout tests 61
Figure 58. Particle size distributions of the target UHPC mix from modified A&A model and designed UHPC mix (R2 calculated to be 98%) 63
Figure 59. Effect of superplasticizer dosage on spread........ 64
Figure 60. Effect of SP dosage on 24-hour compressive strength 64
Figure 61. Compressive strength development of non-proprietary UHPC over time (measured on 2” cube specimens) 65
Figure 62. (a) Original image taken from the cross-section of the sliced UHPC prism, (b) Image after segmentation, highlighting the fiber in yellow and the rest of the matrix unaltered, and (c) Binary image considering the fiber as white and the rest of the matrix as black 67
Figure 63. Physical lab testing setup of the UHPC connection tests (Haber and Graybeal, 2018) 68
Figure 64. Physical UHPC connection specimen detail used in ABAQUS model (Haber and Graybeal, 2018)........ 69
Figure 65. Loaded third-point bending model in ABAQUS........ 73
Figure 66. Meshing used in ABAQUS model 74
Figure 67. Deflection at the zeroth-increment of the time loading history 75
Figure 68. Deflection at the fifteenth-increment of the time loading history........ 75
Figure 69. Deflection at the thirtieth-increment of the time loading history 75
Figure 70. Third-point loading diagram of a simply supported beam with two equally concentrated loads placed symmetrically (Hibbeler 2017)........ 77

Figure 71. Applied moment versus mid-span displacement for the ABAQUS finite element model with comparison to the physically conducted lab tests by Haber and Graybeal (Haber and Graybeal, 2018) 78
Figure 72. Concrete tensile cracking patterns in the ABAQUS finite element model 79
Figure 73. Tensile crack patterns observed from physical test specimens (Haber and Graybeal, 2018) 79
Figure 74. Agency and user cost for different alternatives 83
Figure 75. Agency and user cost probabilities for each alternative 84

List of Tables

Table 1. Estimated service life of conventional bridge deck overlays (Krauss et al. 2009)........................ 3
Table 2. Typical properties of field cast UHPC 10
Table 3. Typical UHPC non-proprietary mix constituents.. 11
Table 4. Influence of specimen size on compressive strength of UHPC (Wille et al. 2011) 18
Table 5. Dimensions of beams for measuring flexural strength.. 21
Table 6. Physical properties of the binder components.. 25
Table 7. Chemical parameters of the cement and silica fume used in this study 25
Table 8. Bogue's composition of the ASTM Type II cement 25
Table 9. Physical properties of the chemical admixtures 26
Table 10. Physical and mechanical properties of fiber used in this study................................. 27
Table 11. Summary of proportions from the 169 non-proprietary UHPC mixtures 28
Table 12. Conversion factors for the compressive strength of UHPC to that measured using a 3”x6” cylinder (Abbas et al., 2016) 29
Table 13. Analysis of variance table of the predictors chosen in the model 29
Table 14. Estimated regression coefficients of the linear model... 30
Table 15. Range of independent variables used in mix.. 30
Table 16. Adopted UHPC mix design... 32
Table 17. UHPC Mix sequence suggested in select published studies 33
Table 18. Average spread for the proprietary and non-proprietary UHPC mixes tested 35
Table 19. Failure stress and type of failure 38
Table 20. Flexural strength progression with increase in the bond age of the concrete............ 39
Table 21. Average compressive strength (psi) results for the proprietary UHPC mixes 43
Table 22. Average compressive strength (psi) results for the non-proprietary UHPC mix 43
Table 23. Failure mode, peak bar axial stress, and bond strength for the epoxy-coated rebar pull-out tests.. 57
Table 24. Failure mode, peak bar axial stress, and bond strength for uncoated rebar pull-out tests... 58
Table 25. Summary of measured fresh properties of non-prop. UHPC PSU mix 1.................. 65
Table 26. Summary of trial mixtures conducted at Penn State 66
Table 27. Geometric properties in millimeters used in the model for (a) precast regular concrete deck, (b) UHPC connection, (c) M16 (#5) longitudinal lap-splice rebar, and (d) M13 (#4) transverse rebar (Haber and Graybeal, 2018) 70
Table 28. UHPC connection geometry used in ABAQUS model (Haber and Graybeal, 2018)................ 70
Table 29. Regular concrete properties used in the model with references 71
Table 30. UHPC properties used in the model... 71
Table 31. Concrete damage plasticity parameters used in the model 72
Table 32. Steel reinforcement properties 72
Table 33. Summary of results from ultimate loading between the physical specimen and the finite element model 76
Table 34. Agency and user cost for different alternatives... 82
Table 35. Agency and user cost statistical data for different alternatives 83

Chapter 1

Introduction

1.1 BACKGROUND

The use of ultra-high-performance concrete (UHPC) has grown in popularity with widespread applications since it was made commercially available in 2000, improving rehabilitation, strengthening of pre-existing structures and components (Paper 2012), and even new construction using accelerated bridge construction (ABC) techniques. Ultra-high-performance concrete is a next-level material that has superior material properties and is stronger than high-performance concrete (HPC) and normal-weight concrete (NWC). UHPC exhibits greater compression and tensile strength as well as greater ductility (Graybeal 2014), thereby resulting in a compressive strength of 190 MPa, tensile strength of 9 MPa and elastic modulus of 52 GPa. UHPC also supports a longer service life in bridge construction due to the components of the UHPC mix. Chemical admixtures such as accelerator, superplasticizer, fly ash, and silica fumes are components that contribute to the performance of UHPC. The fibers inserted into the UHPC mix, commonly steel fibers, provide the flexural and tensile properties that make UHPC a superior material. UHPC contains a high volume of fiber reinforcement and a water-to-cement ratio that is below 0.25. Fine aggregates are often not present in the UHPC mix, unlike the other concrete mixes.

The use of higher-performing concrete is emerging in bridge repair and as connection elements. The higher quality and durability of the material allows for a better performance from the bridge component compared to previous conventional methods as well as speedier construction via prefabricated bridge elements and systems (PBES). Bridge decks in the United States require frequent repair and patchwork for serviceability. A recent estimate puts the cost annually incurred for bridge deck repair at 80% of total bridge maintenance related expenditure (Wibowo and Sritharan 2018). For instance, a study from the Minnesota DOT determined that for maintaining a National Bridge Inventory (NBI) deck condition rating of at least 4 (corresponding to an FHWA condition rating of “poor”), less than 10% of the deck surface area must be in poor condition (Haber et al. 2017). By recent estimates, more than 50% of the bridge deck areas in the United States are in less than “good” condition (shown in Figure 1), and the deterioration is liable to worsen unless intervention is carried out.

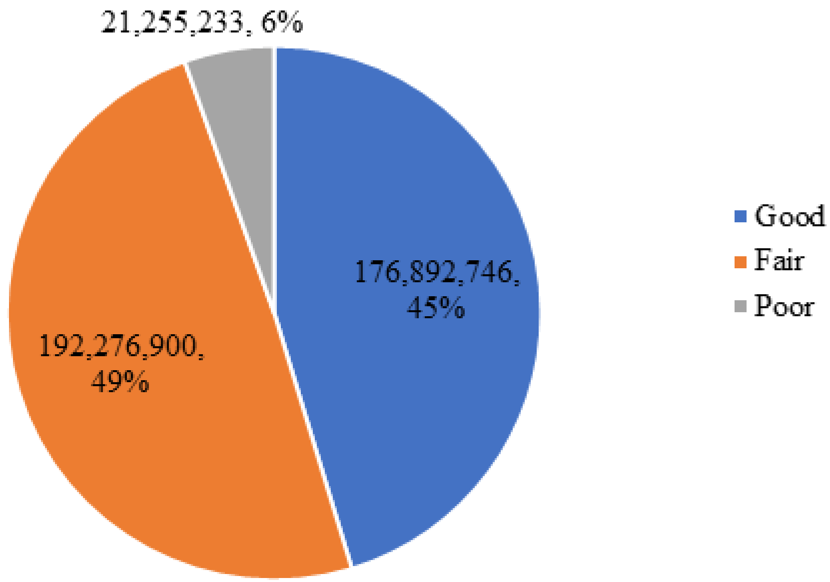

Figure 1. Categories of bridge surface area in m² (by NBI condition rating) (FHWA, 2018).

The use of UHPC for connections between bridge deck panels offers fast construction and increased durability and is gaining momentum across the United States. In addition, UHPC overlays can be used for effectively repairing deteriorating concrete bridge decks. UHPC offers significant advantages over conventional concrete, both short and long term (Graybeal 2006, Russell and Graybeal 2013). For example, the self-flowing nature of UHPC allows proper filling of formwork that has closely spaced reinforcement, and its quick strength gain allows rapid construction. Durability increases due to the impermeable nature of UHPC that reduces the ingress of water and soluble salts into concrete. Better bonding between UHPC and other elements due to very low shrinkage and creep, and improved crack resistance due to higher fracture toughness, offers increased structural integrity over conventional material.

Bridge expansion joints play a vital role in allowing for expansion and contraction between decks due to thermal loads, shrinkage, and longitudinal movement from traffic loads and even dynamic impact. Joints in traditional deck construction are often the weak links, as conventional materials used in joints like cement or epoxy grout are prone to (1) debonding from precast deck elements, and (2) cracking over time due to operational load, differential shrinkage and creep, and ingress of deicing salts due to their porous nature. Many bridges have "leaky joints," due to deicing salts and other liquids that flow through the joint and cause other structural components like steel bearings and girder ends to deteriorate over time. While some transportation agencies are moving toward jointless bridges for short, simple-span bridges, there is still a need to provide adequate repair solutions for multi-span bridges where joints are unavoidable and sustainable solutions are needed. With the advent of and push for more accelerated bridge construction (ABC) to minimize traffic delays due to construction, the use of UHPC, particularly to adjoin precast bridge elements, can aid in the overall durability of the system, given its durability and relative ease of installation. UHPC joints offer an attractive alternative for transportation agencies if a non-proprietary mix design can be provided for use between bridge decks (Graybeal 2012).

Traditional overlay technologies have a variety of drawbacks, including poor service life (for asphalt overlays, polymer overlays, silica fume concrete, and low-slump dense concrete overlays), significant increase in dead load (for all concrete overlays), more construction time and hence increased user cost (for concrete overlays), and high cost (for polymer-modified or silica fume concrete overlays) (Russell and Graybeal 2013). UHPC overlays have the potential to address some of these issues. Research on UHPC overlays has shown that they can provide high strength, high stiffness, low permeability, low shrinkage, smaller crack widths (due to fiber reinforcement), and good bonding with the substrate concrete bridge deck (Graybeal 2006, Shann 2012, Haber et al. 2017). The combination of high strength, stiffness, and durability also reduces the required thickness of the overlay, thus reducing the dead load (Haber et al. 2017). Practical applications of UHPC overlays have been demonstrated with good success (Haber et al. 2017).

Possible options for overlays include asphalt concrete, latex-modified concrete, and low-slump concrete overlays. While the above-mentioned overlays are still widely used, they tend to deteriorate rapidly over time. The table below gives the average service life range and mean service life for commonly used overlays.

Table 1. Estimated service life of conventional bridge deck overlays (Krauss et al. 2009).

Overlay Technique	Expected Service Life Range [mean] (years)	Overlay Thickness Range [mean] (inches)
High performance concrete overlays	10–40 [16–29]	1–5 [1.6–3.5]
Low slump concrete overlays	10–45 [16–32]	1.5–4 [2.0–3.1]
Latex-modified concrete overlays	10–50 [14–29]	1–5 [1.5–2.7]
Asphalt overlays with a membrane	3–40 [12–19]	1.5–4 [2.4–3.1]
Miscellaneous asphalt overlays	5–20 [8–15]	0.38–2.5 [0.8–1.5]
Polymer overlays	1–35 [9–18]	0.13–6 [0.5–1.4]

In comparison with UHPC, conventional concrete overlays tend to be thicker and increase the dead load of the bridge deck. UHPC could be a viable alternative for an overlay, as it allows construction of thinner (1-2” thickness) [4] overlays, which tend to be lightweight. Some estimates put the service life of UHPC structures at twice that of standard, normal-strength concrete (NSC)[5].

Despite the advantages, there are a few serious drawbacks that make construction with UHPC challenging. The main issue related to use of UHPC, for both joints and overlays, is the associated material cost (Newtson and Weldon 2018). Proprietary mixtures are available commercially, but they are costly. Various researchers have proposed non-proprietary UHPC formulations, and these have shown varying levels of success (El-Tawil et al. 2016; Wille and Boisvert-Cotulio 2013). In addition to cost, the rheology and workability of UHPC mixtures may pose constructability challenges for highly reinforced prefabricated bridge connections, due to the high fiber content of UHPC mixtures. Furthermore, it is expected that a properly bonded joint made with UHPC will change the load transfer and deflection characteristics of the structure due to its high strength and stiffness. It is necessary to understand this interaction to exploit the advantages of UHPC to the fullest, and also for redesigning the mixture according to the exact structural performance needed. This project focuses on an integrated structural-material design process to optimize a new UHPC mixture design to deliver the required mechanical and durability performance at a minimum cost.

1.2 OBJECTIVES

The objectives of this research are to: (1) synthesize existing knowledge from the literature regarding various UHPC mix designs and material properties, (2) establish empirical composition-property relationships that can be used to develop UHPC mix designs for joints and overlays based on fresh and hardened properties, (3) evaluate structural performance and durability of laboratory-scale specimens based on the integrated structural-material design approach, and (4) calibrate finite element models based on experimental test results to understand the impact of bond strength and materials properties, especially using locally sourced constituents on the ultimate moment capacity. The results from this work are expected to address a knowledge gap of linking formulation and rheology of UHPC mixtures with different fiber types, which allow the designing of highly flowable mixtures, to evaluate the optimum UHPC mixtures using locally sourced ingredients selected. Potential impact on the state of practice could be significant by promoting the use of low-cost, non-proprietary UHPC to extend the life of concrete bridges, and by familiarizing the industry and transportation agencies in the region with this valuable technology.

1.3 LITERATURE REVIEW

1.3.1 Preceding UHPC Research

Ultra-high-performance concrete is an innovative cementitious mixture characterized by superior mechanical and durability properties to that of conventional concrete. UHPC has a discontinuous pore structure that reduces liquid ingress, significantly enhancing durability compared to conventional concrete. Substantial improvements in concrete technology have led to advancing the research and use of UHPC starting with Canada in the 1990s and later in the United States in the 2000s. With structural design parameters and standards varying between countries, numerous definitions regarding the range of strength and durability characteristics have been reported for UHPC (Crane et al. 2019).

The basis for UHPC's exceptional mechanical properties can be attributed to three main principles: homogeneity, density, and ductility (ACI Committee 239 2018). Homogeneity in the UHPC mix is obtained through using materials with smaller particle sizes that allow for better dispersion when mixing. The consistency of the hardened and fresh properties throughout the entire mix is improved and thus the overall performance of the mix is better distributed (Graybeal et al. 2019). Through optimized gradation of the UHPC matrix constituents, the particle packing density of the mix is increased, which produces a material with a discontinuous pore structure. With smaller particles that are spaced more tightly, the voids in the matrix are more disconnected from one another, which leads to both the increase in strength and improved resistance to penetration. Another benefit from a more compact mix is that due to the increased number of contact points between the mixture constituents, the material better distributes stresses throughout the matrix (ACI Committee 239 2018). By the addition of steel fibers, increased ductility and a strain-hardening tensile behavior of the UHPC mix are obtained. These qualities are very beneficial for infrastructure applications because of the smaller stress-induced crack sizes, which results in increased durability and the ability of UHPC to carry higher tensile loads with a reduced amount of steel reinforcement (ACI Committee 239 2018).

Because of the beneficial qualities of UHPC, the Federal Highway Administration (FHWA) has taken particular interest in this material to address various aspects from accelerated bridge construction (ABC) to lifespan optimization of highway bridge infrastructure (Graybeal 2019). In addition to the FHWA, the American Concrete Institute (ACI) has noted the trend of UHPC in the United States and has formed ACI Committee 239 (2018), which focuses on reporting information and developing design guidelines for UHPC usage. Thus far, considerable research has been conducted to assess the material properties and constituents of UHPC (Russell and Graybeal 2013). Proprietary UHPC projects have been developed and used on many of the projects in the Mid-Atlantic United States. Coupled with understanding the mix design ratios, testing procedures and methods have been established to help standardize the way the material is characterized (ACI Committee 239 2018).

1.3.2 Distribution of UHPC Bridge Applications in the United States

Since the first United States UHPC project in 2006, there has been a steady increase in the number of highway bridge projects, with the largest jump in projects from 2017 to 2018 (FHWA 2018). Figure 2 shows the breakdown by year of all 199 UHPC bridge infrastructure projects from 2006 until 2018. From these projects, Figure 2 depicts the main categories of UHPC applications, with most highway infrastructure projects being heavily saturated on connections between bridge elements. The primary driving factor for this trend has been due to the advantages of UHPC on accelerating bridge construction. From approximately 2015 to 2018, the FHWA provided financial incentives through the EveryDay Counts (EDC) 3 and 4 Initiatives (EDC-3 and EDC-4) on various projects that have implemented UHPC to accelerate construction (FHWA 2018). Because of the promotion of the material by the FHWA, state agencies have been able to gain valuable construction and design experience with UHPC to further utilize the material on subsequent projects.

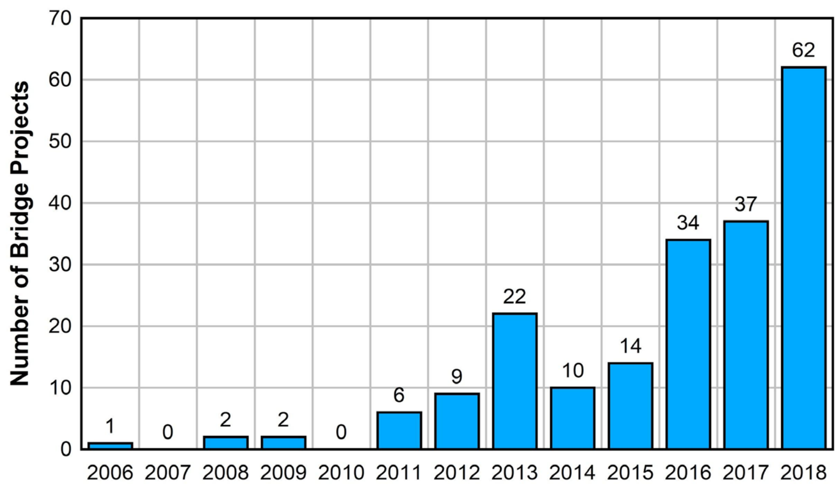

Figure 2. National distribution of UHPC bridge infrastructure projects from 2006-2018.

Geographically, UHPC bridge infrastructure projects have been heavily concentrated on the east coast of the United States, specifically in the Mid-Atlantic United States Region (New York, Pennsylvania, Delaware, District of Columbia, Maryland, Virginia, and West Virginia). The philosophy surrounding the use of UHPC has been on projects that emphasize the mechanical and durability advantages of the material. UHPC for the highway infrastructure sector has a vast appeal in the Mid-Atlantic Region largely due to the corrosive environments that exist from the onset of deicing salts and other intrusive chemicals. Figure 3 depicts the geographic distribution of all 199 projects, with the Mid-Atlantic Region accounting for approximately 57.8% (115) of the total projects and New York accounting for 38.2% (76) of the total (FHWA 2018). In the Mid-Atlantic Region, New York accounts for the majority of UHPC bridge projects where the primary superstructure type has been steel superstructure bridges (NBI 2019). Additionally, in the Mid-Atlantic Region, almost three-quarter of the bridges constructed or rehabilitated have been single-span bridges. Figures 4 and 5 show the breakdown of Mid-Atlantic bridge infrastructure projects by superstructure type and span, respectively.

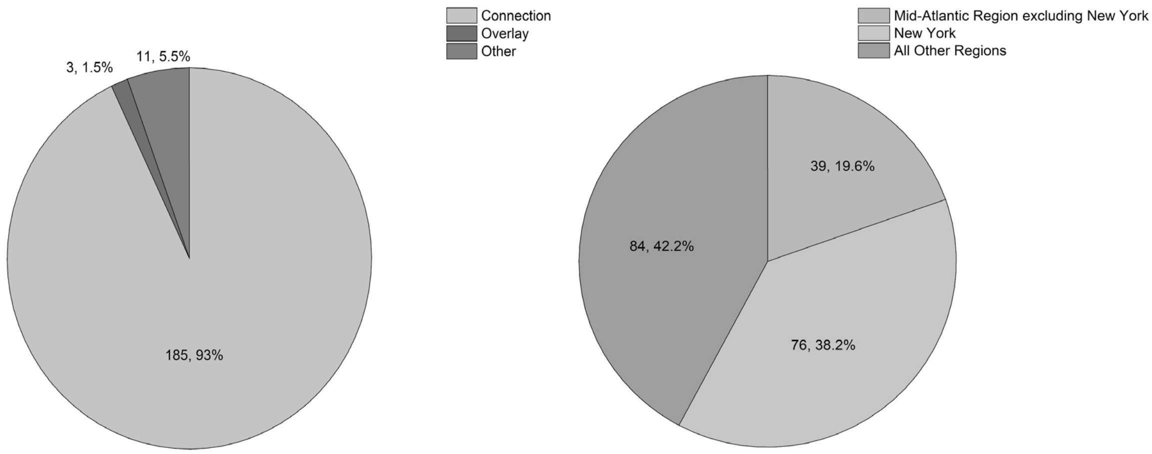

Figure

Figure 3. (a) National distribution of UHPC bridge infrastructure projects by application category; (b) National distribution of UHPC bridge infrastructure projects by region.

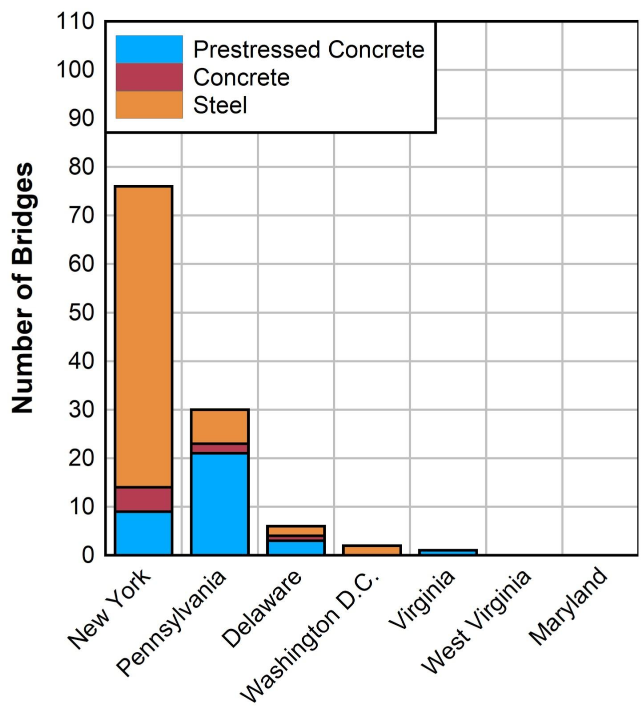

Figure 4. UHPC bridge infrastructure projects by superstructure type in the Mid-Atlantic United States.

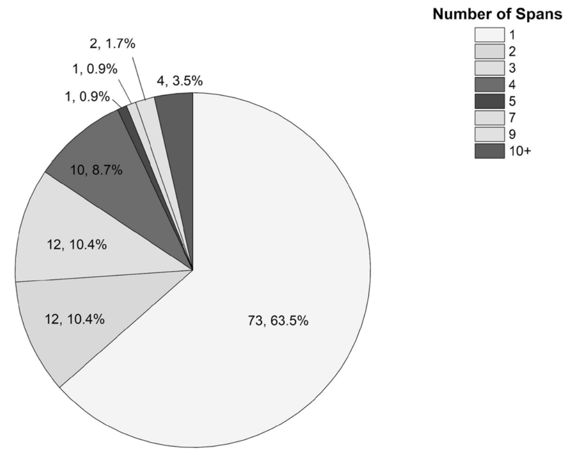

Figure 5. UHPC bridge infrastructure projects by span in the Mid-Atlantic United States.

1.3.3 Composition of UHPC for Bridge Connections and Overlays

In general, UHPC consists of portland cement, aggregate, admixtures, fibers, and water. While a universal definition of UHPC in the United States has yet to be formalized, the FHWA defines UHPC as a cementitious composite material with disconnected fiber reinforcement. The baseline material properties include a water-to-cementitious materials ratio less than 0.25, compressive strength greater than 21.7 kilopounds per square inch (ksi) (150 MPa), and sustained post-cracking tensile strength greater than 0.72 ksi (5 MPa) (Russell and Graybeal 2013). Given the makeup of bridge connections, it is important that the material can freely flow into the joint formwork and self-consolidate (Graybeal 2019). Dissimilar to UHPC mixes used in connections, the UHPC mixes used for overlays typically are not self-consolidating. Instead, these specific UHPC mixes are formulated to have modified rheological characteristics referred to as thixotropic properties. This class of UHPC does not freely flow under gravity and instead spreads when agitated to allow for proper profiling of roadways and screeding (Dean et al. 2019).

1.3.4 Standard UHPC Bridge Connection Types

Given the exceptional material properties when compared with conventional concrete, UHPC offers higher compressive and tensile strength, which leads to the simplification of joint details and increased ease of construction (Graybeal 2019). UHPC also offers an advantage as a wearing surface for bridge overlays due to its outstanding durability and impact resistance (ACI Committee 239 2018). Most of the UHPC bridge projects in the United States have consisted of the following typical connection configurations: (1) link slabs, (2) longitudinal superstructure element connections (Peruchini et al. 2017), and (3) adjacent deck connections (transverse and longitudinal) (FHWA 2018). Figure 6 shows the number of bridge projects in the Mid-Atlantic Region of the United States, including the specific designations as classified by the FHWA (2018).

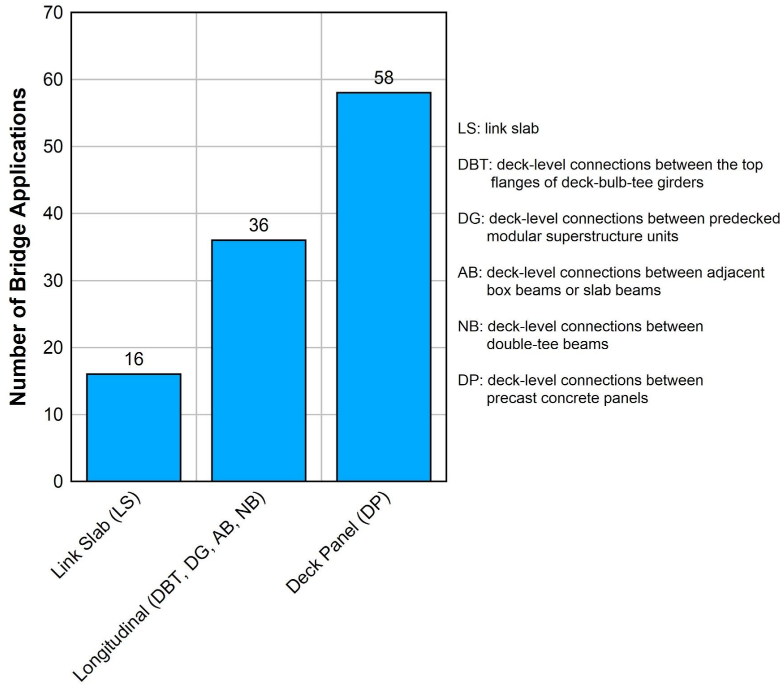

Figure 6. UHPC bridge infrastructure application by type of connection in the Mid-Atlantic United States.

1.3.4.1 Link Slab Connection

UHPC link slabs are connections located above the interior supports of multiple, simple-span bridges. In the majority of cases, link slabs can serve as a replacement for conventional expansion joints that are susceptible to the ingress of water and corrosive agents and result in eventual deterioration of bridge bearings, girders, and piers (Graybeal 2019). Link slabs usually involve lap sliced rebar and UHPC to connect two deck panels on either side of an interior support, effectively connecting two spans of the structure. Link slabs are designed to perform more similar to a semi-rigid, allowing for nominal rotation and longitudinal movement so that minimal internal stresses are transferred from one span to the next (Graybeal 2019). UHPC is also particularly well suited for this application due to the increased toughness and durability characteristics associated with the material, which allows for relatively less cracking and corrosive agent ingress compared to conventional concrete (Graybeal 2019). NYSDOT has been the leading agency in implementing this UHPC detail to decrease the excessive corrosion typically associated with leaky expansion joints, with other transportation agencies such as DelDOT recently adopting the design philosophy in 2018.

1.3.4.2 Longitudinal Element Connection

To connect superstructure segments more effectively, FHWA has developed design guidelines involving lap-spliced rebar extending from the longitudinal element and UHPC to facilitate connections (Graybeal 2019). Implementing this connection effectively creates a composite superstructure system in which moment, shear, and axial tensile and compressive forces are transferred across the connection and is commonly idealized as a continuously reinforced concrete slab at the top flange level (Graybeal 2019). When utilizing UHPC for this type of connection, most issues with differential deflection, cracking, and eventual connection failure associated with the typical procedure of transversely post-tensioning can be better avoided (Graybeal 2019).

1.3.4.3 Deck Panel Connection

UHPC is also commonly used as a rigid longitudinal and/or transverse connection material between two precast deck panels by using lap-spliced rebar connections with UHPC closures (Haber and Graybeal 2018). Due to the increased bond strength between the rebar and the UHPC compared to that of regular concrete, stress is better transferred between the deck components, rebar, and UHPC (Haber and Graybeal 2018). This in turn results in the increased strength development of the lap-spliced rebar over shorter lengths, effectively decreasing the required development length and joint geometry (ACI Committee 239 2018). The FHWA has published standardized details involving a female-female shear key configuration and deck roughened interfaces to promote enhanced bonding between components (Graybeal 2019). Researchers have evaluated the effect of appropriate conditions such as surface saturated dry (SSD) when placing UHPC adjacent to conventional concrete (Russell and Graybeal 2013). In most scenarios, connections usually range from 6 to 8 inches wide. The advantages of this type of UHPC connection primarily involve expeditiously connecting and constructing multiple precast deck elements.

Table 2. Typical properties of field cast UHPC.

Material Characteristic	Average Result
Density	155 lb/ft^3 (2,480 kg/m^3)
Compressive strength (ASTM C39; 28-day strength)	24 ksi (165 MPa)
Modulus of elasticity (ASTM C469; 28-day modulus)	7,000 ksi (48 GPa)
Direct tension cracking strength (uniaxial tension with multiple cracking)	1.2 ksi (8.5 MPa)
Split cylinder cracking strength (ASTM C496)	1.3 ksi (9.0 MPa)
Prism flexural cracking strength (ASTM C1018; 12 in (305-mm) span)	1.3 ksi (9.0 MPa)
Tensile strain capacity before crack localization and fiber debonding	> 0.003 m/m
Long-term creep coefficient (ASTM C512; 11.2 (77 MPa) load)	0.78
Long-term drying shrinkage (RH=50±4%, T=73±3°F(23±2°C)) (ASTM C157; initial reading after set)	555 με
Total shrinkage (embedded vibrating wire gage)	790 με
Coefficient of thermal expansion (AASHTO TP60-00)	8.2 x10^{-6} in/in/°F (14.7 x10^{-6} mm/mm/°C)
Chloride ion penetrability (ASTM C1202; 28-day test)	360 coulombs
Chloride ion penetrability (AASHTO T259; 0.5-in (12.7-mm) depth)	<0.10 lb/yd^3 (<0.06 kg/m^3)
Scaling resistance (ASTM C672)	No scaling
Abrasion resistance (ASTM C944 2x weight; ground surface)	0.026 oz. (0.73 g) lost
Freeze-thaw resistance (ASTM C666A/AASHTO T 161-17; 600 cycles)	RDM = 99 percent
Alkali-silica reactivity (with non-reactive aggregates)(ASTM C1260)	Innocuous

1.3.5 Mixture Proportioning for UHPC

1.3.5.1 Materials

A fresh UHPC formulation is composed of cementitious binders, aggregate, filler materials, and chemical admixtures, like conventional concrete. UHPC is not very different from OPC concrete regarding the type of ingredient materials, but rather the quantities used, as seen in Figures 7 and 8 below. A typical UHPC non-proprietary mix formulation is shown in Table 3. As seen in the table, a very high content of binder is typical of UHPC.

FHWA (Wille et al. 2014) suggests the following mix design (by weight) for UHPC:

- Cement:silica fume: SCM = 1.0 : 0.25 : 0.25
- Water to cement ratio: w/c = 0.2–0.3
- Aggregate: cement ratio = 1.0–2.0
- Fiber volume fraction = 1.0–2.0 percent

Table 3. Typical UHPC non-proprietary mix constituents.

Material	lb/yd³	Percent by Weight
Cement Type I/II	1,298	31.9
Silica Fume (MasterLife SF 100)	398	9.8
Mason Sand	1,234	30.4
Filler	524	12.9
Fibers	265	6.5
Water	231	5.7
MasterGlenium 7920 (HRWR)	97	2.4
MasterSure Z 60 (Workability Extender)	17	0.4

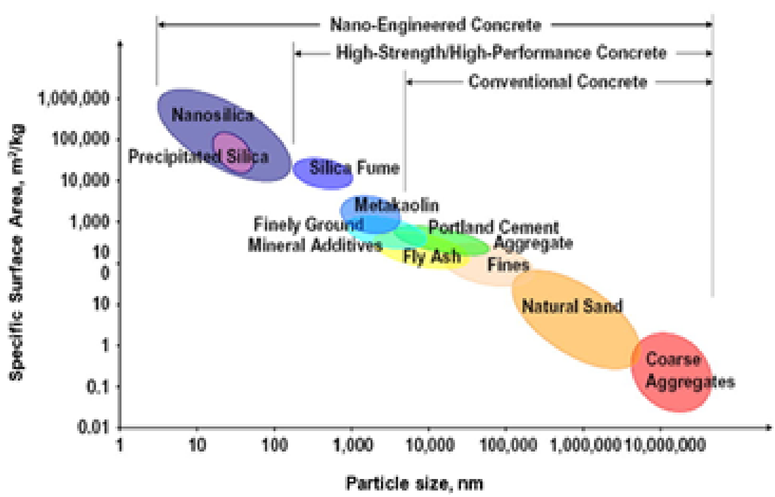

Figure 7. Particle size and specific area of concrete materials (Shi et al. 2015).

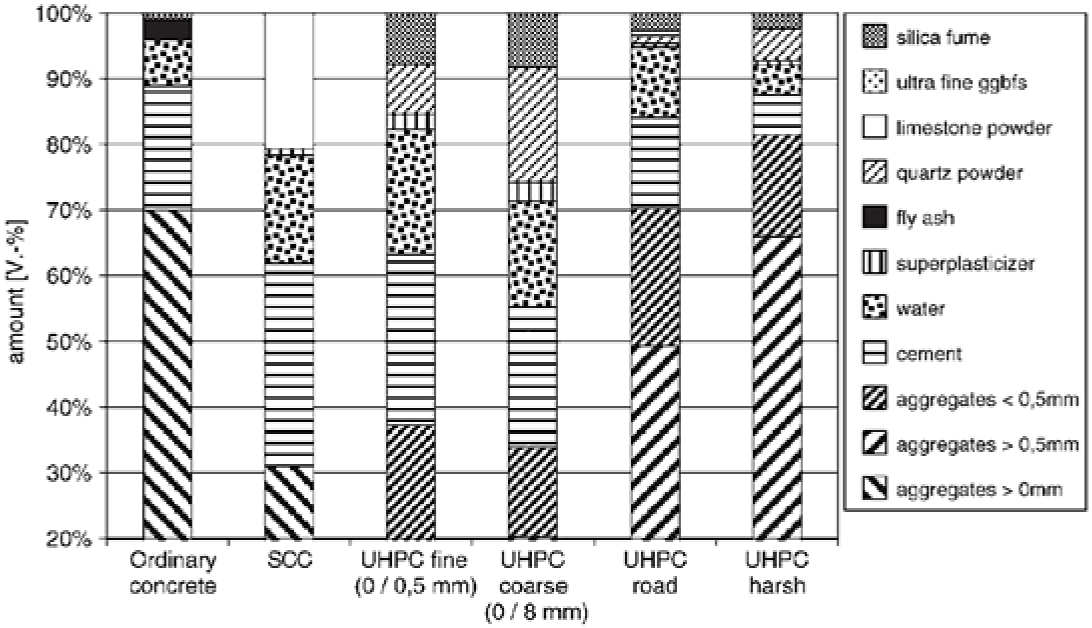

Figure 8. Comparison of some formulations for NSC, SCC, and various UHPCs (Fehling et al. 2014).

Portland cement of ASTM type I and/or II, with a low C_3A content is preferred, to curb the heat of hydration and ettringite formation. A recent FHWA report mentions the use of Class H oil well-cement for some UHPC formulations (Graybeal 2018). Some studies in Europe use CEM I 52.5 R (Shi et al. 2015) and others use sulfate-resistant cement CEM I 52.5 N (Huang et al. 2017a). Generally, a high cement content of 800–1,000 kg/m^3 is used to produce UHPC (Huang et al. 2017b). However, as the water-to-cement ratio is very low, about 65–70% of the cement remains unhydrated, and thereby it is effectively a filler (Courtial et al. 2013a). Therefore, the replacement of cement with ground/crushed quartz, fly ash, GGBFS (ground granulated blast-furnace slag), or limestone may have merits and have been investigated in several studies (Wille and Boisvert-Cotulio 2015; Courtial et al. 2013a; Huang et al. 2017b; Yu et al. 2014; Shi et al. 2015; Arora et al. 2018; de Larrard 1999; Huang et al. 2017a).

Although many of the above-mentioned cement replacements are used interchangeably, silica fume is an indispensable ingredient in UHPC, as it can act as a vital filler to improve the packing density of the concrete. It has a high content of amorphous silica, which can form additional C-S-H upon reacting with portlandite and thereby densifying the microstructure of concrete and refining the interfacial transition zone between the aggregates and cementitious matrix. The silica fume is the largest contributor to the thixotropy of UHPC due to its very fine particle size. The typical silica fume content in UHPC is 20–30% by weight of the cement. It is essential to optimize the content of silica fume, as very low content of silica fume may not enable the high early strength gain and too high silica fume content may result in a mix that is too viscous (Wang et al. 2019), leading to air entrapment. The carbon content of silica fume is important, as the carbon can adsorb the chemical admixtures and impact the performance of concrete.

GGBFS has been investigated in several studies (Wille and Boisvert-Cotulio 2015; Courtial et al. 2013b; Yu et al. 2014; Shi et al. 2015) as a viable cementitious replacement in UHPC. GGBFS is predominantly a filler material in UHPC, as silica fume or nano-silica are responsible for consumption of portlandite to form additional C-S-H. However, upon comparison with fly ash and limestone at the same levels of replacement (Yu et al. 2014), GGBFS performed better with higher compressive strength and lower portlandite content at 91 days. On the other hand, another study (Shi et al. 2015) stated that any addition of slag to cement-silica fume-slag systems increases the porosity corresponding to the percentage addition of slag, especially above 25%. Another study comparing GGBFS, limestone, and fly ash (Yu et al. 2014) said that incorporation of GGBFS reduced the superplasticizer (SP) demand in the mixtures.

Limestone powder (Arora et al. 2018; de Larrard 1999; Huang et al. 2017b) was used in many works as a viable cement replacement, mainly due to its low cost. It was seen that substitution of cement by limestone up to 50% by weight of cement had no negative impact on the compressive strength at 14 days; i.e., the target strength of 150 MPa was still achieved, though the initial packing density was reduced by the substitution (Huang et al. 2017a).

Fly ash is less popular for UHPC applications; however, it was still explored in a few studies (Yu et al. 2014; Arora et al. 2018). It was reported that fly ash contributes exceedingly well to reducing the SP demand in the cement-silica fume-SCM mixture. Shi (2015) reported that utilization of fly ash in combination with GGBFS enhanced the compressive strength in a ternary blend with silica fume.

1.3.5.2 Fine and Coarse Aggregate

Usually, the largest size of aggregates used in UHPC is 0.6 mm. Fine quartz sand of size 150–600 µm is a popular choice. The reasoning behind using a very small aggregate size is to reduce the size of defects in concrete. Fine quartz sand is an expensive aggregate, and many current research efforts investigate reduction of the cost of UHPC by substitution of the fine quartz by river sand and coarser and larger aggregate, by means of particle packing.

A recent study evaluated the properties of UHPC when fine quartz was substituted by locally available aggregates from different parts of the United States (Wille and Boisvert-Cotulio 2015). Four types of aggregates were selected including quartz, basalt, limestone, and volcanic rock (maximum size limited to less than 12.5 mm). In terms of mechanical performance, the best aggregate seemed to be quartz followed by basalt, volcanic rock, and limestone. However, through appropriate particle packing, they were able to achieve requisite UHPC strength (except for limestone in combination with steel fibers).

Another recent study assessed the utilization of coarse basalt aggregate in UHPC (Li et al. 2018) and determined that while utilization of basalt aggregates produced low compressive strength UHPC at the 28th day (at 144 MPa), the combination of basalt aggregate with steel microfibers was able to achieve the 150 MPa target strength.

1.3.5.3 Fibers

Steel, carbon, polypropylene, and glass fibers are some fiber reinforcements that are used in UHPC matrices. Of these, steel and carbon fibers are the most popular since polypropylene and glass fibers do not enhance the strength of UHPC (Shi et al. 2015).

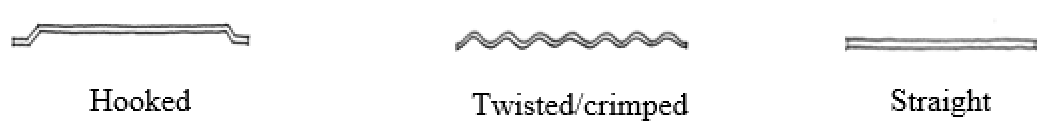

Figure 9. Profiles of steel fibers commonly used in UHPFRC (Katzer 2006).

The introduction of steel fibers can increase toughness of UHPC and the tensile strength of UHPC was seen to increase linearly proportionally to the dosage of the fiber (between 1–5% by volume). Beyond 5% is not economically viable. Some researchers (Kim et al. 2011) determined that the incorporation of a combination of macro- and microfibers improved the flexural toughness of ultra-high-performance fiber-reinforced concrete (UHPFRC). They also determined that in terms of flexural strength, hooked fibers performed better than twisted and straight fibers (in the same dimension).

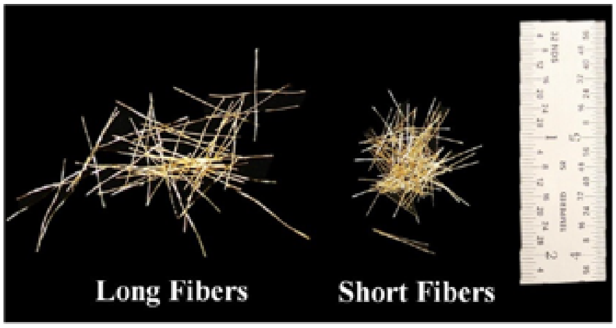

Twisted macro fibers (l = 20mm, Φ=0.3mm) and micro fibers (l = 13mm, Φ=0.3mm)

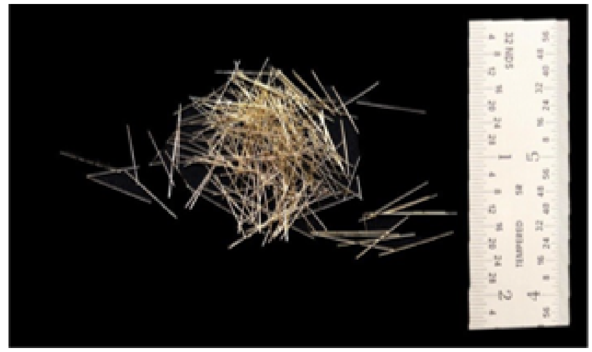

Smooth micro fibers (l = 13mm, Φ=0.3 mm)

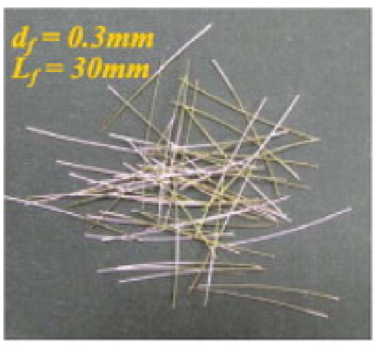

Smooth macro fibers (l = 30 mm, Φ=0.3mm)

Hooked macro fibers (l = 30 mm, Φ = 0.55 mm)

Figure 10. Some common types of steel fibers (Graybeal 2018 and Lee et al. 2018).

1.3.5.4 Water/Binder Ratio and Superplasticizers

Water-to-binder ratio of the UHPC needs to be minimized to ensure high strength and durability. The best way to reduce the water-to-binder ratio is the judicious use of superplasticizers. The water-to-binder ratio range typically used for UHPC is between 0.14–0.2 by weight (Baghaee Moghaddam and Baaj 2018). However, there is an optimal value of water-binder ratio where the highest strength is achieved (Yu et al. 2014). For a given combination of cement and binders, the water demand may be primarily determined for the transition between powder packing to a suspension. For this determination, the Puntke test (Mehdipour and Khayat 2018) may be used. In the Puntke test, the void fraction of the powders is believed to be filled with water in order to produce saturation, and thereby transition from powder packing to a suspension.

Following the determination of a basic water demand, the superplasticizer can be gradually added for this predetermined water-binder ratio, to attain a required flow (also denoted as spread), which may be determined by the means of a mini-slump test (as seen in Figure 11 (Azmee and Shafiq 2018)). The mini-slump spread may be inversely related to the plastic viscosity of the paste. For a better workability, a higher spread may be desired; however, this may not be true for all UHPC formulations.

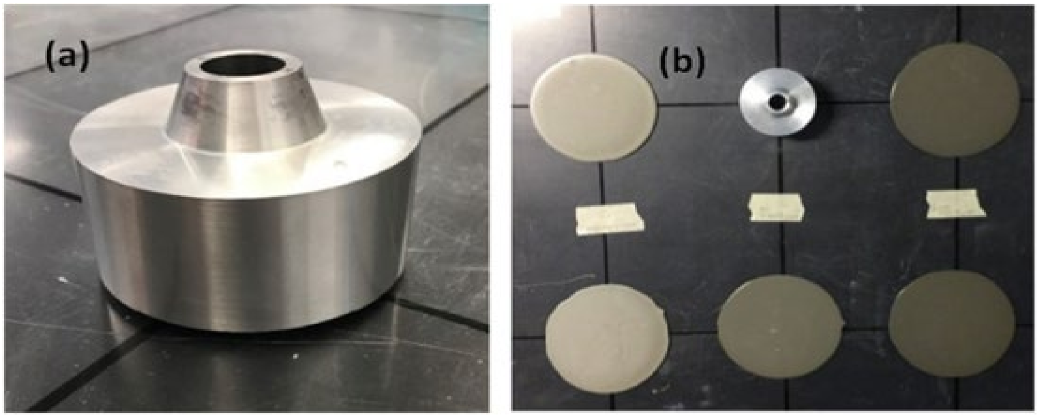

Figure 11. (a) Mini-slump cone and (b) mini-slump flow of pastes with differing binder combinations (Azmee and Shafiq 2018).

Mini-slump cone is a small-size, truncated cone similar in relative dimensions to Abraham's slump cone used for concrete slump test. It was developed by Kantro (1980) as a visual examination technique for determination of rheology of cement paste. The apparatus consists of a truncated cone-shaped mold and a glass plate to measure the spread seen in Figure 12.

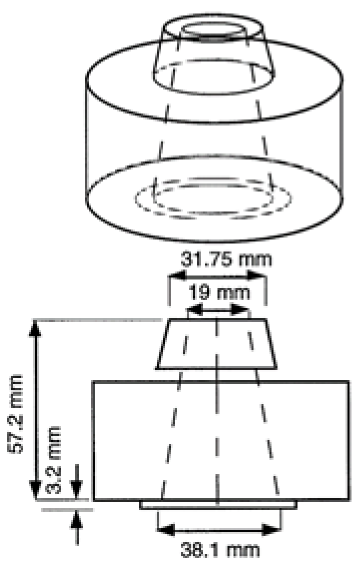

Figure 12. A typical mini slump cone (dimensions in mm) (Reproduced after [18]).

High-range, polycarboxylate-based water-reducing admixtures (PCE-based HRWRAs) are the most used superplasticizers. The stepwise addition of superplasticizer can improve its performance as compared to adding it all at once. A recent review of UHPC materials and mix design (Huang et al. 2017a) states that compatibility between the HRWRA and the binders is an important factor in the choice of an appropriate superplasticizer. It was determined that allyl ether-based polycarboxylate superplasticizers do not have specific interactions with silica fume, whereas methacrylate-based polycarboxylate superplasticizers interacted strongly. It is known that the silica fume content strongly affects the demand for superplasticizer, due to its fine size. Another study (Chen et al. 2019) determined that by virtue of the rounded particle shape of fly ash, the replacement of cement by fly ash reduced the demand for superplasticizers.

1.3.6 Fresh Properties

1.3.6.1 Rheology

For stiff UHPC formulations that do not need to be self-consolidating (such as the one seen in Figure 13), FHWA recommends using the conventional slump test (ASTM C1437).

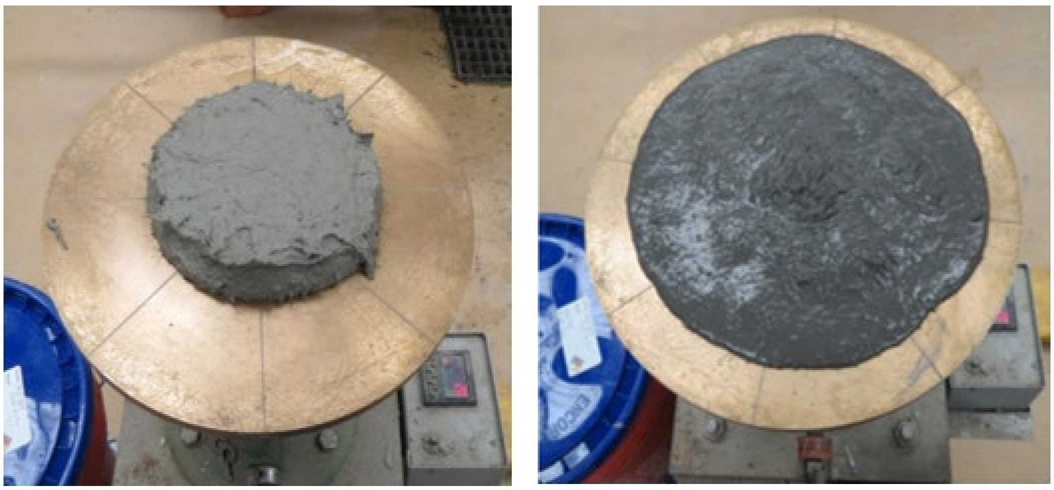

Figure 13. Flow table results for thixotropic and non-thixotropic UHPC mixtures.

In case of other non-thixotropic mix designs needed for connections, FHWA (FHWA-HRT-19-011) recommends the flow test described in ASTM C1856. The flow test (modified from ASTM C1437-15, Standard Test Method for Flow of Hydraulic Cement Mortar) is conducted once per UHPC mix and the flow must fall between 7 and 10 inches. The Swiss standard SIA 2052 (Brühwiler 2016a) requires that the overlaid fresh concrete maintain a required shape (i.e., doesn't flow) when it is sloped up to 7^{o} on a substrate (as per Figure 14). A platform can be modeled to simulate the slope of the bridge deck (θ in the figure is the slope of the deck). If the UHPC is found to be thixotropic (i.e., having a high yield strength), it could be deemed suitable for the overlay application.

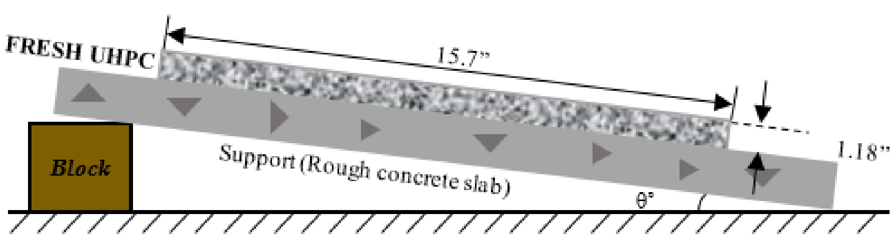

Figure 14. Slope test as per SIA 2052 (Brühwiler 2016a) (ASTM C1856 2017).

To measure the plastic viscosity (μ_p) and dynamic yield stress (τ_0) of the concrete, a recent study investigating cost-effective UHPC utilized a coaxial cylinder viscometer (seen in Figure 16). For a known shear rate and applied torque (which can be used to calculate the shear stress τ), the parameters μ_p and τ_0 may be calculated using the Bingham plastic model as noted in the Equation 1 (seen in Figure 15).

$$\tau = \tau_0 + \mu_p \dot{\gamma} \quad \text{Equation 1}$$

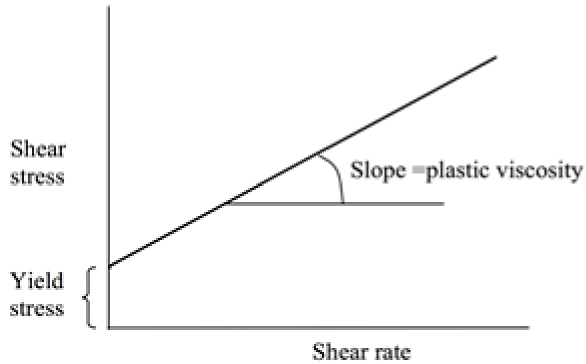

Figure 15. Bingham plastic model.

Figure 16. Contec® 5 coaxial viscometer (Feys and Khayat 2015).

1.3.6.2 Curing

Accelerated curing in the form of heat curing or steam curing may allow high early strength gain for some UHPC mixtures. However, it is not cost effective and practical for field-cast applications. Standard moist curing at room temperature is the most practical option for field-cast UHPC. Though standard curing resulted in weaker pozzolanic activity and smaller C-S-H chain lengths (Lee et al. 2018), after prolonged curing the compressive strength of UHPC could attain higher values (ASTM C1856 2017). For overlay applications, a minimum of 3 days curing is recommended by the NYSDOT. For connections, FHWA-HRT-19-011 recommends a minimum compressive strength of 97 MPa to subject the UHPC to construction and traffic loading. This strength is ordinarily attained between 2 and 4 days. However, if accelerators are added in the mixture design it may be possible to attain the requisite strength in 12 hours. In the laboratory, curing may be extended to 28 days.

1.3.7 Hardened properties

1.3.7.1 Compressive strength

Compressive strength of the UHPC is clearly the primary qualifying criterion for determination of its suitability (ASTM C1856 2017). The compressive strength of UHPC is determined as per ASTM C39, Standard Test Method for Compressive Strength of Cylindrical Concrete Specimens (Graybeal, 2018) using the modifications described in ASTM C1856 (i.e., a higher loading rate of 1 MPa/s should be used). ASTM C109 has also been used for evaluating the compressive strength of UHPC, although the strengths reported are 7% higher than that of the 3” by 6” cylindrical specimens (Pyo et al. 2017b). The NYSDOT requires that the cylindrical compression test be conducted at 1, 4, 7, 14 and 28 days of age for field-cast UHPC.
A study from Wille (Wille et al. 2011) summarized a few conversion factors for compressive strength of UHPC specimens of different geometry with respect to the strength of a 100 mm cube specimen of UHPC, as seen in Table 4.

Table 4. Influence of specimen size on compressive strength of UHPC (Wille et al. 2011).

Specimen Type	Conversion Factor
Cylinder (100 mm×200 mm)	0.98
Cylinder (150 mm×300 mm)	0.94
Cylinder (76 mm×150 mm)	0.98
Cube (50 mm)	1.04
Cube (150 mm)	1.05

1.3.7.2 Tensile strength

UHPC exhibits higher tensile strength than normal strength concrete because of the incorporation of steel microfibers and the denser packing of particles (Abbas et al. 2016). A recent FHWA report summarized the direct and indirect measures of tensile strength of UHPC and is briefly discussed in this section.

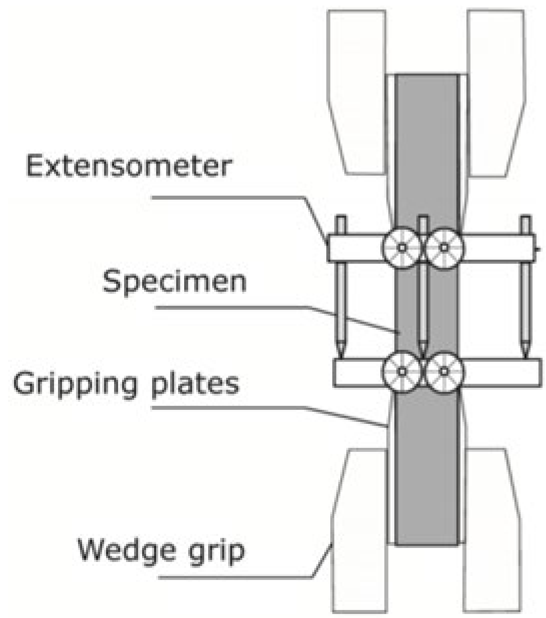

Figure 17. Schematic of direct tension test (Graybeal, 2018).

The direct tension test can be used to determine the uniaxial tensile response of a UHPC prismatic member (as seen in the stress-strain diagram below). The 3 phases of the response can be described as:

Phase 1 – Elastic response until the first cracking strength is attained

Phase 2 – The multi-cracking phase where multiple cracks may result until the strain becomes localized and a single discrete crack forms

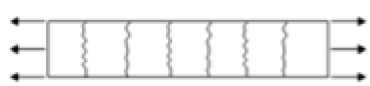

Phase 3 – The individual crack widens in this stage and the fibers bridging the crack de-bond from the matrix and pull-out

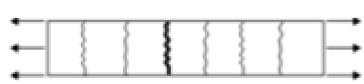

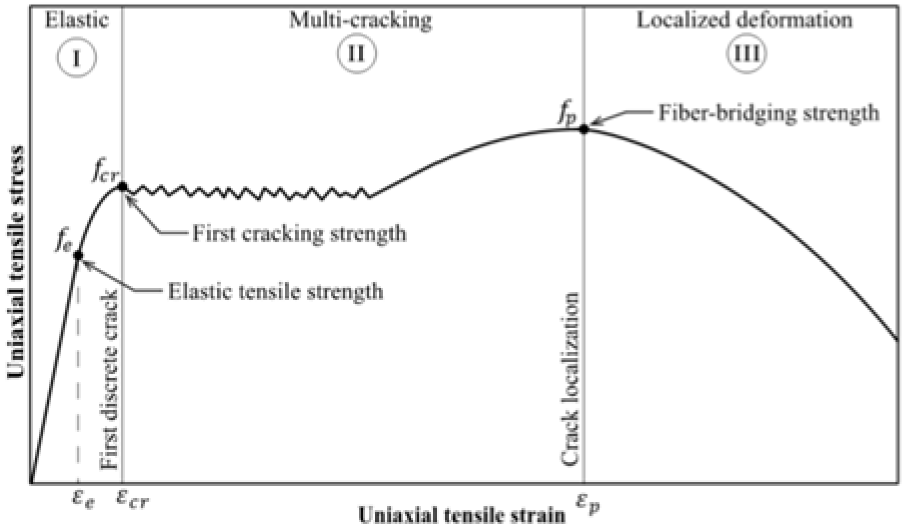

Figure 18. Uniaxial tensile response for UHPC (Graybeal 2018).

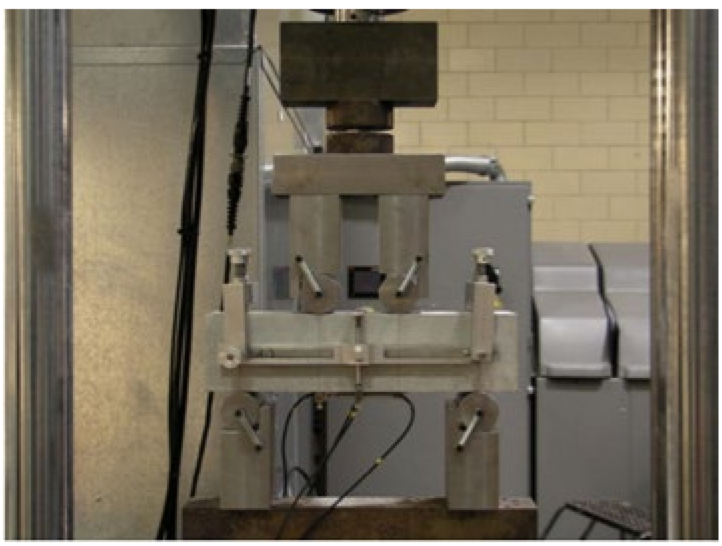

Figure 19. 4-point bending prism test of UHPC.

FHWA (Graybeal and Baby 2019) also recommends a 4-point bending test in flexure to assess the uniaxial tension behavior, using inverse stress-strain relationships as per Equation 2. The strain is related to the stress using a compliance modulus S.

$$\varepsilon = S\,\sigma \qquad \text{Equation 2}$$

The indirect test for measurement of tensile strength of UHPC prismatic specimens, with respect to flexure, is conducted as per the requirements of ASTM C1609/C1609M (Flexural Performance of Fiber-Reinforced Concrete (Using Beam with Third-Point Loading), with modifications of the ASTM C1856 (Pyo et al. 2017a). The size of the test specimen is dictated by the longest dimension of the fiber, as denoted in Table 5.

Table 5. Dimensions of beams for measuring flexural strength.

Maximum Fiber Length (l_f)	Nominal Prism Cross Section
< 15 mm [0.60 in.]	75 mm by 75 mm [3 in. by 3 in.]
15 mm to 20 mm [0.60 in. to 0.80 in.]	100 mm by 100 mm [4 in. by 4 in.]
20 mm to 25 mm [0.80 to 1.00 in.]	150 mm by 150 mm [6 in. by 6 in]
> 25 mm [1.00 in.]	200 mm by 200 mm [8 in. by 8 in.]

1.3.8 Experimental Testing

The Federal Highway Administration has been focusing on the use of UHPC in the bridge connection of precast bridge components (Elements, 2014). The research conducted by the U.S. Department of Transportation tests how the superior performance of the UHPC serves as a new generation connection. With the increase of technology in bridge deck components, we must have a durable connection that can withstand the stress and fatigue that comes from structural and environmental factors. The specimens tested in that research are precast concrete panels that are joined using UHPC closure pour. In the research, the UHPC is tested as a transverse and a longitudinal connection. In addition, the dimensions and configuration of the connection were studied as well. The results from cyclic loading of the test specimens showed that the UHPC bond was sufficient. No debonding was observed through all the loading. The tensile cracks of the precast panels were replaced with smaller tight cracks. This validated the expectation and use of the UHPC. It is essential moving forward that to ensure the performance of the connection, the direct bonding of the concrete is also thoroughly investigated.

The joint between different concrete interfaces in achieving the optimal bond strength has been studied more and more throughout its history. The surface preparation and roughness are two direct factors in achieving adequate bond strength. Slant shear tests were conducted at the University of Virginia to study the bond compatibility of UHPC and normal concrete (Safritt, 2015). Slant shear tests have been a very common easy and fast method for testing the surface-to-surface bond between different materials. The bond is tested via shear forces applied to the interface of the materials. In their research, different surface preparations are tested (normal, sandblasted and etched with hydrochloric acid). The effects of different admixtures and aggregate moisture conditions were tested as well. The bond strength and failure types were recorded from each test. In conclusion, the test data showed that the sandblasted surface produced the strongest bond between the two concretes. Sandblasting is ideal for creating the interface friction because it is an easier method that produces the strongest bond. However, there was no index recorded for tracking the roughness of each specimen in these tests. A large majority of the failures occurred at the bond interface and the rest occurred in the UHPC. With no clear trend in the failure type of the concrete, we can assume the full bonding of the concrete was not fully captured through the slant shear test.

Santos et al. (2007) studied the effects of the surface roughness on the bond strength by quantifying the roughness of each interface surface. Slant shear tests and pull-out tests were performed to study the bond strength of the concrete in compression and tension. In these tests, a smooth, a rough (sandblasted), and a slightly rough surface (wire-brushed) were tested. The data showed that roughness can be quantified accurately and not just described in a qualitative process. Like our current research, this allowed for a more detailed relationship between the roughness and bond strength. Laser profiling was recommended as the best way of acquiring the profile of the interface. As expected, the data showed us that the sandblasting produced the strongest bond between the concrete.

Julio et al. (2004) continued the research on concrete-to-concrete bonding by investigating the surface of the substrate. The slant shear test and pull-out test were performed to obtain the bond strength in compression, tension, and shear. In addition to the commonly used wire brushed and sandblasted surface, chipped surface from jackhammering was tested as well. There are some concerns with this method, given the belief that jackhammering causes damage to the substrate due to microcracking in the concrete. Sandblasting was shown to produce the strongest bond, with the bond strength being 35% higher than that of wire brushing. In this study, the effects of pre-wetting the substrate concrete are also investigated. This affects the moisture condition and absorption of the concrete. Pre-wetting the surface helps achieve a saturated surface dry condition, which is ideal for bonding. However, the data received showed that pre-wetting had no real significance on the bond strength of the concrete. This gives us great insight for our present work and bonding tests.

Tayeh et al. (2013) explored the influence of mechanical properties and permeability of the interface on bonding. The bond between the normal concrete and the UHPC were tested using the slant shear test and a splitting tensile test, which is an indirect method of testing the bond strength in tension. The concrete specimens were tested at various ages during a 28-day period. This allows the bond strength growth to be tracked with age. Several different surfaces were prepped and tested (wire-brushing, sandblasting, grooved surface, etc.). The data from both the shear and tensile test showed that all of the prepped surfaces produced strong bonding. The fractures occurred in the normal concrete before occurring in the interfaces of the two concretes. The sandblasted surface created the strongest bond, as expected, due to the interlocking and adhesion from the exposed aggregates on the bond interface. The silica fume was shown to have a great effect on the bond strength by improving the transition zone in the concrete through pozzolanic reactivity. The data from the test showed how slowly the bond strength increased with the age of the concrete (Age of 7 days to 28 days). The results established that the bond behavior of the concrete is more influenced by the surface preparation than by any other factors.

The previous methods of investigating the bond strength of concrete present a long history as well as room for improvement. The previous method of bond testing is one that is low-cost as well as being easy to produce. The slant shear test has been the primary test for bond testing. Pull-out testing has been used as well to study the bond behavior of the concrete in tension. Although this test provides a uniform distribution of stress along the bond interface, confusion and inconsistency can occur from the results obtained from the test (Zanotti & Banthia, 2016; Li & Rangaraju, 2016). The combination of shear and compression stresses during loading can potentially cause misrepresentation in the failure modes and the behavior of the materials bonded. Exploring different methods such as flexural testing can help simplify and ensure the analysis of the bond behavior.

Flexural testing has a long history of studying the different mechanical properties of various materials. Flexural testing has a history of exploring the bending behavior and modulus of elasticity of any material. This test also allows us to capture the bending fatigue of the material and the stresses that are developed during loading. Flexural tests have commonly been used in exploring crack growth in concrete material. The history of the flexural test shows that the 4-point or 3-point bending test is an essential test needed for new composite materials. In this report, a brief overview of the test capabilities is provided.

Zou et al. (2020) performed the 4-point bending test to analyze the damage and the fatigue properties of stone matrix asphalt. Asphalt is a material that has a complex stress-strain state. The 4-point bending test was used to compare and study the behavior of the asphalt under different temperatures, test conditions, variations of frequency, and strain levels.

Yin et al. (2019) explored the use of the 4-point bending test in studying the fracture properties of concrete. All the different values such as the load, cracks, and deflections were recorded during the loading. Various initial crack depths of different widths were investigated. The results solidified the use of the 4-point bending test in analyzing fracture properties.

Hofinger et al. (1998) explored the use of the 4-point bending test in tracking the fracture energy of the tested specimen. The test was modified to allow the energy rate at the bond interface to be measured. The specimen used in the testing had thin, brittle layers, which were bonded to a substrate material. In their test, a modification that was made to the 4-point bending test allowed for the evaluation of the interface fracture toughness. This included layers that were separated by vertical cracks.

Baby et al. (2013) used the 4-point bending test to explore the tensile behavior of UHPC under loading. This research used the bending test to help understand the tensile carrying capacity of high-performing concrete. Many researchers have attempted to produce a test for obtaining the tensile behavior of ultra-high-performance fiber-reinforced concrete. The stress-strain relationship of the concrete was created with the use of inverse analysis, as displayed in their research.

The history of flexural bending tests shows that this testing is important in understanding the stress-strain relationship of different materials, as well as the cracking and deflection. With this current work, we will examine the potential of this test in studying bond behavior. With the simplicity and the consistency in the results that are obtained, this test will allow us to assess the bond behavior between the concrete within the joint connection.

1.3.9 High-Performance Concrete

The more superior concrete has been explored in bridge applications due to its greater performance and properties. As the concrete becomes more advanced, we witness better workability, strength, durability, and ductility. These traits are important to the behavior and service life of applications such as the joint connection of precast components. High-performance concrete is a more advanced material than the conventional normal-weight concrete. The main difference between the two concretes is the use of mineral and chemical admixtures in the HPC. The addition of admixtures such as silica fumes and superplasticizer allow the concrete to exhibit better flowability and compressive strength. These traits are also obtained from the lack of coarse aggregates in the HPC. The addition of the chemical admixtures allows for lower consumption of water in the concrete mix. Therefore, HPC has a lower water-to-cement ratio than the normal-weight concrete. The water-to-cement ratio for higher-strength concrete is usually designed to be less than 0.4. This contributes to the compressive strength of the HPC as well as the porosity within the hydrated cement paste. The enhanced properties make HPC a desirable material. While there are advantages of using HPC, this study will focus on the use of UHPC, where FHWA-HRT-19-011 recommends a minimum compressive strength of 97 MPa to subject the UHPC to construction and traffic loading for bridge applications.

Chapter 2

Material Characterization

The primary objective of this chapter is to provide details on the material characterization of the UHPC. This chapter provides details on the locally available mix constituents, the mix design, measurement of compressive strength, measurement and calculation of direct tensile strength, and measurement of flexural strength. This chapter will serve as a guide to the mix design development of UHPC using locally available mixture constituents.

2.1 MATERIALS AND METHODS

The UHPC mixture constituents in this project consist of the binder components, sand, chemical admixtures, and fibers. The subsequent sections explain these constituents in more detail. Tables 6 through 8 show various binder components with cement.

2.1.1 Binder Components

The principal binder components used in this study are ASTM Type II Cement (with C_3A content <5%), an undensified fine silica fume (from Norchem®) (ASTM C1240), and a ground limestone powder (known as aggregate mineral filler) used as a supplemental material.

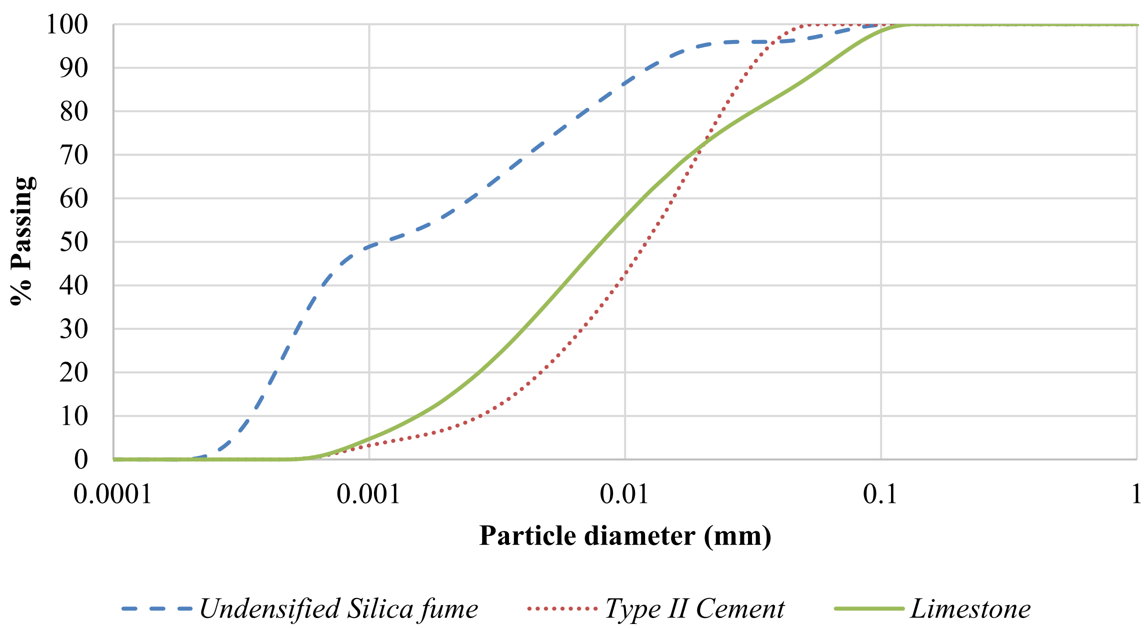

Figure 20. Particle size distribution of the silica fume, cement and supplemental material used.

Table 6. Physical properties of the binder components.

Parameter	Cement	Undensified Silica Fume
Specific Surface Area (m^2/kg)	426	15,000

Table 7. Chemical parameters of the cement and silica fume used in this study.

Parameter	Cement (%)	Undensified Silica Fume (%)
CaO	62.83	0.95
SiO_2	19.83	95.68
Al_2O_3	4.29	0.22
Fe_2O_3	4.18	0.02
MgO	3.54	0.21
SO_3	2.73	0.18
Alkalis as Na_2O eq.	0.90	0.28
Loss on Ignition	0.65	2.52

Table 8. Bogue's composition of the ASTM Type II Cement.

Compounds	%
C_3S	62.5
C_2S	9.8
C_3A	4.3
C_4AF	12.7

2.1.2 Sand

In this project, the sand was locally sourced from Pennsylvania, and two locally available manufactured mason sands, a siliceous mason sand, and a quartzite mason sand were used in this study. Their grain size distribution is plotted in Figure 21.

It is noted that UHPC sands do not need to comply with the existing gradations specified for concrete sand (ASTM C33) or for masonry sand (ASTM C144). The sand that was chosen for development of non-proprietary UHPC was a locally available fine sand with a higher percentage of particles less than 600 µm (to ensure that the mix was as finely graded as possible).

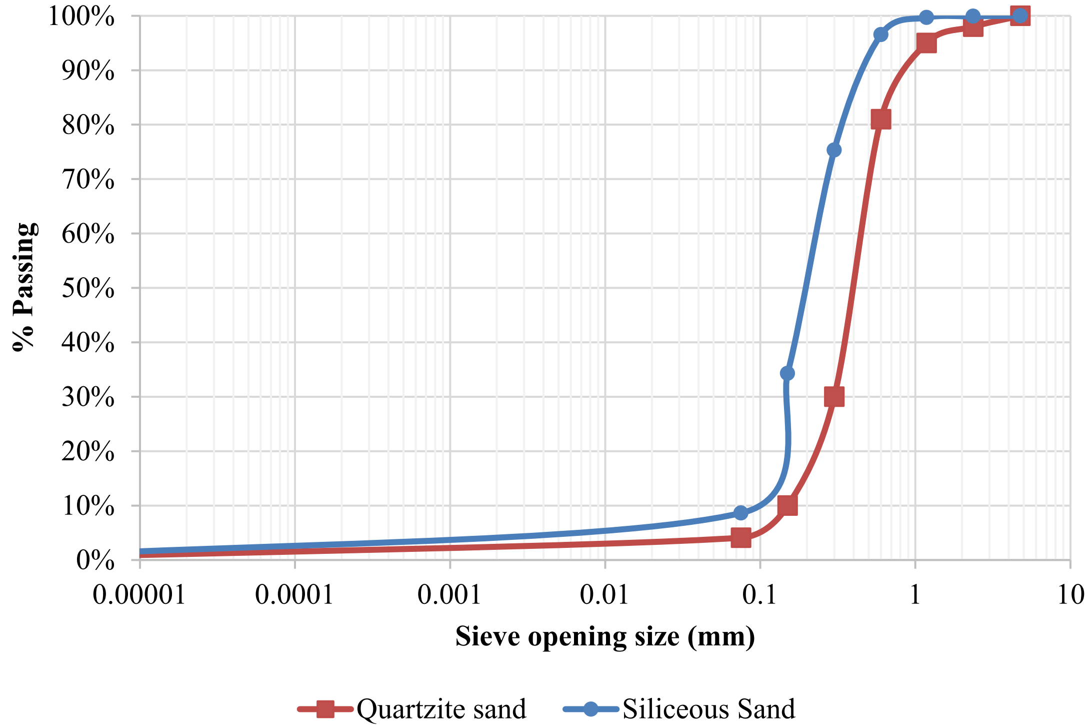

Figure 21. Grain size distributions of the sand used.

2.1.3 Chemical Admixtures

UHPC typically needs high dosages of superplasticizer to make the concrete self-consolidating. In addition, workability-retaining admixtures may be used to prevent loss of workability in the UHPC. In this study, the primary chemical admixtures used in the formulation of UHPC mixtures are a polycarboxylate-based superplasticizer (Masterglenium 7920®) (complying with ASTM C494/ C494 M for Type F) and a workability-retaining admixture (MasterSure Z60®) (complying with ASTM C 494/C 494M requirements for Type S). The physical characteristics of these admixtures are summarized in Table 9.

Table 9. Physical properties of the chemical admixtures.

Physical Properties	Superplasticizer	Workability Extender
Density (g/cm^3)	1.07	1.04
% Solids	33	20

2.1.4 Fiber

The fibers used in this study were steel microfibers from Baekart (OL13/0.2), which followed ASTM A820. The physical properties of the fibers are summarized in Table 10.

Table 10. Physical and mechanical properties of fiber used in this study.

Property	Value
Length	13 mm (0.5”)
Diameter	0.2 mm (0.008”)
Aspect Ratio	65
Density	7.87 g/cm^3
Nominal Tensile Strength	2750 MPa (400 ksi)
Modulus of Elasticity	200 GPa

2.1.5 Mix Design

2.1.5.1 Statistical modeling and selection of mixture

In the design of UHPC mixtures, due to the lack of well-established mix design guidelines, there is considerable trial and error involved. To eliminate the need for extensive experimentation and also to provide a guideline for producers to develop UHPC using locally available material, a statistical model was developed. The mix design adopted for UHPC used in this study was formulated based on the objective of attaining a target compressive strength for a given UHPC mixture design based on statistical modeling (from known data).

An extensive literature review was conducted to compile a table of published mixture proportions, so that we may gain some insightful relationships between the performance of UHPCs (28th-day compressive strength) and their mixture ingredients. A database of 169 UHPC mixtures was collected and curated, and its properties are summarized in Table 11.

Table 11. Summary of proportions from the 169 non-proprietary UHPC mixtures.

Ingredient	Range (kg/m^3)
Portland cement (C)	300–1,251
Silica fume (SF)	0–291
Supplemental materials (SM)	0–1,058
Water (W)	135–252
Fine aggregate	400–1,500
Admixture (SP)	5–46
Fiber	0–157

Once the database was collected, some of the collected data were eliminated, following the criteria below:

a. UHPCs with coarse aggregates (> 4.75 mm) were eliminated.
b. UHPC mixtures with too low or too high cement content (< 400 kg/m^3 or > 1,000 kg/m^3) were eliminated.

After elimination of the 36 data points, the remaining 133 data points were used for model development and, based on accepted statistical theory, the number of data points is sufficient to obtain a precise estimate of the strength of the relationship between the predictors and the response. For these points, the collected compressive strength data for UHPC was harmonized to account for the differences in the specimen types and sizes used for the measurement of the strength, using the factors in Table 12.

Table 12. Conversion factors for the compressive strength of UHPC to that measured using a 3" x 6" cylinder (Abbas et al., 2016).

Specimen Type	Conversion Factor
Cylinder 150×75 mm	1
Cube 50 mm per ASTM C109	0.94
Cube 40 mm per EN 196-1	0.9
Cube 100 mm	0.94

It is well-established that to predict compressive strength, water-to-cement ratio plays a major role. However, in UHPC, there are additional factors that influence the strength of mixtures, including the role of silica fume, the later age enhancement of strength using supplementary cementitious material, the role of particle packing and, finally, the binder volume (which in turn dictates the aggregate volume). To ensure consistency across the mixture variables considered in this study, the following independent variables were chosen: W/C, SF/C, SM/C, V_p. In addition to these variables, a factor that would indirectly impact compressive strength was chosen as categorical predictors (i.e., presence of fiber). Analysis of variance was used to determine the significance of the predictors in the model and, as seen in Table 13, all the predictors used were highly significant.

Table 13. Analysis of variance table of the predictors chosen in the model.

	Pr(>F)	Significance
W/C	0.000364	***
SF/C	5.60E-16	***
V_p	2.20E-06	***
Fiber Content	2.20E-16	***
SM/C	4.39E-05	***

*** *denotes a p-value of less than 0.001*

The model was fitted using R statistical software and a multiple linear model regression model (seen in Equation 3) fitting all the predictors was determined. The model is summarized in the form of,

$$Y = \beta_0 + \sum_{i=1}^{n} \beta_i X_i + \varepsilon \qquad \text{Equation 3}$$

Here Y denotes the fitted mean value of compressive strength ($f'c$) and X_i denotes the various independent variables used in the model. The regression coefficients for the intercept and slope of the regression model are given in Table 14.

Table 14. Estimated regression coefficients of the linear model.

Regression Coefficients	Estimate Value
Intercept	136.5
W_C	284.6
SF_C	119.6
SM_C	22
Vp	94.7

Further, a function that relates the cost of the UHPC mix design (in \$/m^3) was developed. This function considered the averaged unit cost of commonly used UHPC mixture constituents, and the related cost of the UHPC mixture to the same variables that were used to model the compressive strength.

Cost of UHPC mixture (\$/m^3) with 2% volume of fiber =

$$V_p\left(\frac{376 + 1909\left(\frac{SF}{C}\right) + 379.8\left(\frac{SM}{C}\right)}{1 + 1.43\left(\frac{SF}{C}\right) + 1.17\left(\frac{SM}{C}\right) + 3.15\left(\frac{W}{C}\right)} - 325.55\right) + 998 \quad \text{Equation 4}$$

This function was used in combination with the regression model to generate synthetic data for 10,000 mixtures. Here, 10,000 values of each of the input variables were randomly generated, using a uniform distribution, to fit in the cost and compressive strength functions and generate mixtures. The range of these independent variables were chosen based on recommended UHPC design proportions of the FHWA (Wille, 2013).

Table 15. Range of Independent variables used in mix.

Variable	Range
W/C	0.2–0.4
SF/C	0.05–0.35
SM/C	0–1
Volume of Cement	0.12–0.32

At the end of this approach, 10,000 mix designs were generated, and their associated unit cost was calculated. This approach enables us to choose possible candidate mixtures for a given compressive strength, at minimum cost.

2.1.5.2 Particle packing models to select the mix design

The maximum packing density could be attained by producing a gradation as “close to ideal grading curve” [31] as possible or with a packing density as close to the maximum virtual packing density. The particle packing model chosen in this study was the modified Andreasen and Andersen (A&A) model.

This approach of particle packing assumes that there are all possible sizes present in a system between the maximum and minimum size. The particle size distribution may be determined by,

$$P(D_i) = \frac{D_i^q - D_{min}^q}{D_{max}^q - D_{min}^q} \qquad \text{Equation 5}$$

$P(D_i)$ – fraction of total solids smaller than particle size D_i (Cumulative percentage finer than D_i)
D_i – particle size (µm)
D_{max} and D_{min} – maximum and minimum particle size (µm)
q – distribution modulus
Distribution modulus mathematically determines the curvature of the cumulative particle size distribution of the mixture from Equation 5. It is indicative of the proportion between fine and coarse particles in the concrete (considering the high quantity of fine particles, a value of q is chosen appropriately: q = 0.17-0.23).

Equation 6 provides a formula for a smooth cumulative particle size distribution (PSD) that is used as a target PSD for mix design of the concrete. This model tries to optimize the composition of the granular mixture by adjusting the individual components until a difference between the obtained mixture and ideal packed mixture is lowest, as computed in Equation 7.

$$RSS = \sum_{i=1}^{n} \left(P_{mix}\left(D_i^{i+1}\right) - P_{tar}\left(D_i^{i+1}\right)\right)^2 \qquad \text{Equation 6}$$

where,

$P_{mix}(D_i)$ = Cumulative % finer than particle size D_i for the selected mixture

$P_{tar}(D_i)$ = Cumulative % finer than particle size D_i for the idealized mixture from modified A&A model

$$Closeness\ of\ fit = \frac{RSS}{P_{tar}\left(D_i^{i+1}\right)^2}$$

Equation 7

This method is very popular due to its ease of use and requirement of minimal number of inputs in the optimization. The "q" factor is decided beforehand, and thereby it is only necessary to determine the particle size distribution for each of the components in the mixture. The value of distribution modulus (q) assumed in this study is 0.20. This value is midway in the range of the commonly used distribution moduli. With too high a value of distribution modulus, the UHPC mixture becomes too coarse and too low, and the UHPC is very difficult to work with (Kumar et al., 2020).

2.1.5.3 Final UHPC Mix design adopted

To ascertain the comparability of the properties of the non-proprietary UHPC to the commercially available premixed UHPC mixtures, a commercially available proprietary UHPC from a local provider was used.

Table 16. Adopted UHPC mix design.

Mix Constituent	Volume or Type
Water (kg/m^3)	193
Cement type	ASTM Type II
Cement content (kg/m^3)	770
Silica fume content (kg/m^3)	236
SM content (kg/m^3)	311
HRWRA (kg/m^3)	10.5
Fine aggregate (type)	Fine siliceous sand (PA)
Fine aggregate content (kg/m^3)	732
Fiber content (kg/m^3)	157

2.1.6 Mixing Procedure

Mixing of UHPC is considerably different from conventional concrete. The mixing duration and sequence of mixing are highly dependent on the type of mixer and the type of material used in proportioning of the concrete. A review of UHPC mixing protocols seen in various published studies was conducted to determine the most appropriate mixing protocol for the non-proprietary UHPC mixtures.

Figure 22. High shear mixer used for mixing of UHPC.

Table 17. UHPC Mix sequence suggested in select published studies.

Source	Mixing Procedure Followed	Total Mixing Time (minutes)
AZDOT Report 2018 (Neithalath and Arora)	1. Quartz powder and sand were initially dry-mixed with silica fume in a Hobart mixer for 5-10 minutes. 2. The powders were then transferred to a high-shear mixer (handheld high-shear in bucket) and mixed for 10 more minutes with cement (until color appears uniform), then the water and superplasticizer mixture were added gradually in thirds of total volume (5 minutes each for each third of the volume). 3. The mixing was continued until a cohesive mixture was obtained. 4. Fibers were added and another 5-10 minutes of mixing was carried out.	30-45
Kay Wille and Boisvert-Cotulio, 2011	1. Aggregate, silica fume and quartz powder were dry mixed for 5 minutes at low-speed in a Hobart mixer. 2. Adding cement and SCM, the combination was mixed for 5 minutes at medium speed until homogenous. 3. One third of the mix water and superplasticizer was added to this mixture and mixed at medium for 5 minutes more. 4. Finally, the rest of the water was added and this mixture mixed at high speed until cohesive, then fibers were added and the mixture was mixed for 5-10 minutes more.	25
Weina Meng and Kamal Khayat, 2018 (Ph.D. thesis)	1. Aggregate and quartz powder were dry mixed at 60 rpm for 60 seconds. 2. To this mixture the dry cementitious materials were added and this was mixed at 60 rpm for 2 minutes. 3. 90% of the mixing water and superplasticizer was added and the mixture was further mixed at 120 rpm for 3-5 minutes. 4. The remaining mix water and SP were added, and 5 more minutes of mixing was carried out 5. The micro steel fibers were gradually added within 1 minute at 60 rpm and the mixture was mixed at 120 rpm for 2 minutes.	15-20

Two separate UHPC mixes were used for all the experimental lab testing that was conducted. The primary mixture involved was CT25 UHPC and is referred to as the "proprietary" mixture throughout the testing program. CT25 is the standard high-strength UHPC mixture from Cor-Tuf and is used in many applications, including bridge connections, overlays, and other structural components. The second mixture used during testing was a self-developed UHPC mixture. This mix used components that were all non-proprietary and locally sourced in the Mid-Atlantic region of the United States. These constituents include cement, silica fume, mason sand, mineral filler, steel fibers, water, a high-range water reducer (HRWR), and a workability extender.

At least 48 hours prior to the mixing of UHPC, the sand is dried in a 105 °C oven for 24 hours. Then, at least 24 hours prior to mixing, the oven-dried sand and cooled sand are prewetted with a predetermined moisture content. The mix water is prepared by keeping the pre-weighed amount of water in a refrigerator overnight (2-4 °C). The following mixing procedure is then adopted:

1. The moist sand, supplemental materials, cement, silica fume, and steel fibers are added to the mixer and mixed for 2 minutes or until visibly homogenous.

2. The chilled mix water (2-4°C) and about 50% of the superplasticizer are added together and the UHPC is mixed for 3 more minutes. Then, after adding the remaining superplasticizer and workability extender, the UHPC is further mixed until the mixture "turns over," called turnover time, typically 5-7 minutes more.

Initially powdery → Small balls form → Mixture resembles dough → Flowable

3. After the UHPC becomes flowable, it is mixed for 1 more minute to ensure homogeneity.

2.1.7 Fresh Property Assessment

2.1.7.1 Workability

The flow test is the standardized fresh property evaluation recommended by FHWA and is required by many DOTs to provide a quality control measure for UHPC applications. This test helps ensure consistency among multiple mixes and suitability for casting of hardened property specimens. Most UHPC flow tests are conducted on a setup consisting of a brass mini cone and a 10-inch plate flow table. The spread is typically measured three or more times to produce an average spread for each mix.

A flow table complying with ASTM C230/C230M-21 was used to evaluate the static flow of UHPC in accordance with ASTM C1856/C1856M-17 (ASTM C1856, 2017). The UHPC was filled in the greased conical mold, under its own weight. The concrete was allowed to rest for a minute, before the mold was lifted, and the spread diameter was evaluated. The average of 4 measurements made with the vernier caliper was reported as the final spread flow of the UHPC.

Figure ***23. Static spread diameter of UHPC.***

Table 18. Average spread for the proprietary and non-proprietary UHPC mixes tested.

Mix	Spread
4-2-21	8.25”
5-3-21	8.50”
6-3-21	8.50”
6-8-21	7.00”

Figure 24. Standard filling procedure of brass flow table prior to measuring the UHPC spread.

2.1.7.2 Fresh air content and setting time

The fresh air content of the UHPC was evaluated using ASTM C231/231M and the setting time was measured in accordance with ASTM C191 (Vicat Apparatus). The setting time was not evaluated using penetration resistance, due to the presence of fibers in the UHPC mixtures due to the surface drying of UHPC (tendency to form a stiff surface layer).

Figure 25. Measuring UHPC spread during a flow test.

2.2 FLEXURAL BOND STRENGTH TESTS

Understanding the effectiveness of the bond between materials plays a vital role in maintaining structural integrity and durability of the connection. This is important for bridge joints, as load transfer across joints is expected. Therefore, proper testing to verify the bond between materials is needed to ensure the mechanical properties of the concrete mix and the design of the connection.

2.2.1 Four-Point Testing

Various 4-point tests were conducted to verify the use of flexural bending in testing the bond of the concrete. Previous methods in bond testing have their flaws and drawbacks, which makes the use of flexural bending tests attractive. The previous methods consist of performing shear slant and the pull-out test to study the bonding in compression and tension. Although these tests are simple and inexpensive, the complex combination of stresses caused during testing can misrepresent the fracture type and the total bond behavior of the concrete (Zanotti & Banthia, 2016; Li & Rangaraju, 2016). Due to the simplicity of the flexural bending test, the consistency in the results, and the display of the cracking behavior in the concrete, the results obtained from testing will be used to validate the use of the 4-point bending test for critical bond testing.

To validate the use of the flexural bending test in studying the bond behavior between the concrete, 4-point bending tests were done on beams made of the lesser HPC and precast concrete. In our testing, the effects of the moisture condition on the existing precast surface were tested. The surface roughness throughout the test was altered under different moisture conditions to see how the curves vary under different moisture conditions. The results from our tests contained the flexural strengths of the samples, the roughness quantity, and the fracture type of the beam. Three different surface roughnesses were tested, ranging from low to high roughness. The roughness was obtained using different retarder durations; the duration of the retarder determines how much cement paste is left on the surfaces. The longer the duration, the smoother the bond surface becomes. The test duration ranged from 20 to 30 hours. All of our roughness quantities were tested under two different moisture states, surface saturated dry and air dry (AD). At SSD, the internal pores are filled with moisture and the surface is absent of any water. At the AD condition, the surface is also absent of any water and the pores are partially filled with water. At an AD state, the concrete will absorb moisture from the fresher concrete to hydrate itself, unlike that of the SSD state.

2.2.2 Results

These results will help identify the effect the moisture condition has on the bond behavior. The data show an exponential decrease in flexural strength as the roughness decreases. The decrease in flexural strength jumps from 3% to 18%. At an AD condition, we experience a more linear decrease in flexural strength as the roughness decreases. These data show that the absorption and suction of moisture from the fresh concrete can contribute to maintaining the bond of the concrete. It is still unclear from our results the long-term effects that the AD condition will have on the bond and the stress produced from it. The data allow us to see that the absorption created from the AD states can contribute to the bonding at its early stage. Modifications to the design mix and the type of concrete used can mitigate the long-term effect of having the moisture condition at AD at the bond. This lessens the need to create an SSD moisture state at the bond surface, which will improve construction efforts and save cost. The results showed that the failure occurrence at the bond increased as the bond surfaces became less rough. This is expected, due to a smoother surface creating a weaker bond strength, making the bond the weakest point.

Table 19. Failure stress and type of failure.

ID	HPC/ Bond Age	Flex Str. (psi)	Ave. Str. (psi)	RQ	Failure Type
STD/HPC-S20H1	7	581.9	691.2	High Roughness	Precast
STD/HPC-S20H2	7	755.5	691.2	High Roughness	Precast
STD/HPC-S20H3	7	672.2	691.2	High Roughness	Precast
STD/HPC-S20H4	7	755.3	691.2	High Roughness	Precast
STD/HPC-S25H1	7	720.3	670.2	Norm. Roughness	Precast
STD/HPC-S25H2	7	646.9	670.2	Norm. Roughness	Precast
STD/HPC-S25H3	7	637.3	670.2	Norm. Roughness	Bond
STD/HPC-S25H4	7	670.2	670.2	Norm. Roughness	P/Bond
STD/HPC-S30H1	7	509.3	545.6	Low Roughness	Precast
STD/HPC-S30H2	7	594.9	545.6	Low Roughness	Precast
STD/HPC-S30H3	7	536.8	545.6	Low Roughness	Precast
STD/HPC-S30H4	7	541.4	545.6	Low Roughness	Precast
STD/HPC-A20H1	7	761.7	698.7	High Roughness	Bond
STD/HPC-A20H2	7	692.1	698.7	High Roughness	Precast
STD/HPC-A20H3	7	656.3	698.7	High Roughness	Precast
STD/HPC-A20H4	7	684.6	698.7	High Roughness	Precast
STD/HPC-A25H1	7	731.7	666.5	Norm. Roughness	Bond
STD/HPC-A25H2	7	582.8	666.5	Norm. Roughness	Precast
STD/HPC-A25H3	7	687.0	666.5	Norm. Roughness	Precast
STD/HPC-A25H4	7	664.5	666.5	Norm. Roughness	Bond
STD/HPC-A30H1	7	690.6	657.1	Low Roughness	Bond
STD/HPC-A30H2	7	633.7	657.1	Low Roughness	P/Bond
STD/HPC-A30H3	7	636.0	657.1	Low Roughness	Bond
STD/HPC-A30H4	7	668.3	657.1	Low Roughness	P/Bond

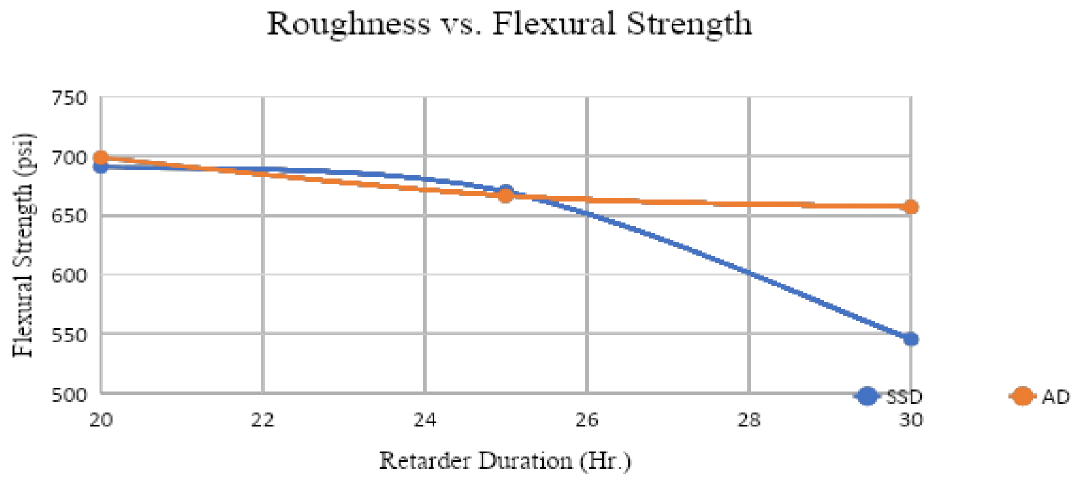

Figure **26. *Plot of flexural strength vs retarder duration.***

The results shown in Table 20 display the progression of the flexural strength with the increase in the bond age of the concrete. These data points were picked from a wide set of beams consisting of identical properties outside of the bond age. The result from the different beams showed a linear progression between the 7th and 28th bond age. The flexural strength exhibits an increase of 36% as the bond age goes from 7 to 28 days. From our large data set, the tendency of the failures within the bond decreases with the increase in bond age. This is due to the curing enhancing the bond strength, making the precast member the weakest point in the connection. In Figure 26, the curve of our data is compared to previous studies and the results to the commonly used slant shear and pull-out test. The curve for our data is represented by the orange curve. As seen in Figure 26, the trend and slope of our data coincides with the expected rate in increase of the bond strength. As well, the pattern in failure type aligns with that of the previous test. If the flexural testing can give us the expected behavior of the concrete bond, then the use of the 4-point bending test becomes ideal due to its simplicity and the consistency in the results.

Table 20. Flexural strength progression with increase in the bond age of the concrete.

ID	HPC Age	Flex Str. (psi)	Ave. Str. (psi)	Failure %
STD/HPC-07D1	7	720.3	670.2	Precast
STD/HPC-07D2	7	646.9	670.2	Precast
STD/HPC-07D3	7	637.3	670.2	Bond
STD/HPC-07D4	7	670.2	670.2	P/Bond
STD/HPC-18D1	18	675.7	745.3	Precast
STD/HPC-18D2	18	830.1	745.3	Precast
STD/HPC-18D3	18	727.7	745.3	P/Bond
STD/HPC-18D4	18	748.3	745.3	Precast
STD/HPC-28D1	28	927.1	917.6	Precast
STD/HPC-28D2	28	931.6	917.6	Bond
STD/HPC-28D3	28	1006.6	917.6	Bond
STD/HPC-28D4	28	805.3	917.6	Precast

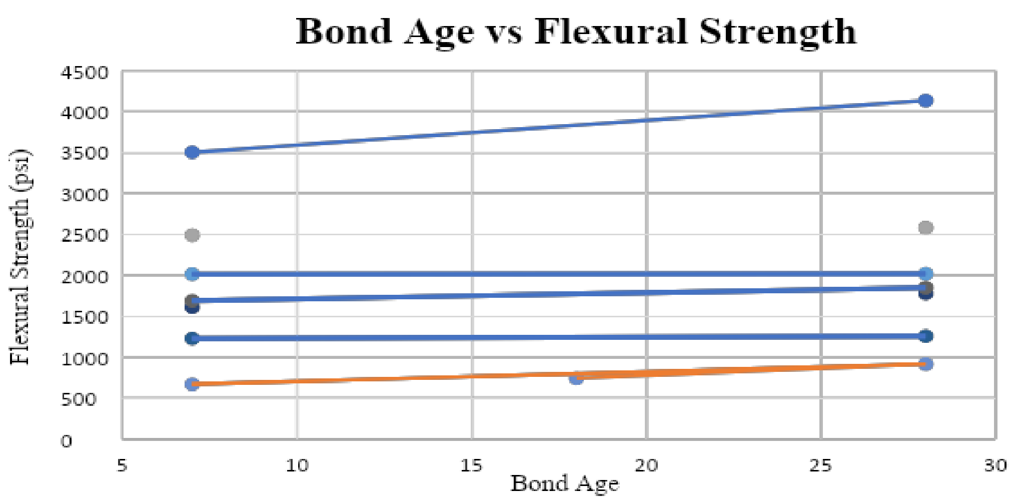

Figure 27. ***Plot of flexural strength vs bond age.***

The critical point in any structural design is ensuring the adequate strength, safety, and durability. As we investigate ensuring the durability of the concrete, we must focus on the major cause of this issue, which is cracking from stresses within the concrete. Cracking within the concrete leaves it exposed to penetration from detrimental substances, which causes a serious threat to the long-term performance of the concrete. These stresses that cause cracking can be obtained from the shrinkage of the concrete as it hydrates. Although the properties and components within the UHPC help make the concrete resistant to shrinkage from hydration, this matter must still be accounted for. With the certain amount of shrinkage that will occur, internal stresses will happen due to the opposite forces that are present at the bond interface. In order to properly track the stresses and cracking behavior of the concrete, we propose the use of the dual ring restrained shrinkage test. This test allows the user to track the strains and crack growth of the concrete while replicating restrained conditions. With the use of a circular geometry, we eliminate the corner stresses. Strain gauges are incorporated into the testing to collect the stresses at specific areas and correlate the data to the stress experienced at the joint and bond. The concrete is cast within two steel rings on a steel base with string gauges inserted to read the strain and cracking patterns within the concrete. The guidelines and dimension for this test follow AASHTO T363 (2017).

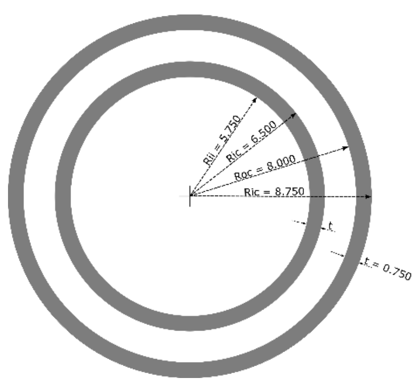

Figure 28. ***Dimension of steel rings.***

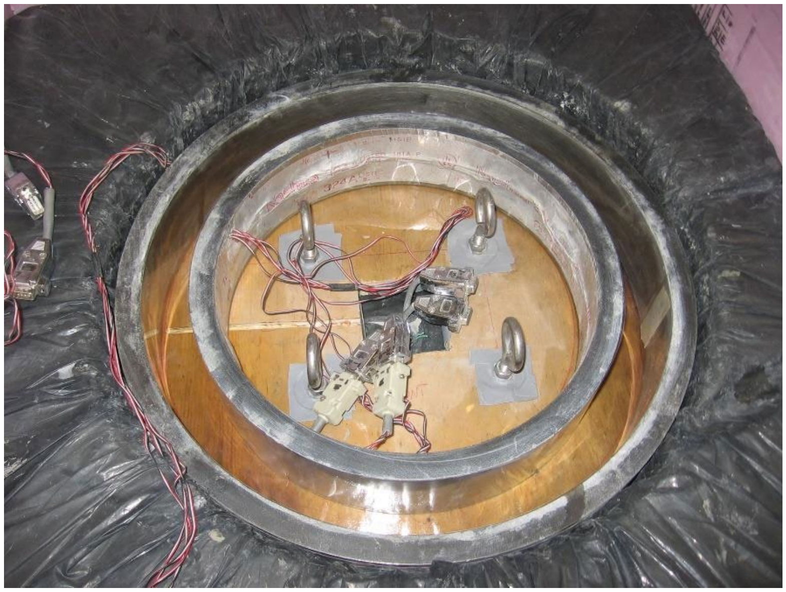

Figure **29. Image of dual ring test.**

2.3 COMPRESSIVE STRENGTH TESTS

During this project a great deal of emphasis was placed on accurately preparing and testing compression specimens. This was due to the convenience of making and testing specimens and comparing the results to previously reported data on UHPC compressive strength performance. Tamping and vibration tables were not utilized when consolidating specimens, since both the UHPC mixes were self-consolidating. Notably, vibration was shown to negatively affect the performance of UHPC because it can cause uneven fiber reinforcement distribution throughout the mixture.

The procedure for casting all UHPC cubes and cylinders followed a consistent practice reported by Cor-Tuf, ASTM, and FHWA's research. Once the concrete was poured into each mold, the specimens were covered on all sides by either their molds or caps and plastic covers. Each cube or cylinder was removed from its respective mold and placed into a moist-curing chamber at the 24- to 36-hour mark, depending on readiness. After appropriate maturity of the UHPC cylinders and cubes was reached, the specimens were removed from the curing chamber.

Detailed attention was placed on preparing the surfaces for all tested cubes and cylinders. Cubes were prepared by using a sanding belt to remove minor surface imperfections and to square up the corners and sides of the cube. Fully prepared cube specimens appear in Figure 30. Preparing cylinders involved a more involved approach to ensure proper conditioning prior to testing. Cylinders were either prepared using a concrete end grinder or concrete saw as discussed in the previous section. This involved removing a small portion of the cylinder's height so that the top and bottom circular sides were parallel to each other and perpendicular to the cylinder's axis along the height. This was checked and adjusted using a level and speed square tool shown in Figure 31.

Figure 30. UHPC specimens prepared on the sanding belt prior to testing.

Figure 31. Lab procedure to determine suitability of UHPC cylinders using a level and speed square layout tool.

Table 21. Average compressive strength (psi) results for the proprietary UHPC mixes.

		4-2-21	5-3-21	6-3-21
3 Day	Cylinder	-	-	-
3 Day	Cube	-	11,868	-
7 Day	Cylinder	12,859	-	-
7 Day	Cube	-	15,729	-
14 Day	Cylinder	-	17,472	-
14 Day	Cube	16,300	-	22,626
28 Day	Cylinder	15,349	19,028	-
28 Day	Cube	16,992	17,179	23,109

Table 22. Average compressive strength (psi) results for the non-proprietary UHPC mix.

		6-8-21
7 Day	Cylinder	12,312
7 Day	Cube	-
14 Day	Cylinder	13,790
14 Day	Cube	15,941
28 Day	Cylinder	16,439
28 Day	Cube	17,435

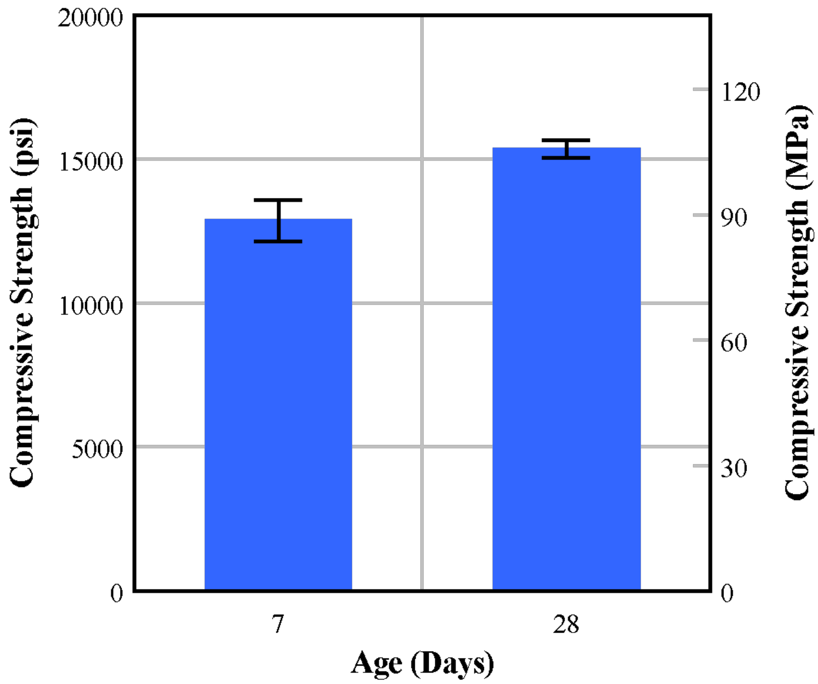

Figure 32. Cylinder compressive test results for 4-2-21 proprietary UHPC mix.

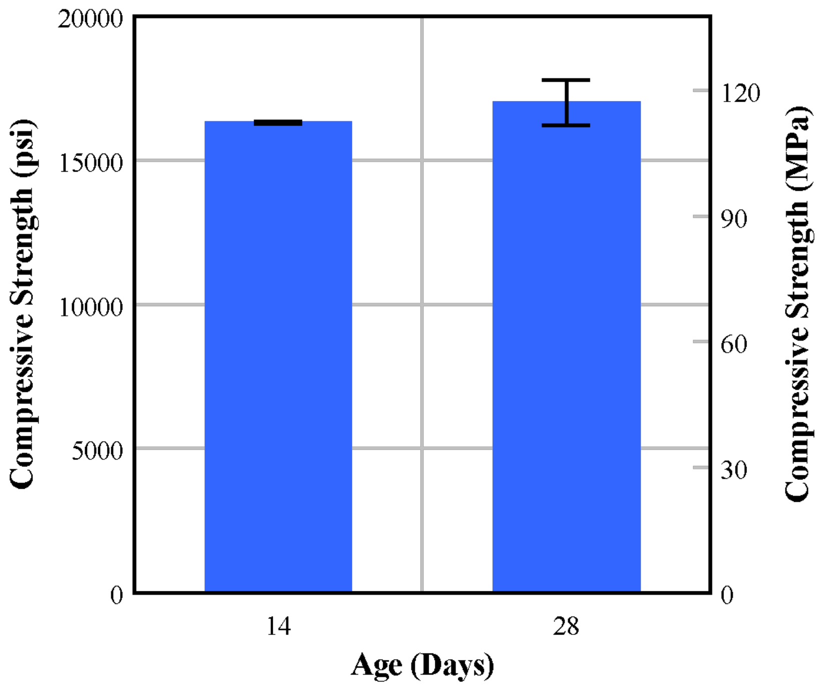

Figure 33. Cube compressive test results for 4-2-21 proprietary UHPC mix.

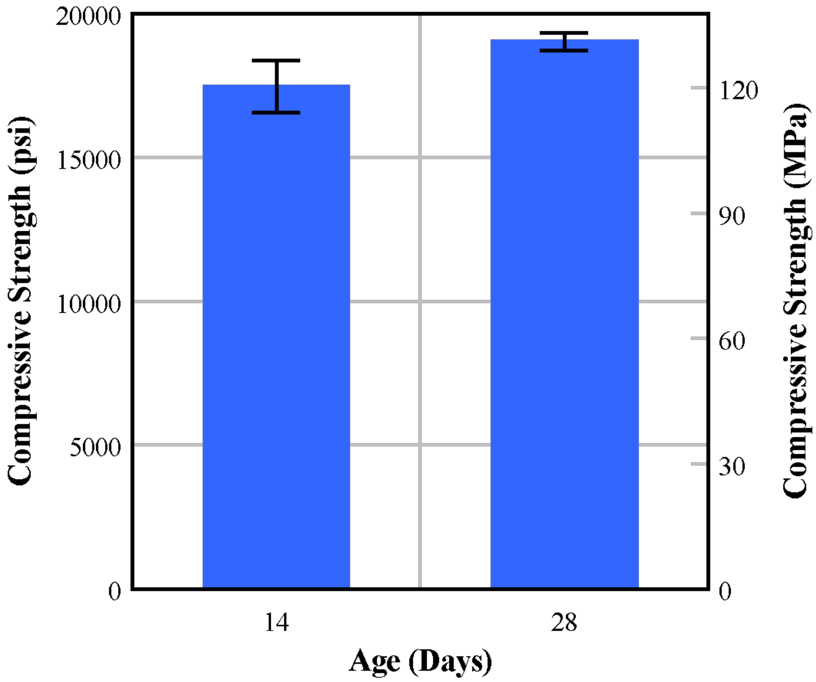

Figure 34. Cylinder compressive test results for 5-3-21 proprietary UHPC mix.

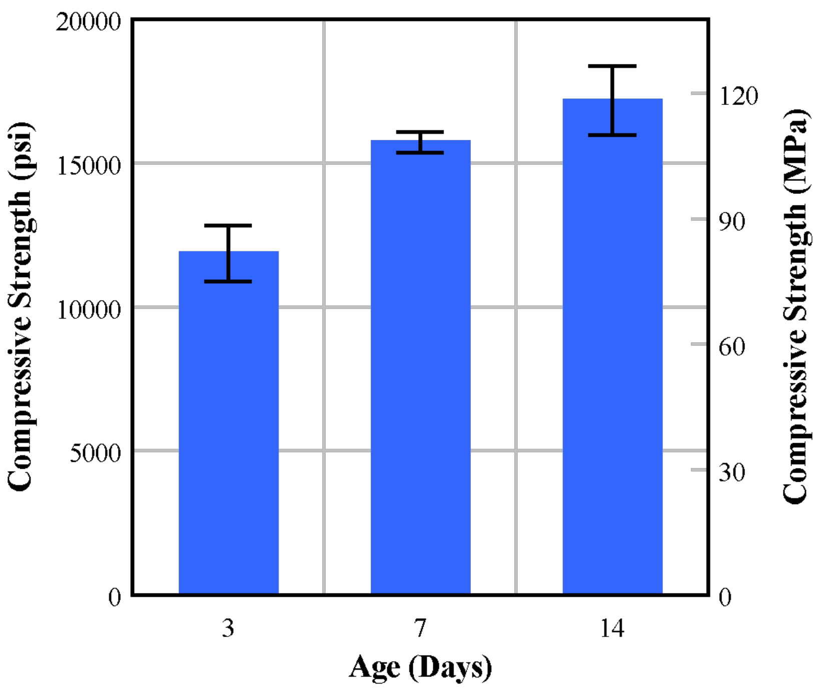

Figure 35. Cube compressive test results for 5-3-21 proprietary UHPC mix.

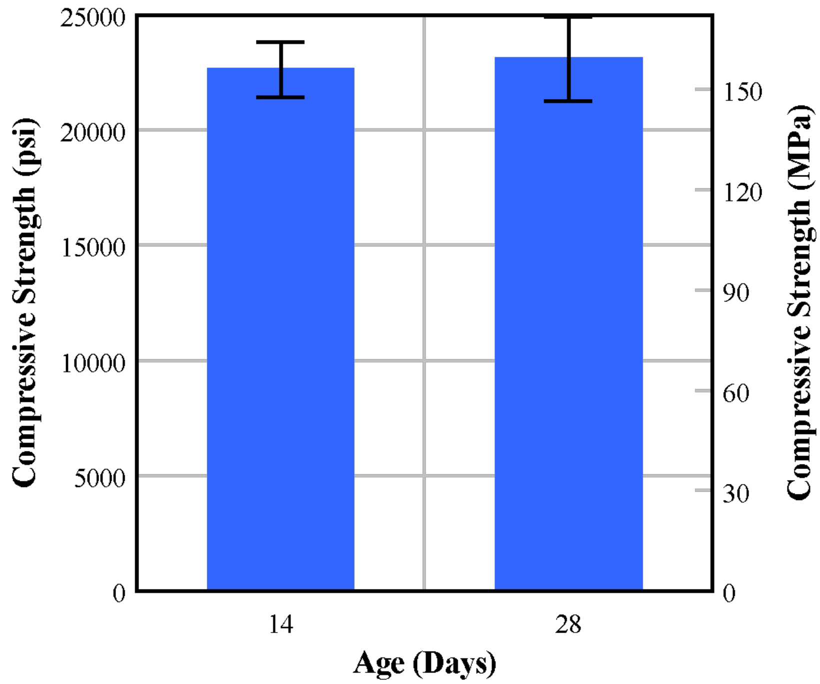

Figure 36. Cube compressive results for 6-3-21 proprietary UHPC mix used in pull-out tests.

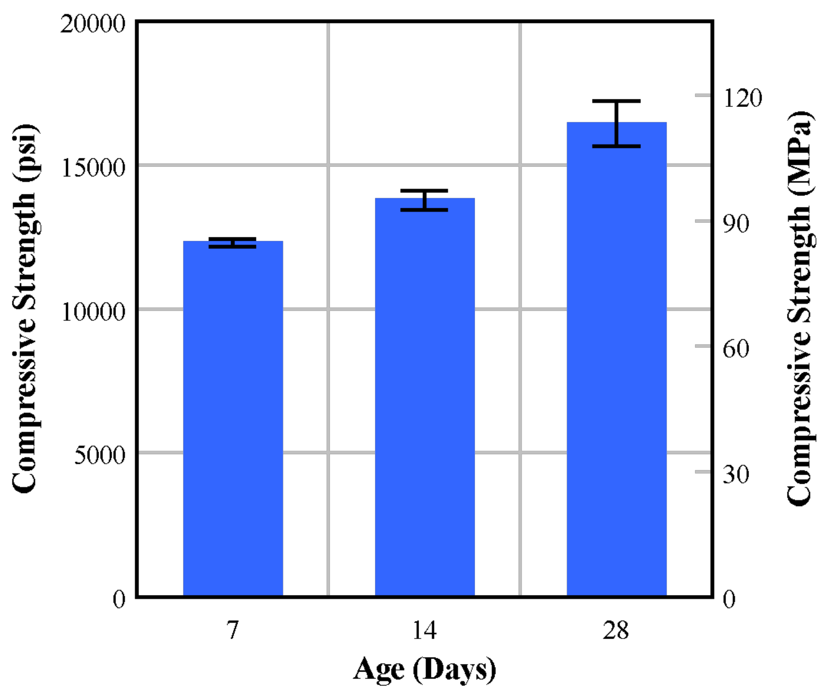

Figure 37. Cylinder compressive results for 6-8-21 non-proprietary UHPC mix used in pull-out tests.

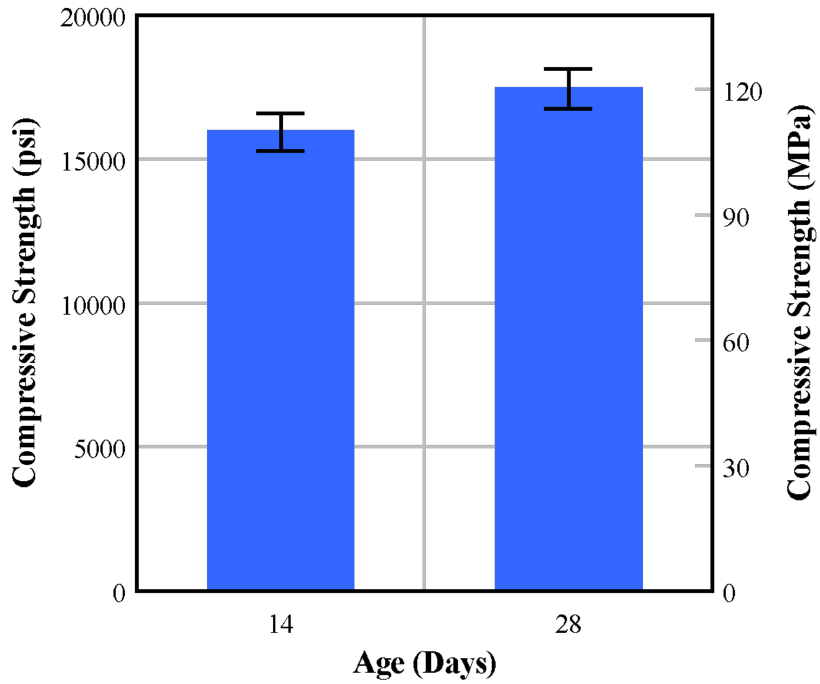

Figure 38. Cube compressive results for 6-8-21 non-proprietary UHPC mix used in pull-out tests.

2.4 TENSILE STRENGTH TESTS

For measurement of tensile strength in non-proprietary UHPC, two measurements were used. The direct tensile strength was measured using dog-bone specimens and correlated with the tensile strength calculated based on an inverse analysis of the stress-strain curve in flexure.

2.4.1 Direct Tensile Assessment

To determine the response of UHPC to direct tensile stresses, 18” by 3” by 2” dog-bone prisms were designed, with a 2” by 2” cross-section and 6” gauge length based on recommended sample size from Zhou and Qiao (Zhou & Qiao, 2018). Figure 39 shows the test specimens.

Figure 39. Direct tension test specimens designed.

The loading was applied to the dog-bone specimens using an MTS Criterion load frame with a 100 kN load cell. 3D Digital image correlation (DIC) was used to determine the strain in the front face of the gauge section in the UHPC. The stress applied was calculated based on the measured load in the load cell using the narrowest cross-section.

2.4.2 Prism Third-Point Bending Tests

Prism flexural tests were conducted for three proprietary mixes and one non-proprietary mix, discussed in the previous section. These tests were performed on 12 total specimens, 9 of which were proprietary and 3 that were non-proprietary. The flexural tensile performance was examined throughout these tests and was used to determine each mix's tensile performance. The prisms detailed in this section all failed in a desirable fashion within the middle third portion of the specimen. The test setup and instrumentation are outlined below.

Third-point (4-point bending) tests were conducted on multiple prisms cast for each mix. The prisms were all 14" long with a 4" by 4" cross section and were tested on a 12" span. Each prism was supported on both sides of the middle third of the prism, while the point loads were applied at the two ends of the span. The full testing setup is shown in Figure 16 and Figure 34. Each third of the span was a 4-inch segment, of which the middle third was the primary region of importance. This was because the maximum bending stresses occurred in the middle third due to the loading configuration.

One linear variable differential transformer (LVDT) was placed on either side of the span's mid-point and two uniaxial strain gauges were located on the bottom tensile face of the middle third. The strain gauge used was a 20CLW gauge from Micro-Measurements with a grid resistance of 120 ohms. The strain gauges were 2” in length and staggered so that the entire 4” middle third portion of the span was covered. The support conditions, loading conditions, LVDT locations, and strain gauge placement on the tensile face are shown in Figure 38.

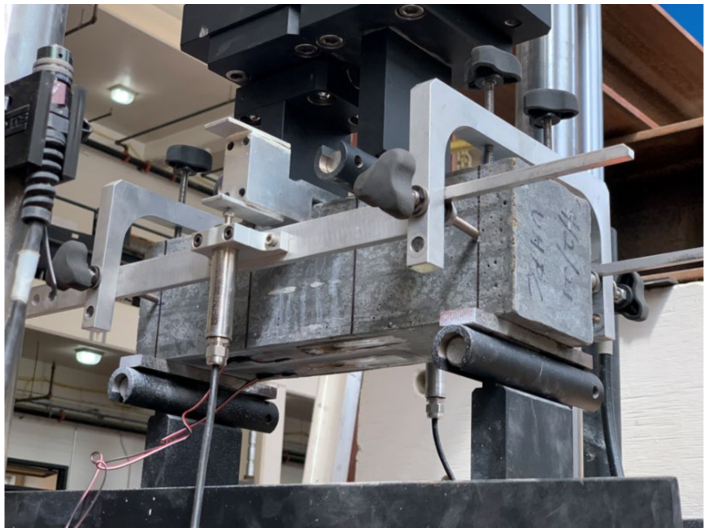

Figure ***40. Third-point bending test on Instron Testing Machine with two uniaxial strain gauges at midspan.***

2.4.3 Equivalent Bending Stress Versus Midspan Deflection Results

The flexural tensile behavior for all 12 specimens followed an expected pattern consisting of elastic, strain-hardening plastic, and strain-softening plastic behavior. The steel fiber reinforcement was largely responsible for the strain-hardening behavior and increased tensile ductility common to UHPCs. The entire set of results from the prism flexural tensile testing is summarized in Figure 41 through Figure 44.

During the tests, the prisms were observed to see the fibers bridging the cracks within the tensile stress region of the span. These discontinuous fibers allowed the prisms to withstand a significant amount of cracking before the load capacity was reached. The failure pattern within all twelve prisms involved small cracks that formed on the tensile face of the prism. Eventually, a predominant crack started to form and gradually grew larger and wider until failure. Figure 43 shows the typical condition of a failed prism.

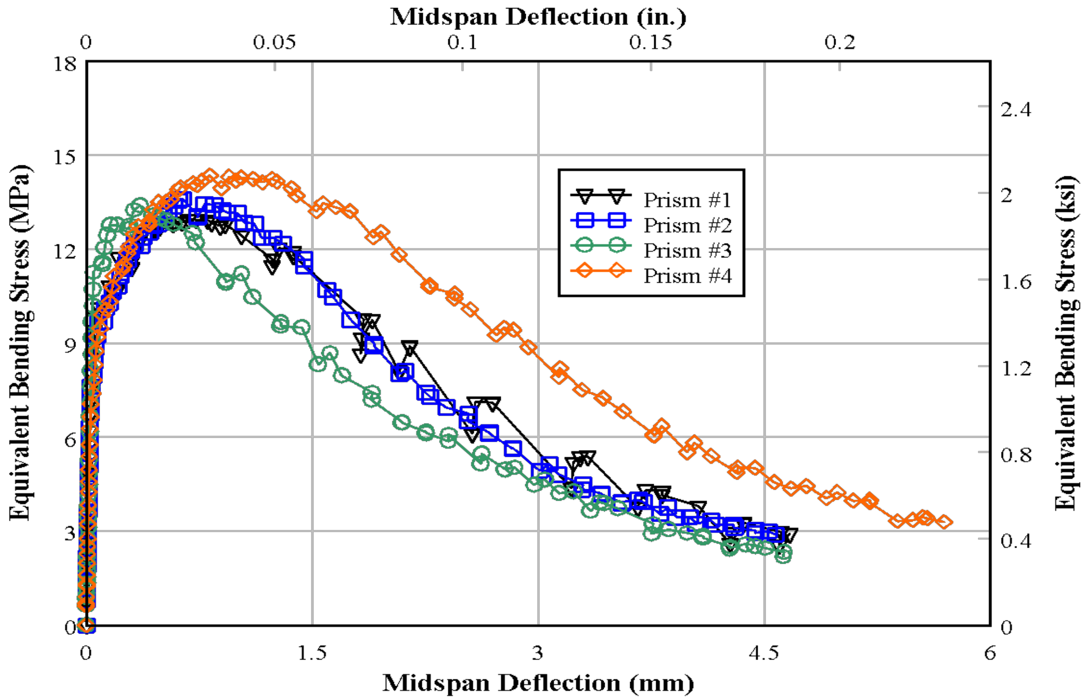

Figure 41. Third-point bending tests for 4-2-21 proprietary UHPC mix.

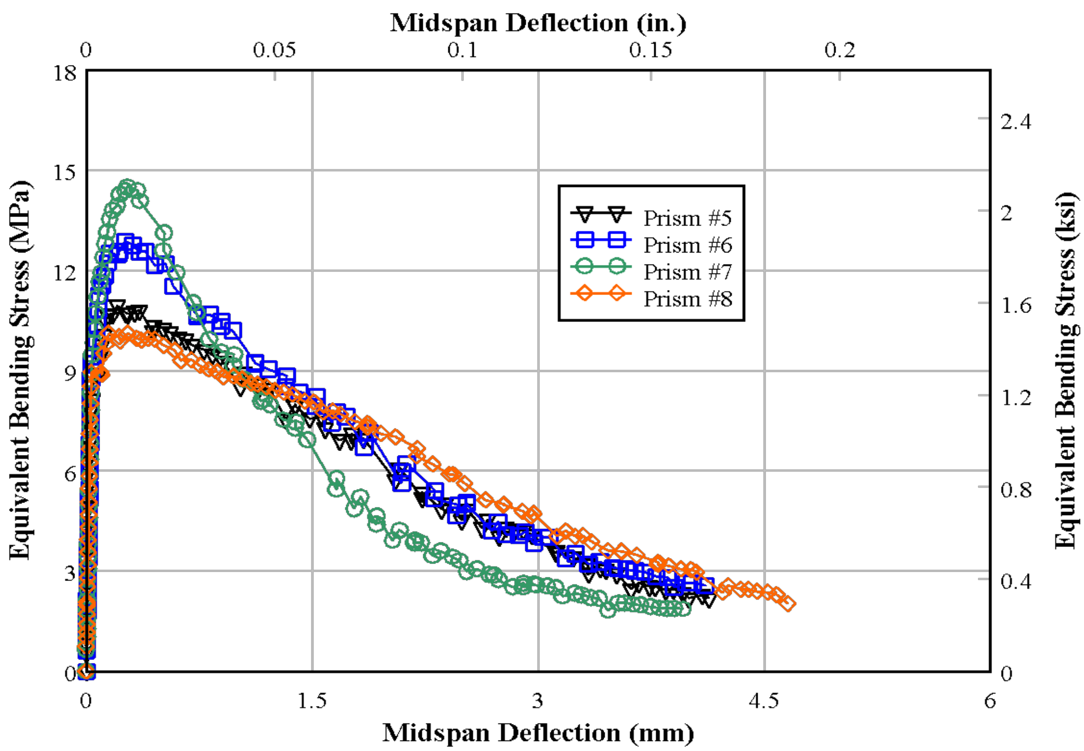

Figure 42. Third-point bending tests for 5-3-21 proprietary UHPC mix.

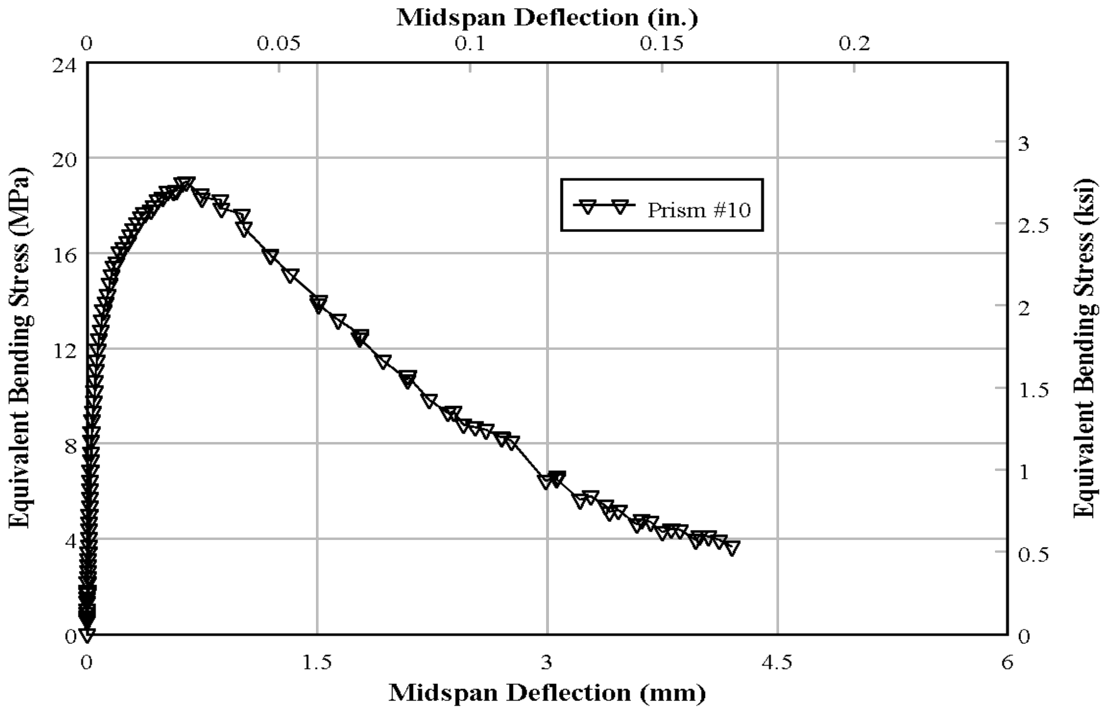

Figure 43. Third-point bending test for 6-3-21 proprietary UHPC mix.

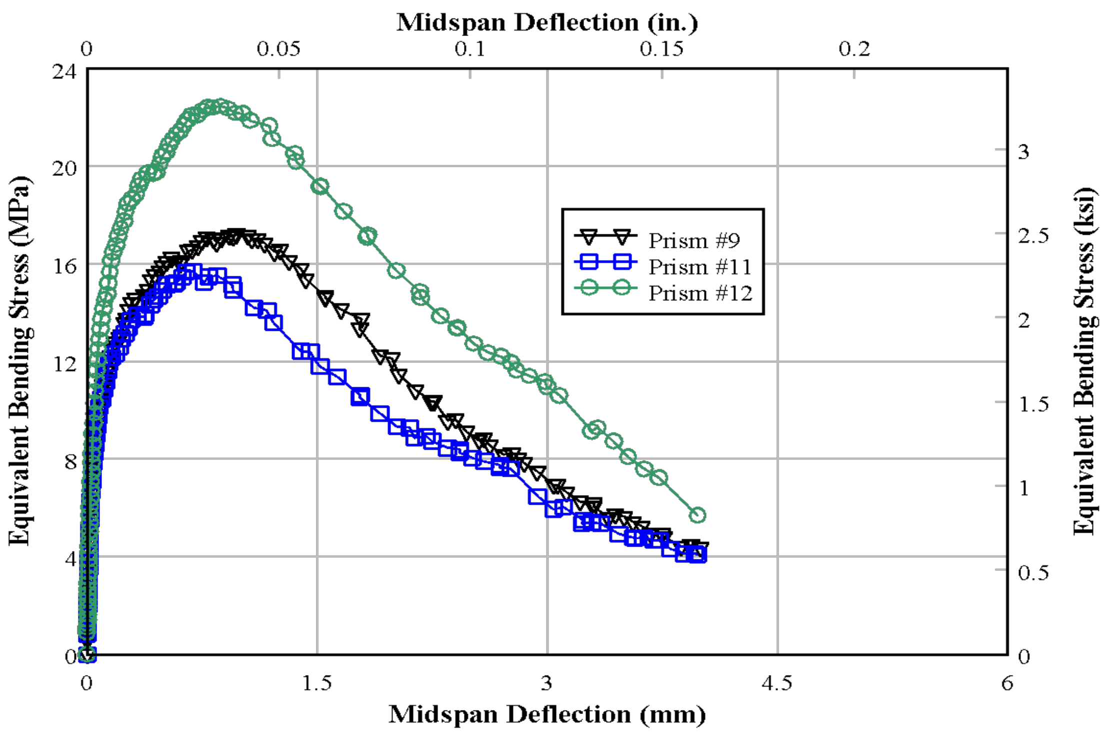

Figure 44. Third-point bending tests for 6-8-21 non-proprietary UHPC mix.

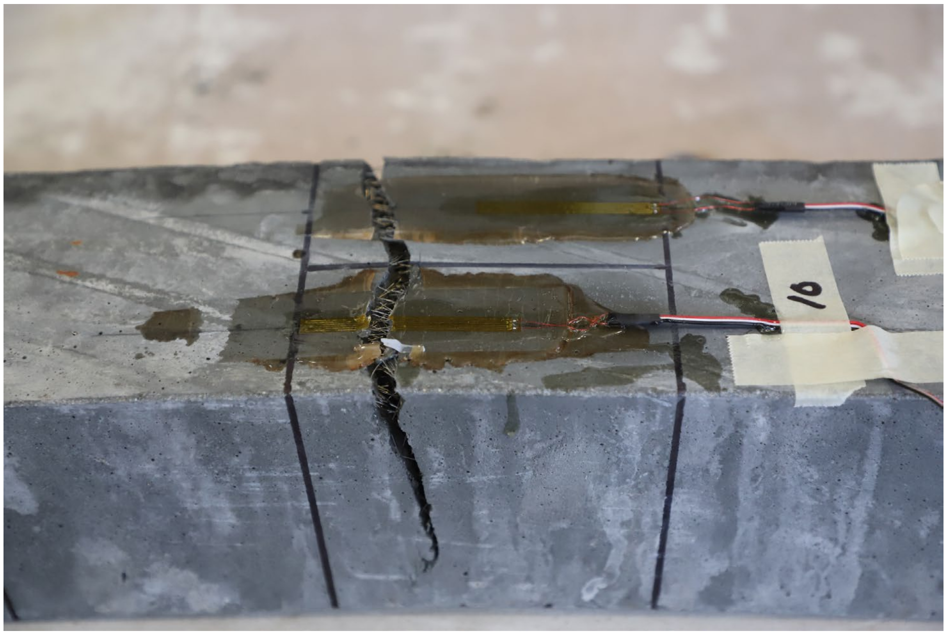

Figure 45. Completed prism test with crack occurring in the middle third of the specimen.

2.5 REBAR PULL-OUT TESTS

Twenty individual rebar pull-out tests were performed to quantify the structural bond integrity of the steel rebar reinforcement embedded in the particular UHPCs used (Haber and Graybeal 2018) with both a proprietary and non-proprietary UHPC mix and rebar. Additionally, the associated failure mechanisms related to the material and geometric properties of the test setup were evaluated through the data collected during the pull-out test and visual inspection (Peruchini et al. 2017). The various bond failure mechanisms considered are listed in the previous sections. More details about the fabrication and construction of specimens are listed in (Dennis 2022).

2.5.1 Reinforcement Uniaxial Tensile Testing

Prior to the start of rebar pull-out testing, the epoxy-coated and uncoated reinforcement bars were tested to confirm their uniaxial tension properties. The testing was performed using the Tinius Olsen Universal Testing Machine and GOM Aramis digital image correlation equipment and software. Tensile stress versus strain data was collected for the epoxy-coated and uncoated #5 bars to observe each bar's yield and ultimate points. The data presented in Figure 46 show the representative tensile performance of the #5 pull-out rebar used in all the rebar pull-out tests.

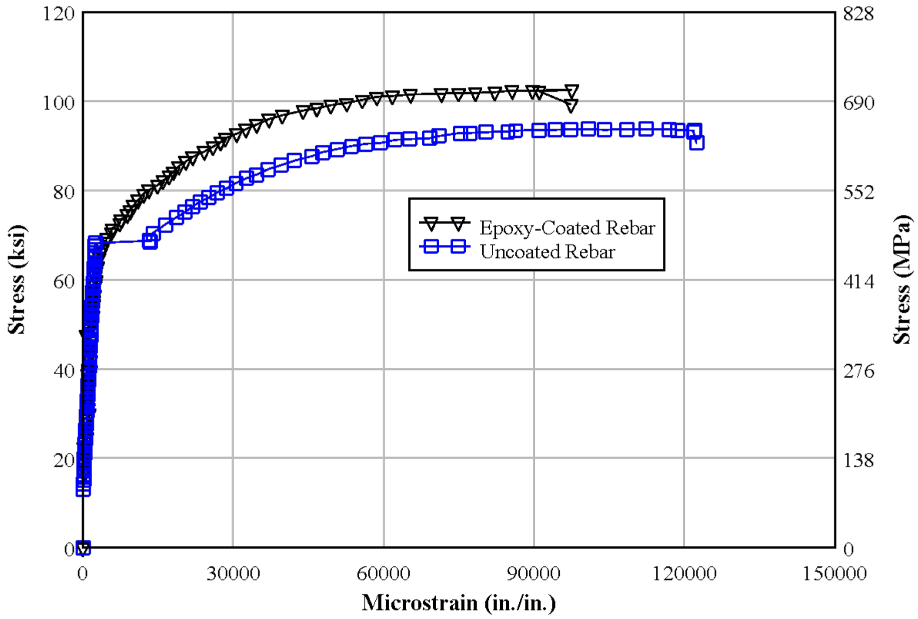

Figure ***46. Uniaxial tensile stress versus strain for the epoxy-coated and uncoated rebar.***

The two different reinforcement bars performed slightly differently in terms of yield and ultimate strength. The epoxy-coated rebar had a yield strength of approximately 65 ksi and an ultimate strength of approximately 102 ksi. Alternatively, the uncoated rebar had a higher yield strength of about 68 ksi but a lower ultimate strength of 93 ksi. Each reinforcement bar tested failed by necking in the reinforcement and eventual fracture. The yield strength data were used for subsequent calculations instead of using the manufacturer-designated 60 ksi yield strength.

The pull-out tests were conducted on the Tinius Olsen Universal Testing Machine under a constant displacement loading rate of 0.2 in./min. Two LVDT displacement transducers (DCTH400AG) from RDP Electrosense were used to capture the displacement at each loading interval. Both LVDTs were attached to the rebar with a clamping mount and arranged on opposite sides of the tested rebar as shown in Figure 47.

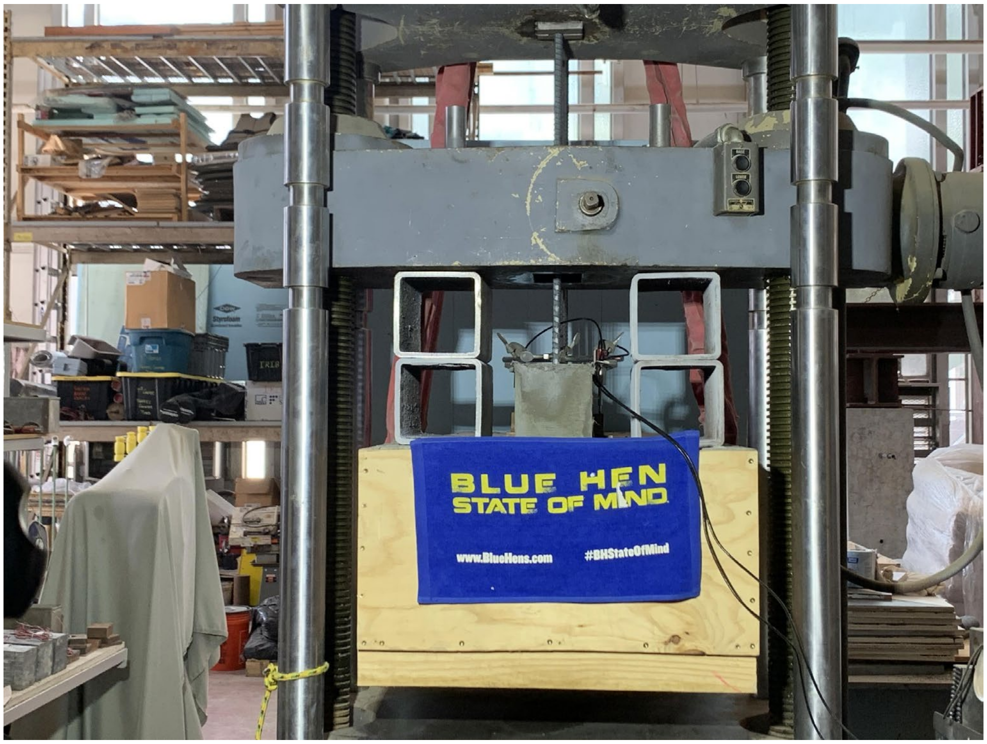

Figure 47. Rebar pull-out test setup.

The tests were conducted by holding the extended rebar end in place with one crosshead while the other crosshead applied the vertical pull-out force until failure. As each rebar was pulled out of the UHPC strip, the LVDTs captured the vertical movement of the rebar relative to the top of the concrete surface. The published displacement data represent an average of the displacement reading at each loading step between the two LVDTs.

Four particular pull-out test configurations were developed during the fabrication process. For each of the four configurations, five individual pull-out tests were conducted, resulting in a total of 20 tests. The four unique testing scenarios were as follows: proprietary mix with epoxy-coated reinforcement, proprietary mix with uncoated reinforcement, non-proprietary mix with epoxy-coated reinforcement, and non-proprietary mix with uncoated reinforcement (Figures 48 through 51).

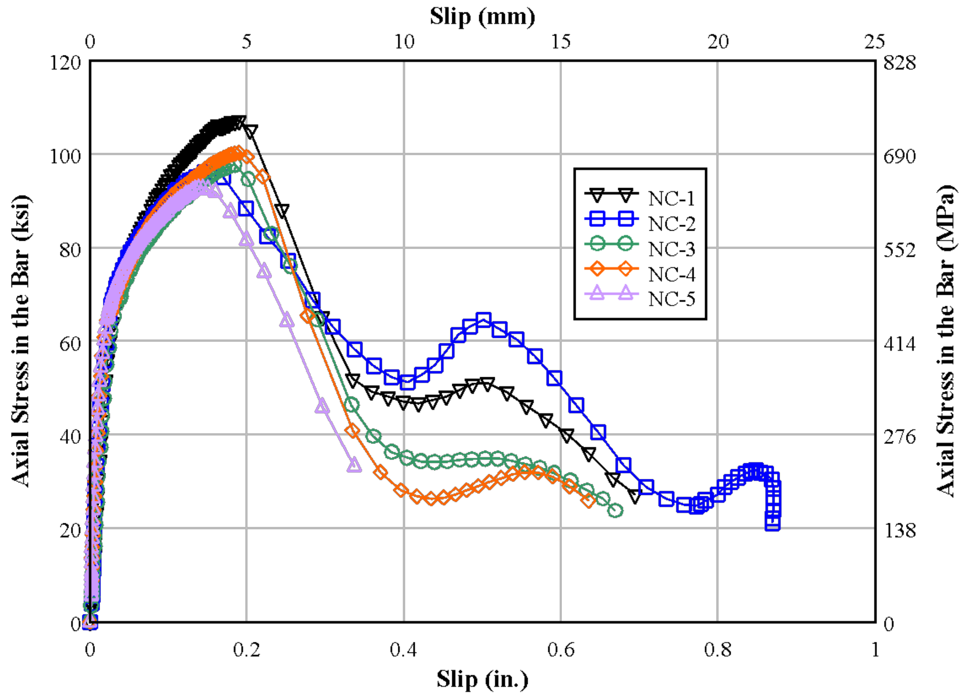

Figure *48. Stress versus slip response from the non-proprietary coated rebar pullout tests.*

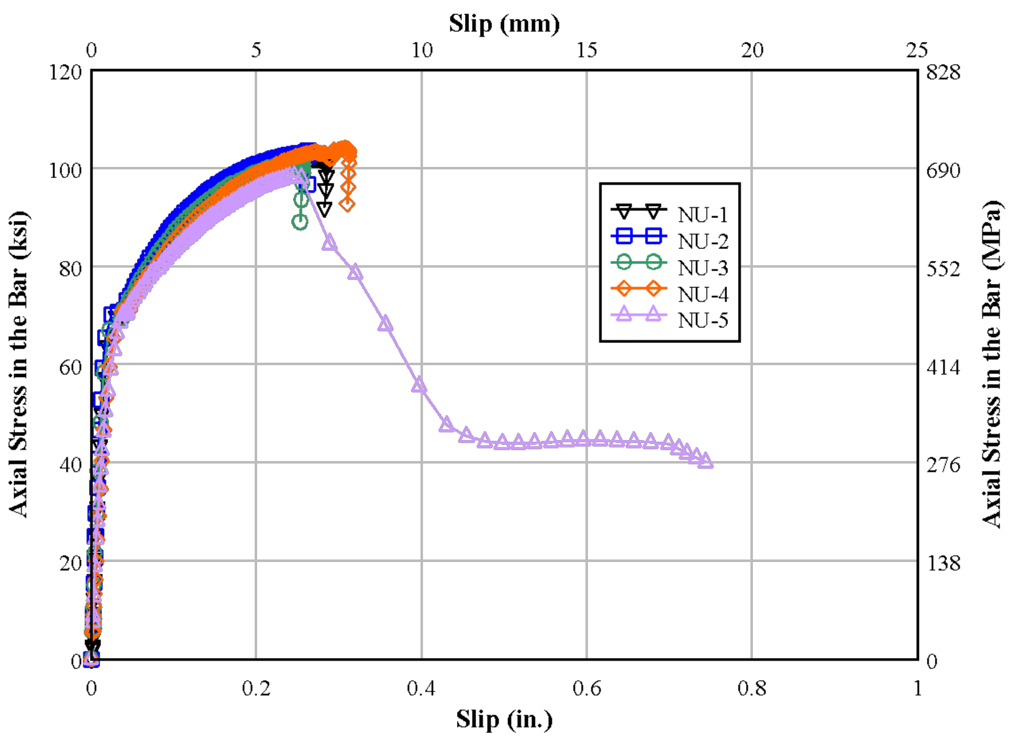

Figure *49. Stress versus slip response from the non-proprietary uncoated rebar pullout tests.*

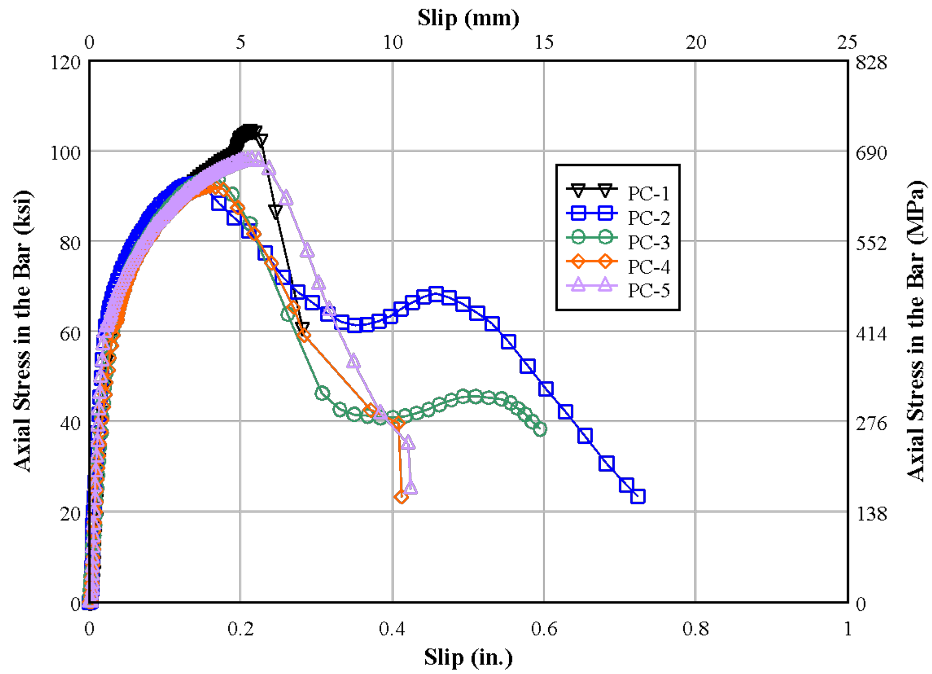

Figure 50. Stress versus slip response from the proprietary coated rebar pullout tests.

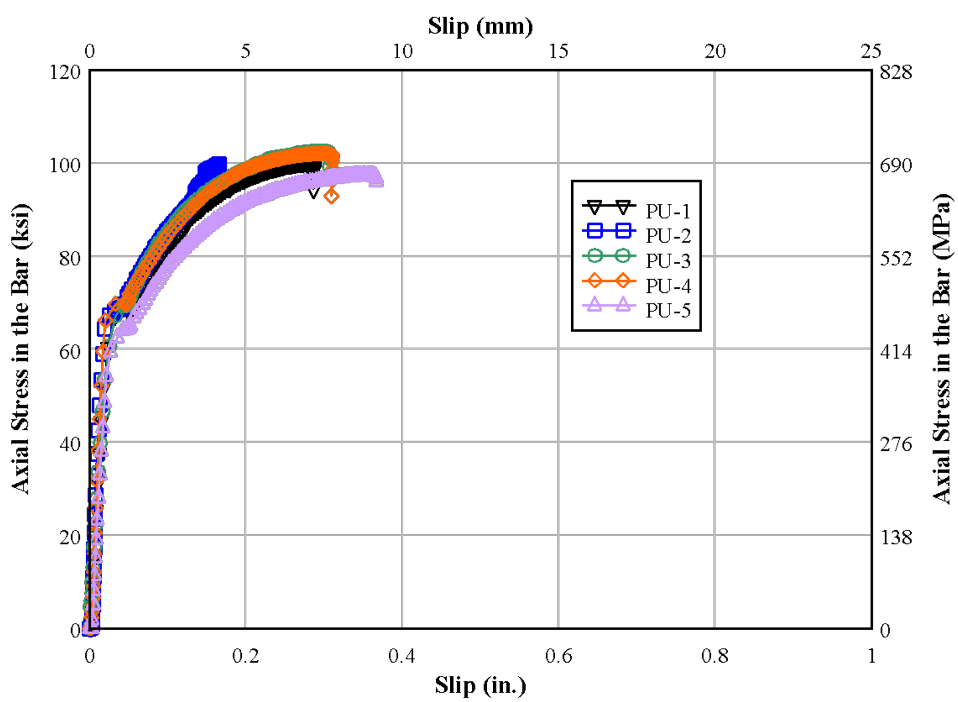

Figure 51. Stress versus slip response from the proprietary uncoated rebar pullout tests.

2.5.2 Analysis of Results

The failure mode, peak bar axial stress, and bar-UHPC bond strength for all twenty tests were compiled for all 20 tests in Table 23 and Table 24. These data were further analyzed and presented as an average and standard deviation for the four unique testing scenarios. These data are presented in Figure 52 through Figure 55.

Additionally, the representative load-slip behavior for each of the four testing configurations was summarized and compared against pull-out tests conducted by Haber and Graybeal's FHWA research program (Haber and Graybeal, 2018).

The proprietary and non-proprietary UHPC mixes performed very similarly in terms of peak axial stress and bond stress before failure. Also, the overall ductility and loading pattern from start to failure was very similar between the representative curves. These curves summarize the bond performance of both epoxy-coated and uncoated rebar embedded in the proprietary and non-proprietary UHPC shown in Figure 56 and Figure 57.

Table 23. Failure mode, peak bar axial stress, and bond strength for the epoxy-coated rebar pull-out tests.

Test	Failure Mode	Peak Bar Axial Stress (f_{smax}) (ksi)	Bar-UHPC Bond Strength (μ_{test}) (ksi)
PC-1	Splitting	104.7	3,272
PC-2	Splitting	92.7	2,897
PC-3	Splitting	94.0	2,938
PC-4	Splitting	92.1	2,878
PC-5	Splitting	98.0	3,063
NC-1	Splitting	107.2	3,350
NC-2	Splitting	96.8	3,026
NC-3	Splitting	97.8	3,055
NC-4	Splitting	100.2	3,132
NC-5	Splitting	92.7	2,898

Table 24. Failure mode, peak bar axial stress, and bond strength for the uncoated rebar pull-out tests.

Test	Failure Mode	Peak Bar Axial Stress (f_{smax}) (ksi)	Bar-UHPC Bond Strength (μ_{test}) (ksi)
PU-1	Fracture	100.1	3,128
PU-2	Fracture	99.8	3,120
PU-3	Fracture	102.4	3,201
PU-4	Fracture	102.1	3,189
PU-5	Fracture	97.4	3,042
NU-1	Fracture	102.1	3,190
NU-2	Fracture	103.6	3,238
NU-3	Fracture	101.5	3,172
NU-4	Fracture	104.0	3,252
NU-5	Splitting	98.4	3,075

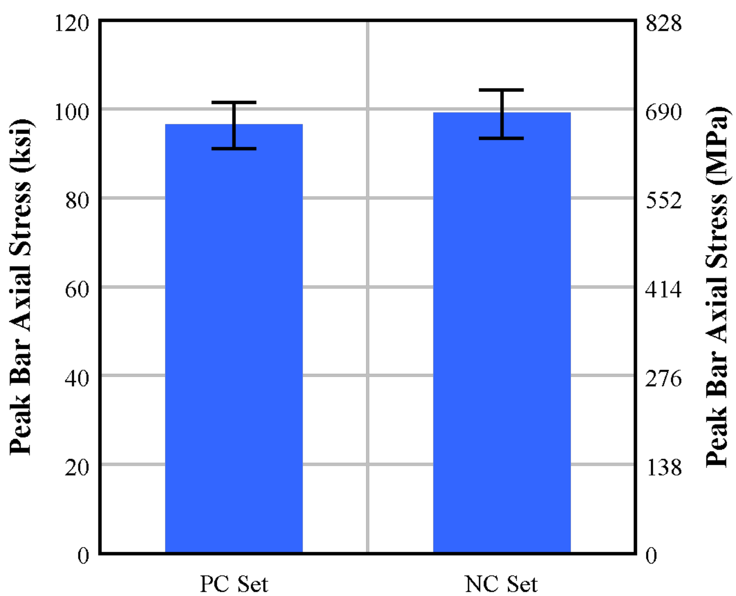

Figure 52. Peak bar axial stress for all epoxy-coated rebar pull-out tests.

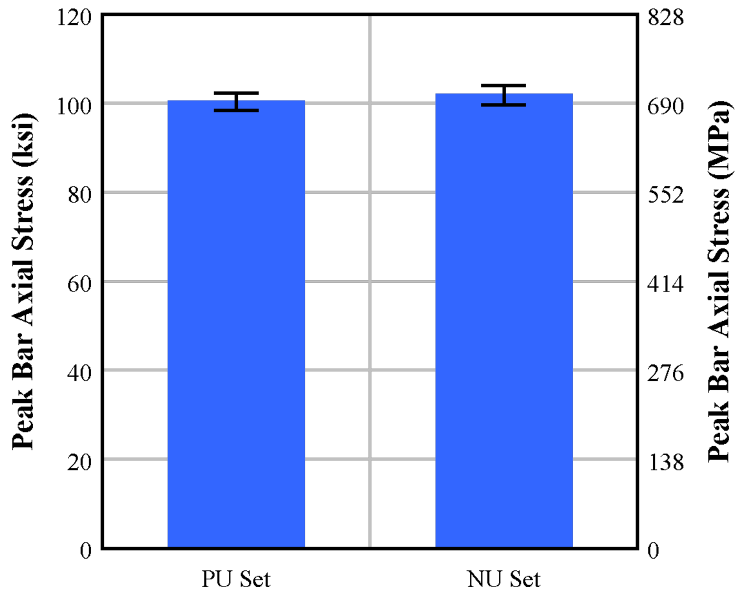

Figure 53. Peak bar axial stress for all uncoated rebar pull-out tests.

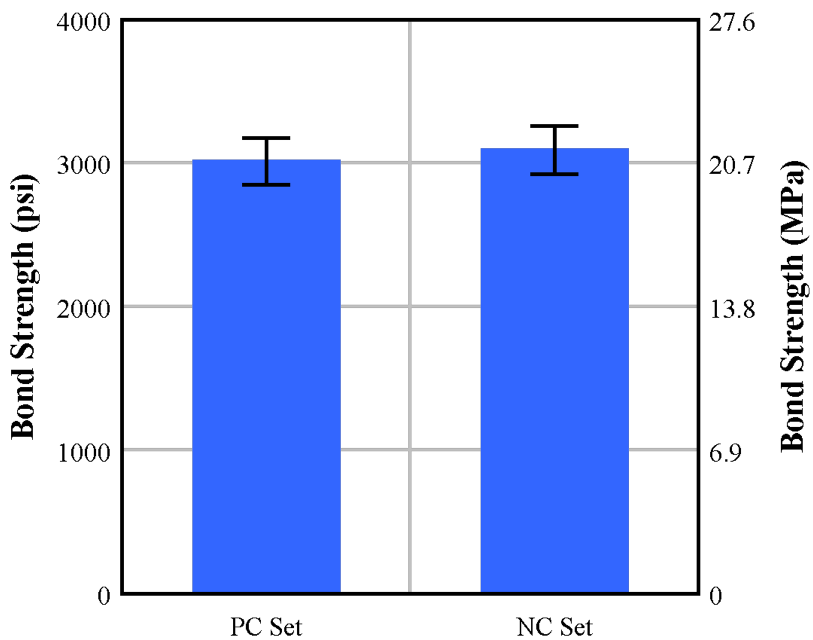

Figure 54. Bar-UHPC bond strength for all epoxy-coated rebar pull-out tests.

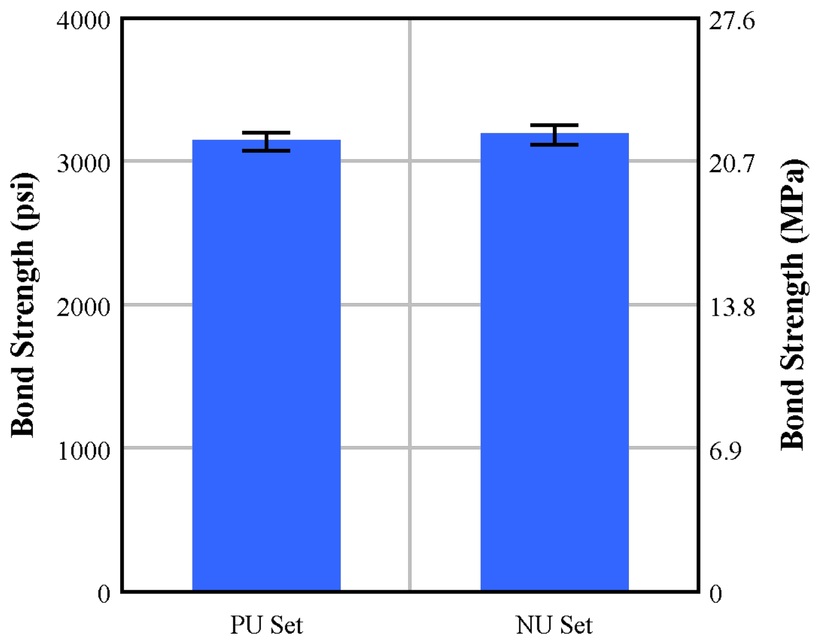

Figure 55. Bar-UHPC bond strength for all uncoated rebar pull-out tests.

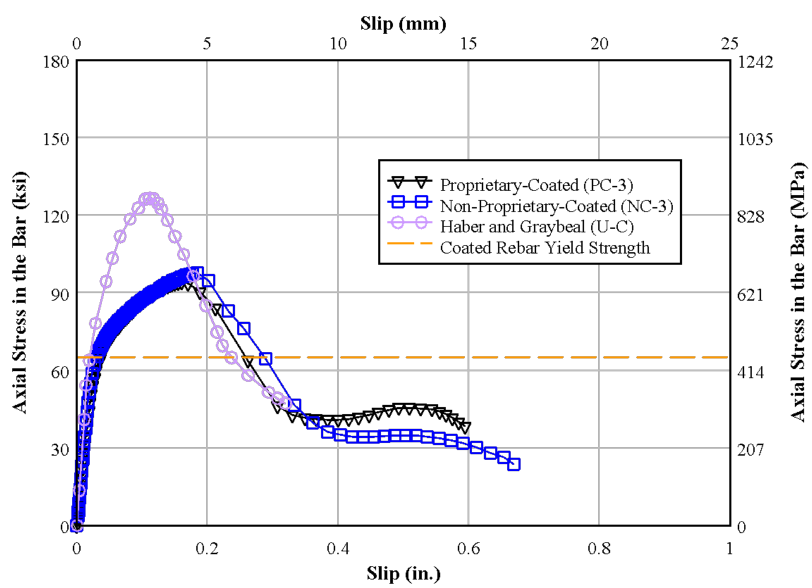

Figure 56. Stress versus slip response for all epoxy-coated rebar pullout tests.

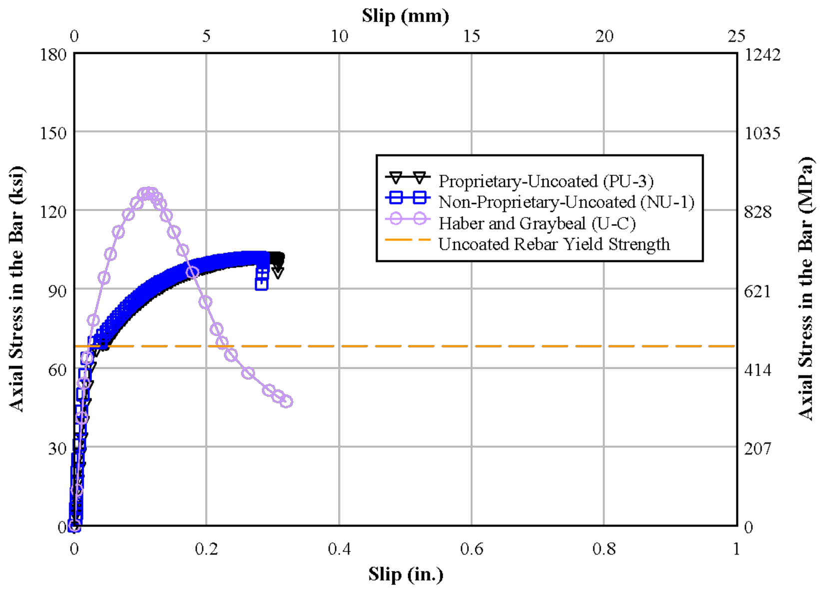

Figure 57. Stress versus slip response for all uncoated rebar pullout tests.

Chapter 3

Findings

3.1 SUMMARY OF EXPERIMENTAL TEST RESULTS

3.1.1 Fresh property characterization at Penn State

The research at Penn State was primarily involved in determining the most optimal mix design for a UHPC in terms of its slump flow and characteristic compressive strength. To determine the most optimal mixture design to be cast at the University of Delaware, trials were conducted using the optimized low-cost UHPC mixtures derived from the statistical model for a target compressive strength of 140 MPa. Firstly, the statistical model was used to determine a working mix design (based on the 99% prediction interval of the model, a predicted mean strength of 175 MPa was chosen, since the standard error of regression is 11.92) and an optimal mix design was chosen based on the modified Andreasen and Andersen particle packing model, as detailed in section 1.3.5. Since the 99% prediction interval was chosen to be conservative, it is likely that only 1% of the mixtures would fall outside of the prediction interval of the model.

Figure 58 represents a comparison between the target optimized UHPC formulations based on the maximum aggregate size (1.18 mm) and the designed UHPC mix with minimum sum of the square of differences (Wibowo and Sritharan 2018), for illustration purposes. The calculated sum of the square of differences is then divided by the sum of the square of the target mix distribution, to obtain the closeness of fit (R^2) between the theoretical and actual mixture design. The low-cost mixtures from 2.1.5.1 were chosen and the closest-fitting mixtures were chosen and further adopted after determining the appropriate superplasticizer dosage.

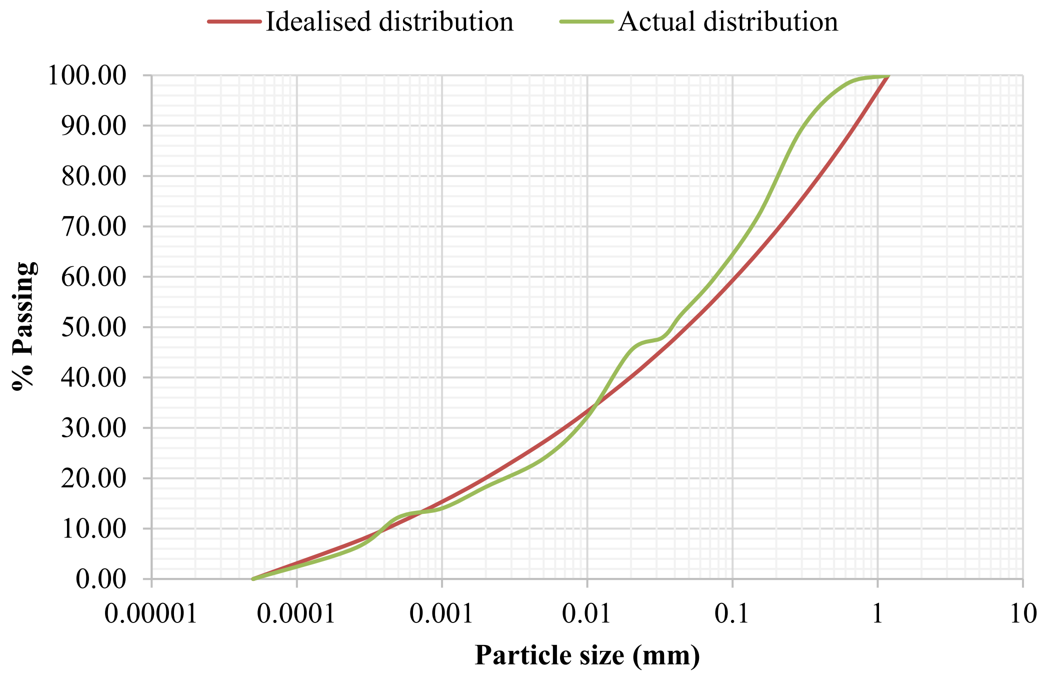

Figure 58. Particle size distributions of the target UHPC mix from modified A&A model and designed UHPC mix (R^2 calculated to be 98%).

Now, since superplasticizer dosage is not determined from the model directly, trial mixtures are conducted to determine the dosage. Superplasticizer is an integral component in obtaining a workable and self-consolidating UHPC. However, the excessive use of superplasticizer can contribute to several issues in the fresh and hardened performance of the concrete. Excessive superplasticizer use contributes to retardation, due to the adsorption of the comb-like polymer structures on the hydrating cement grains and possible complexation of Ca^{2+} ions with PCEs in solution. This leads to deceleration of early-age strength gain (Zhang et al., 2019). In addition, excessive use of superplasticizer is linked to unwanted air entrainment in self-consolidating concrete (Piekarczyk & Łaźniewska-Piekarczyk, 2021). It has been established in previous studies (PP Li, 2018) that an increase in superplasticizer is effective in increasing the workability of UHPC until an optimum. Beyond this value, an increase in superplasticizer is ineffective in improving workability.

Hence, to measure the optimal dosage of superplasticizer required, the UHPC mixtures were mixed, and the static flow was evaluated (by increasing the dosage of superplasticizer from 0.2% to 1.2% by weight of cementitious material). Increase in superplasticizer dosage increases the spread diameter until an optimal value, beyond which there is no improvement (Figure 59) and possible segregation when the mini-slump cone spread is measured. Thus, a superplasticizer dosage that was deemed the minimum required to attain 260-mm static spread was adopted. A summary of the early-age properties of UHPC that were assessed is provided in Table 25.

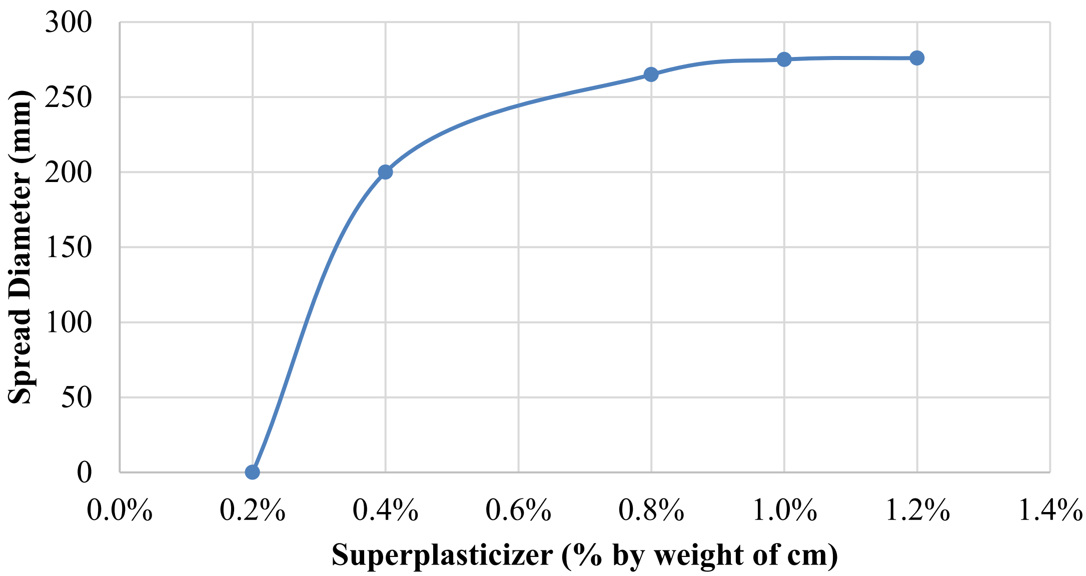

Figure 59. Effect of superplasticizer dosage on spread.

It is noted that by determining the optimal superplasticizer dosage, it is possible to reduce the initial setting time and increase the strength attained at 24 hours' age. Figure 60 represents the effect of increase in superplasticizer dosage on strength measured at 24 hours. With an increase in superplasticizer dosage by 20%, the 24-hour strength dropped by more than 50%. Thus, with the help of an optimal SP dosage, there is a possibility for good trade-off between the maximum achievable flow in a particular mix design and the maximum strength achieved.

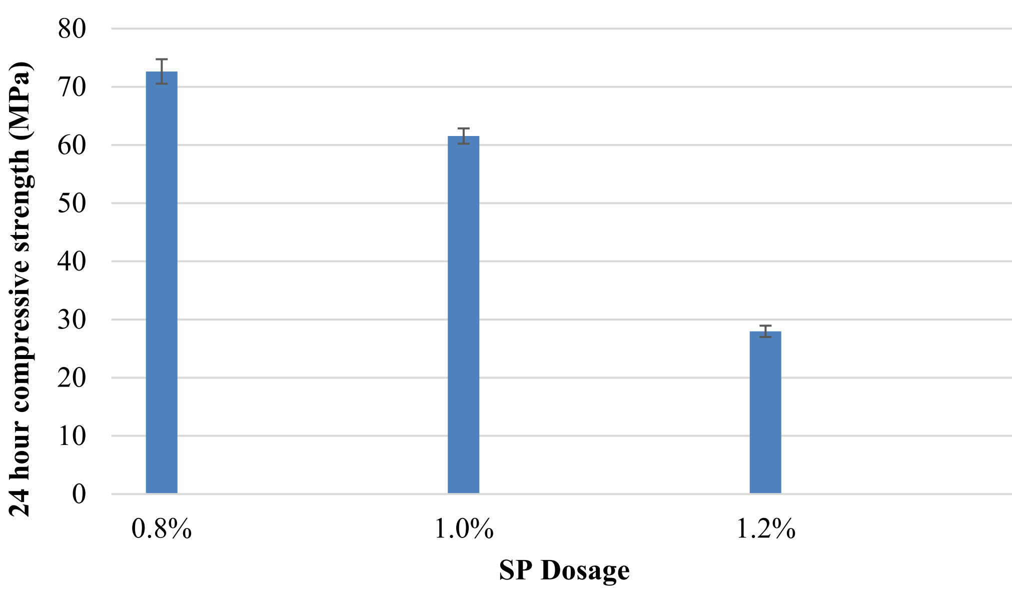

Figure 60. Effect of SP dosage on 24-hour compressive strength.

The final fresh properties of the UHPC mix are detailed in Table 25. It is noted that this UHPC was produced without the use of any set accelerating admixture. The fresh air content of the UHPC mix is still high, possibly due to the higher viscosity of UHPC due to the use of silica fume. The higher viscosity of the UHPC causes the mixture to entrap higher amounts of air. To mitigate this in future castings, it is recommended that a suitable defoaming admixture be used in addition to the use of chilled mixing water, and possibly to improve workability further by use of fly ash. Increase in the flowability of UHPC mixtures increases the wet-packing density and improves self-consolidation of the mixture, decreasing the risk of entrapping excessive air in the UHPC.

Table 25. Summary of measured fresh properties of designed non-proprietary UHPC PSU Mix 1.

Fresh Property	Value
Workability	268 mm (spread)
Fresh Air Content	5.5%
Setting Time	9 hours and 53 minutes

Figure 61 represents the strength development in UHPC mixtures, and it is worth noting that 82% of the compressive strength of the final UHPC is developed at the age of 7 days and the 7-day and 28-day strength of the UHPC mixture was 120±2 MPa and 142±3 MPa, respectively. Modulus of elasticity of the UHPC mixture is approximated using the relationship proposed by the FHWA (Graybeal, 2007). The elastic modulus of UHPC can be approximated using the Equation 8:

$$E_c = 3840\sqrt{f'_c} \qquad \text{Equation 8}$$

where E_c is the elastic modulus expressed in MPa and f'_c is the compressive strength measured in MPa. Using this relationship, E_c is determined as 42 GPa.

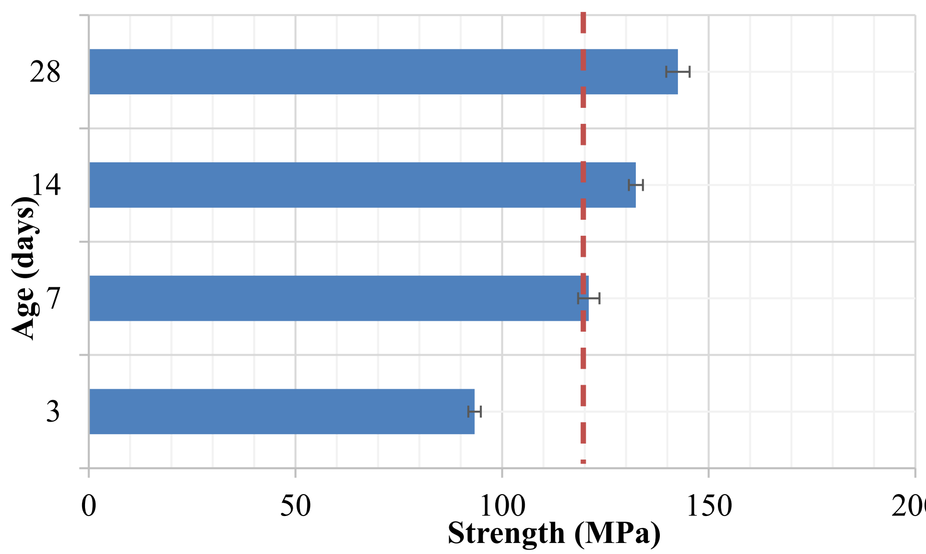

Figure 61. Compressive strength development of non-proprietary UHPC over time (measured on 2" cube specimens).

A summary of the mixture proportions is detailed in Table 26. Initially, dry densified silica fume was utilized for casting the UHPC mixtures, denoted as PSU Mix 1. Since the silica fume agglomerates do not break down adequately inside a pan-mixer due to insufficient energy of mixing, these mixes did not perform as expected, and hence the UHPC mix design was revised. The UHPC Mixes 2 and 3 are the most optimal mixtures for attaining 140 MPa compressive strength. The main difference between Mixes 2 and 3 is the type of fine aggregate used. Mix 3 was cast using the same mixture proportions as Mix 2, but using a higher quality, but coarser quartzite mason sand, to determine equivalent properties of the same mixture used by the University of Delaware of the hardened property testing.

Table 26. Summary of trial mixtures conducted at Penn State.

Ingredient	UHPC Mix 1	UHPC Mix 2	UHPC Mix 3
Water (kg/m^3)	242	193	193
Cement type	ASTM Type II	ASTM Type II	ASTM Type II
Cement content (kg/m^3)	779	770	770
w/c	0.31	0.25	0.25
Silica fume type and content	214	236	236
Limestone filler content	184	311	311
HRWRA (kg/m^3)	9.5	10.5	10.5
Fine agg (type)	Fine siliceous sand (PA)	Fine siliceous sand (PA)	Quartzite mason sand (PA)
Fine aggregate content (kg/m^3)	752	732	732
Paste content (1-V_{agg})	0.70	0.71	0.70
Fiber content	157	157	157
Spread or flow (mm)	180	268	211
28-day strength (MPa)	129±3	143±2	144±5

3.1.2 Tensile strength and dispersion of fibers in the cross-section

Using the dog-bone setup, the first cracking tensile strength of UHPC = 8.52±0.2 MPa. To ensure that the fibers were uniformly distributed in the UHPC without segregation, an image processing sequence was developed in MATLAB to determine the homogeneous distribution of fibers in the cross-section. As seen in Figure 62, the process involved a 2-step conversion before the fiber distribution could be determined. First, a threshold is selected to represent the fiber fraction, and the rest of the image is considered a part of the matrix. Then this image is converted into a binary image where the fibers are white and the matrix is black in color.

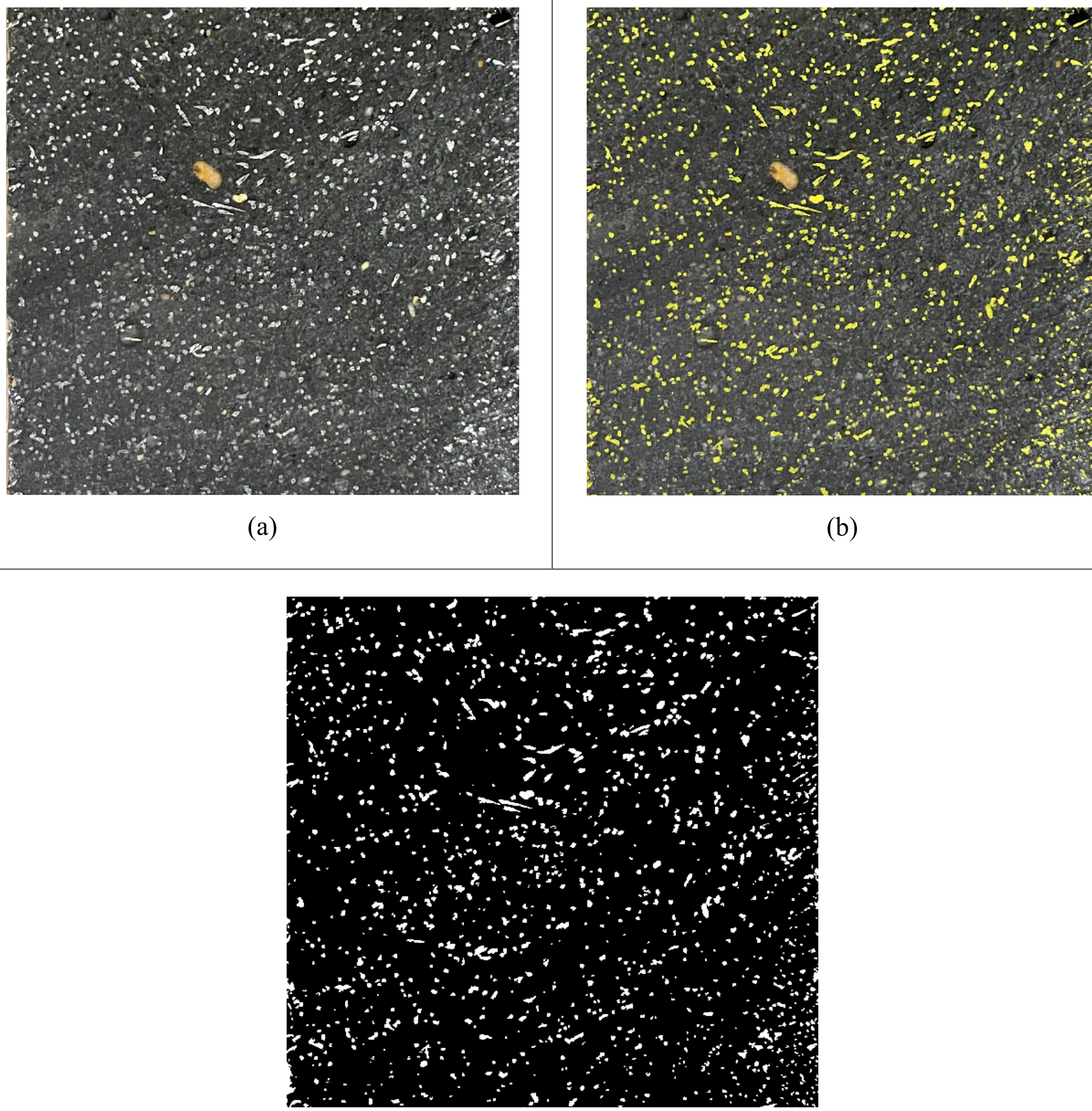

(a)

(b)

(c)

Figure 62. (a) Original image taken from the cross-section of the sliced UHPC prism, (b) image after segmentation, highlighting the fiber in yellow and the rest of the matrix unaltered, and (c) binary image considering the fiber as white and the rest of the matrix as black.

This binary image can theoretically be further processed via image analysis to determine the area distribution of fibers in the cross-section and to quantify the possible fiber segregation in extremely flowable mixtures.

3.2 FINITE ELEMENT MODELING OF UHPC BRIDGE CONNECTION

3.2.1 Background

With the development of various UHPC products to connect modular bridge components, experimental testing to assess the performance of these connections has become increasingly important. However, many times it is not practical to physically evaluate the behavior of various types of UHPC or rebar and geometric configurations of UHPC connections. Thus, research has looked at analytically simulating their response using finite element models (Nasrin and Ibrahim, 2018). For these models, their accuracy was highly dependent on the reliability of the parameters and models used within the finite element program. These models seek to capture the UHPC, regular concrete, steel reinforcement, and contact bond behavior between the materials. The commercial software ABAQUS was used for this research program because of its past use and ability to analyze composite structural systems, including UHPC bridge connections (Nasrin and Ibrahim, 2018).

3.2.2 Model Development

The finite modeling effort involved mimicking the test setup and results from the deck panel-UHPC connection specimens discussed in *Lap-Spliced Rebar Connections with UHPC Closures* by Haber and Graybeal (2018). These lab tests involved a commonly employed UHPC connection detail with dimensions generally following FHWA's recommendations shown in Haber and Graybeal (2018). These tests consisted of two identical prefabricated regular-strength reinforced concrete deck panels connected at the mid-span by a non-contact lap splice UHPC connection shown in Figure 63 (Haber and Graybeal, 2018).

The two regular concrete panels contained both transverse and longitudinal reinforcement. The longitudinal reinforcement running parallel with the span also acted as non-contact lap splices that overlapped the UHPC connection region. This configuration was tested in third-point bending, in which the loads were applied from the top at the opposite ends of the span and the supports were located at both sides of the middle-third of the span (Haber and Graybeal, 2018).

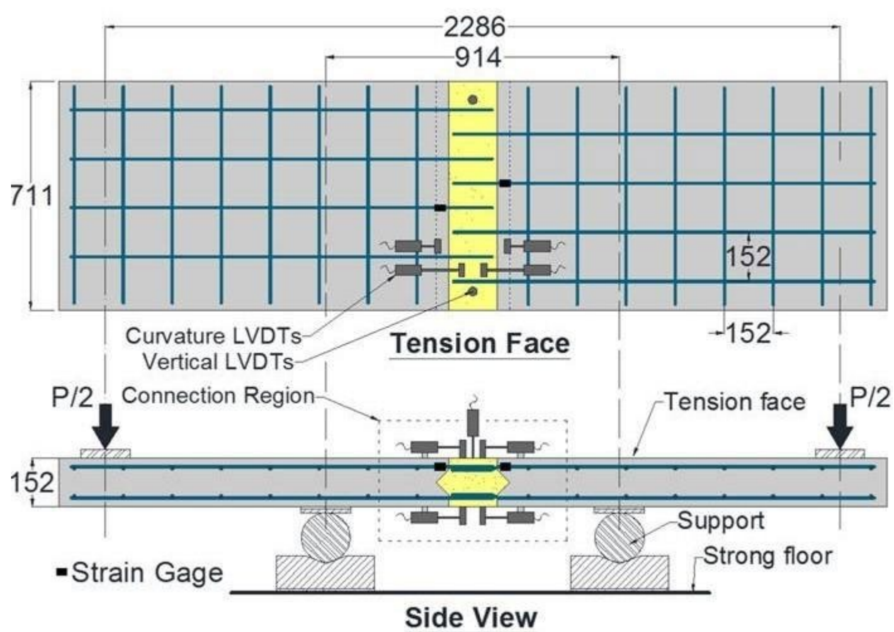

Figure 63. Physical lab testing setup of the UHPC connection tests (Haber and Graybeal, 2018).

The force-displacement data from initial loading to failure (ultimate) was recorded by Haber and Graybeal (2018) and was the subject of this finite element model. Five physical lab tests were conducted (U-A, U-B, U-C, U-D, U-E) by Haber and Graybeal and each specimen failed due to the crushing of the regular strength concrete (Haber and Graybeal, 2018). For computational convenience, the specimen "U-A" was simulated using its exact material and geometric properties for ease of comparison (Figure 64).

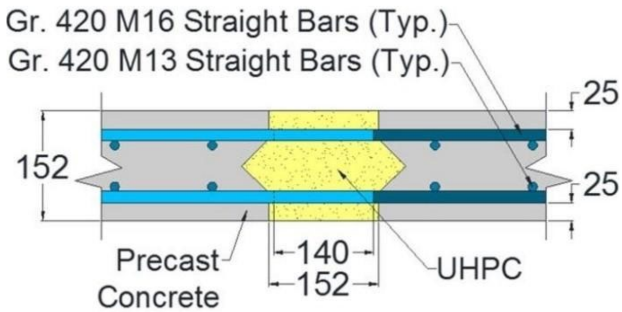

Figure 64. Physical UHPC connection specimen detail used in ABAQUS model (Haber and Graybeal, 2018).

3.2.3 Geometry

The entire third-dimensional geometry of all the components of the bridge connection test was essential for the ABAQUS model to match closely with the physical tests. The "U-A" specimen tested by Haber and Graybeal was identically matched within the finite element model with the information provided by the previous research (Haber and Graybeal, 2018). Additionally, this allowed for proper detailed loading of the model in third-point bending, as described in subsequent sections. The dimensions of the model are shown in Table 27 and Table 28. This information also matches Figure 63 and Figure 64 provided by Haber and Graybeal (2018).

Table 27. Geometric properties in millimeters used in the model for (a) precast regular concrete deck, (b) UHPC connection, (c) M16 (#5) longitudinal lap-splice rebar, and (d) M13 (#4) transverse rebar (Haber and Graybeal, 2018).

(a) Precast regular concrete deck

Length (mm)	1,074
Width (mm)	711
Height (mm)	152

(b) UHPC connection

Length (mm)	152
Width (mm)	711
Height (mm)	152

(c) M16 (#5) longitudinal lap-splice rebar

Length (mm)	1,214
Cross-Sectional Area (mm^2)	200

(d) M13 (#4) transverse rebar

Length (mm)	711
Cross-Sectional Area (mm^2)	129

Table 28. UHPC connection geometry used in ABAQUS model (Haber and Graybeal, 2018).

Yield Strength of Reinforcement (f_y) (MPa)0	Minimum Cover (c) (mm)	Embedment Length (l_d) (mm)	Lap Splice Length (l_s) (mm)	Maximum Clear Spacing between Adjacent Lap Spliced Bars (s) (mm)
420	$1.57d_b = 25$	$9.2d_b = 146$	$0.96l_d = 140$	$0.41l_d = 60$

3.2.4 Material Properties and Models

3.2.4.1 Concrete Modeling

To capture both the elastic and plastic behavior of concrete in compression and tension, the ABAQUS model was separated out into their respective behaviors. Information on the concrete's elastic modulus (E) and Poisson's ratio (ν) was specified to describe the material's behavior within the elastic region of loading. The concrete damage plasticity model was used to define the inelastic (plastic) behavior of concrete. The five main parameters used by ABAQUS for concrete damage plasticity are the dilation angle (ψ), eccentricity (ε), f_{b0}/f_{c0}, K, and the viscosity parameter. These parameters are ABAQUS standards and were defined within the program with values informed by recommendations from Nasrin and Ibrahim. The specific values for each parameter are seen in Table 29, Table 30, and Table 31 (Nasrin and Ibrahim, 2018).

For concrete damage plasticity modeling, corresponding stress and inelastic strain values were used to describe the concrete's uniaxial tensile and compressive behavior past its elastic region. This information was drawn from empirical equations used to describe the inelastic portion of both the compression and tension curve for a concrete with equivalent compressive strengths to the ones present in the model (Birtel and Mark, 2006). From the corresponding stress and inelastic strain values of the given concrete, compression and tension damage parameters by equations proposed from Birtel and Mark were calculated for each associated value of inelastic (crushing or cracking) strain and implemented in the ABAQUS model (Birtel and Mark, 2006).

Table 29. Regular concrete properties used in the model with references.

Compressive Strength (f'c) (MPa)	43	(Haber and Graybeal, 2018)
Elastic Modulus (E) (MPa)	21,083	(Nasrin and Ibrahim, 2018)
Poisson's Ratio (v)	0.18	(Nasrin and Ibrahim, 2018)
Mass Density (ton/mm^3)	2.4 E-09	(Nasrin and Ibrahim, 2018)

Table 30. UHPC properties used in the model.

Compressive Strength (f'c) (MPa)	174	(Haber and Graybeal, 2018)
Elastic Modulus (E) (MPa)	53,700	(Nasrin and Ibrahim, 2018)
Poisson's Ratio (v)	0.15	(Haber and Graybeal, 2018)
Mass Density (ton/mm^3)	2.56 E-09	(Nasrin and Ibrahim, 2018)

Table 31. Concrete damage plasticity parameters used in the model.

Dilation Angle (ψ)	35	(Nasrin and Ibrahim, 2018)
Eccentricity (ε)	0.1	(Nasrin and Ibrahim, 2018)
f_{b0}/f_{c0}	1.16	(Nasrin and Ibrahim, 2018)
K	0.667	(Nasrin and Ibrahim, 2018)
Viscosity Parameter	0	(Nasrin and Ibrahim, 2018)

3.2.4.2 Steel Rebar Modeling

Modeling of steel reinforcement within ABAQUS for both the regular concrete and UHPC was done using an elastic-perfectly plastic model. Similar to concrete, ABAQUS separates these mechanical models for steel into two parts: elastic and plastic. The primary parameters involved in the model were the elastic modulus (E), Poisson's ratio (v), and yield strength (f_y) of the rebar. Details on these properties are detailed in Table 32.

Table 32. Steel reinforcement properties.

Yield Strength (f_y) (MPa)	420	(Haber and Graybeal, 2018)
Elastic Modulus (E) (MPa)	200,000	(Nasrin and Ibrahim, 2018)
Poisson's Ratio (v)	0.3	(Nasrin and Ibrahim, 2018)
Mass Density (ton/mm^3)	7.85 E-09	(Nasrin and Ibrahim, 2018)

3.2.5 Contact Models

The model consisted of three primary materials: numerous steel reinforcement bars, two concrete slabs, and the UHPC connection. Contact modeling was essential to accurately capture the behavior between two surfaces in contact within the UHPC connection model. Two contact modeling methods between regular concrete and UHPC were available for use. Similarly, for steel and concrete two contact modeling methods were considered.

For concrete interfaces, the first method and most common method was creating a tie constraint between the surfaces. This contact modeling method acts as if there is a perfect bond between the two concrete surfaces. Alternatively, the second available method involved using an interaction definition between the concrete surfaces. This alternative modeling technique is referred to as a mechanical penalty friction model, in which an appropriate friction coefficient is specified to describe the bond performance between the two concrete surfaces (Nasrin and Ibrahim, 2018). The friction contact model allows for a varying degree of slip depending on the value of the friction coefficient. This information is typically obtained through experimental bond tests. Many researchers have proposed varying friction coefficients ranging from 0.44 to 1.50 depending on the surface interface conditions (Hussein et al., 2016; Semendary and Svecova, 2020; Zhang et al., 2020). The finite element modeling efforts by Nasrin and Ibrahim looked at the results of using a tie (perfect bond) contact model and a friction contact model using a friction coefficient of 1.09 proposed by Hussein et al. for mid-rough surfaces (Hussein et al., 2016; Nasrin and Ibrahim, 2018).

Similar to contact modeling between regular concrete and UHPC, two comparable options are available to describe the contact behavior between steel rebar and concrete. The first and most employed contact modeling method was using an embedded region constraint. This method assumed that there was a perfect bond between the steel reinforcement and the concrete surrounding it. Notably, this approach was utilized in the modeling efforts by Nasrin and Ibrahim (Nasrin and Ibrahim, 2018). The second way to model the contact behavior between reinforcement and concrete is by creating an interaction. However, deriving a friction coefficient that describes the full bond behavior of steel and concrete is difficult due to the multiple factors that contribute to the bond strength, including the bearing force of the reinforcement bar ribs, chemical adhesion, and friction force between the materials (Yuan and Graybeal, 2015). For regular concrete and steel reinforcement, Raous and Karray conducted rebar pull-out tests and attempted to describe the force-sliding (load-slip) relationship. This analysis used a friction coefficient of 0.45 to account for the entire bond strength of the rebar embedded in concrete (Raous and Karray, 2009). Based on the findings of Raous and Karray (2009), it was inferred that steel rebar and UHPC should have a larger associated friction coefficient to describe the superior bond performance of UHPC rebar compared to regular concrete rebar. However, the exact value of the friction coefficient is related to the load-slip relationship developed from rebar pull-out tests where the performance is a function of the embedment (development) length, lap splice length, bar spacing, bar diameter, bar yield strength, concrete side cover, and UHPC strength (Yuan and Graybeal, 2015).

3.2.6 Loading

The model was loaded until failure in third-point bending using the dynamic, explicit step option in ABAQUS. This analysis option allowed the specification of a set amount of deflection at the third-point loading locations and ensured loading up to ultimate. Two-point loads were applied at both ends of the middle third of the span. Similarly, two pinned supports resisting displacement in the global y-direction were applied at the opposite ends of the span. The model's loading configuration is illustrated in Figure 65.

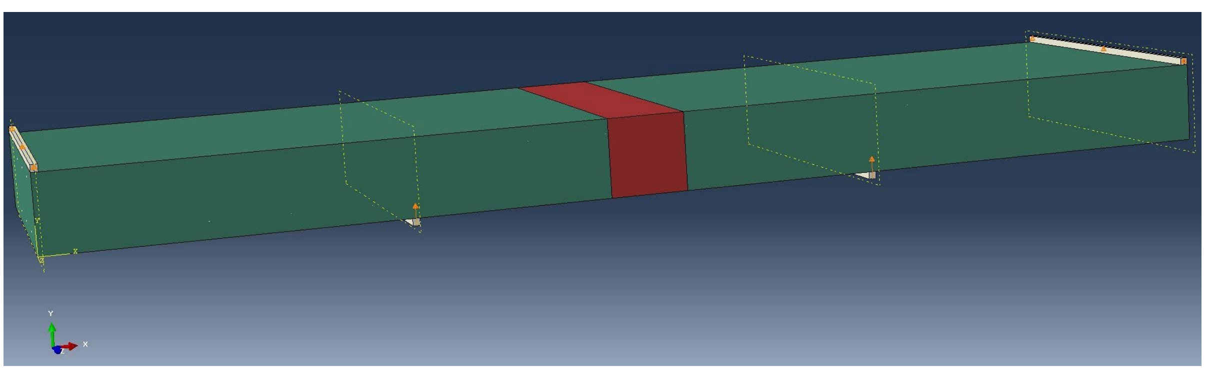

Figure 65. Loaded third-point bending model in ABAQUS.

3.2.7 Meshing and Elements

A mesh sensitivity study was conducted to assess whether a sufficiently fine mesh had been reached for the three-dimension analysis. A global mesh size from 50 to 15 mm was examined to determine a mesh size that would produce a minimal amount of "noise" for the moment/load versus displacement data. It was found that the maximum mesh size for this specific analysis was 15 mm. However, this mesh analysis size produced a computationally time-consuming exercise for the program when executed.

Hexagonal linear 3D stress elements (C3D8R), as shown in Figure 66, were used for all concrete materials and the loading plates. These elements were chosen due to the rectangular geometric nature of the model and to reduce the complexity of the simulation to save computational effort. For the reinforcement elements, a two-node linear 3D truss element (T3D2) was implemented per recommendations from Nasrin and Ibrahim (Nasrin and Ibrahim, 2018).

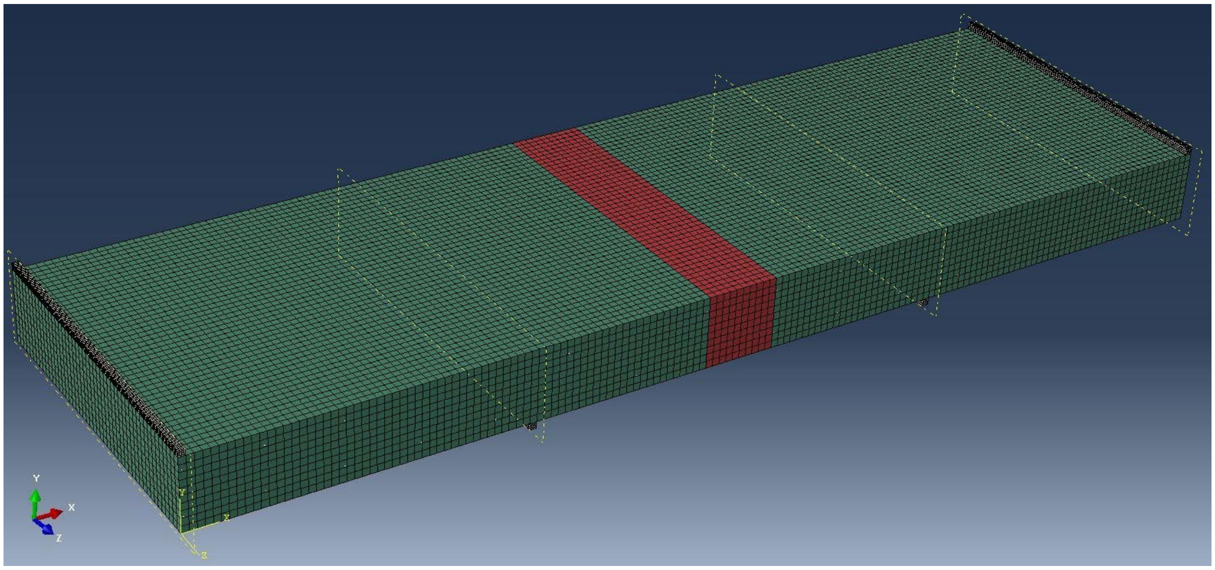

Figure 66. Meshing used in ABAQUS model.

3.2.8 Model Validation

The ABAQUS simulation was completed by loading the model until failure in third-point bending in an identical manner to the physical lab tests. During the simulation, the model's "loading step" was split up into 30 separate increments. This was done to obtain the needed output of forces, stresses, displacements, and cracking damage in the post-processing stage along the time loading history. Figure 67 through Figure 69 show the deflection along the time loading history for visualization purposes at the 0^{th} increment, 15^{th} increment, and 30^{th} increment.

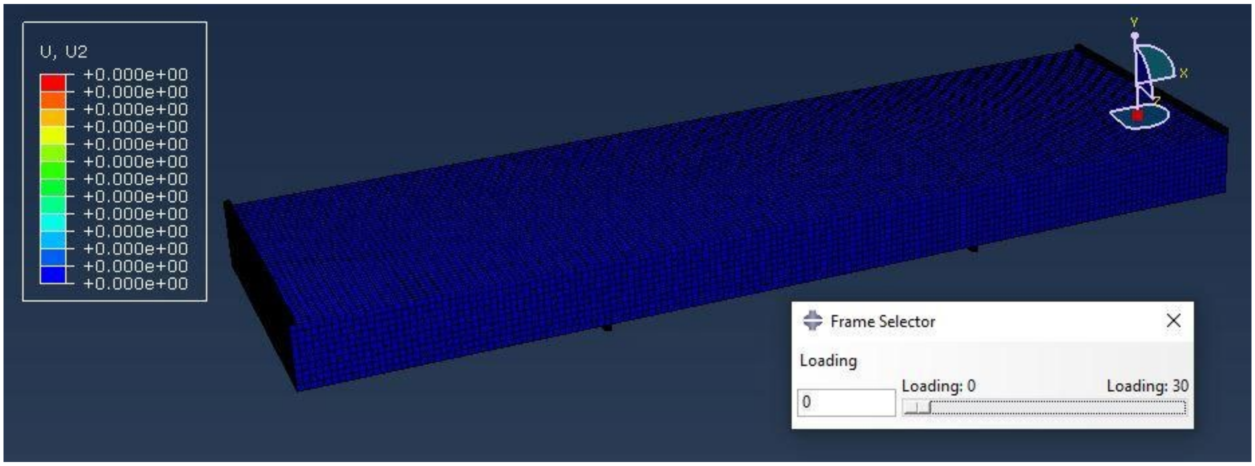

Figure 67. Deflection at the 0th increment of the time loading history.

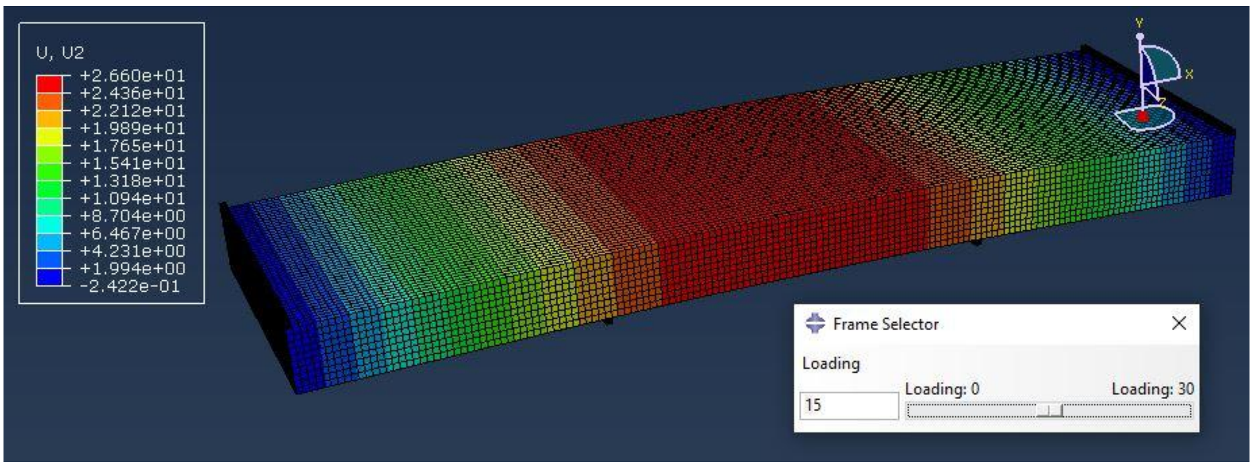

Figure 68. Deflection at the 15th increment of the time loading history.

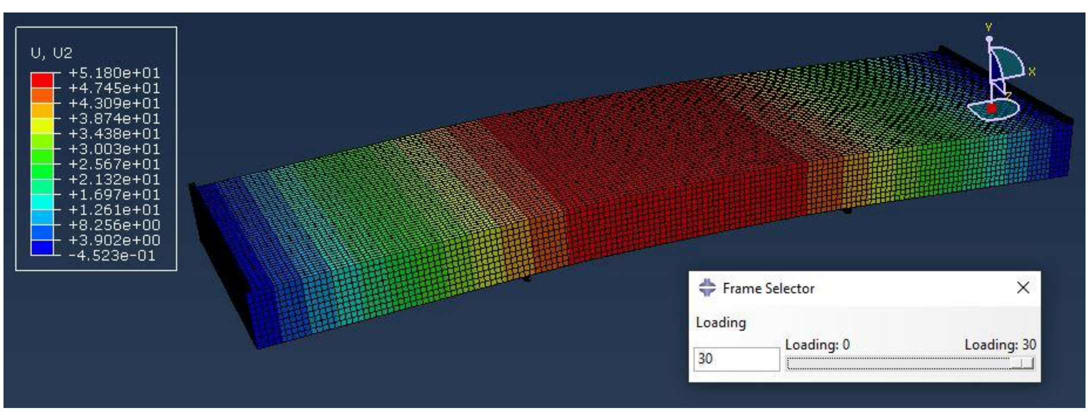

Figure 69. Deflection at the 30th increment of the time loading history.

The model was intended to accurately capture both the load-displacement behavior and the relative tensile crack patterns observed up until failure by Haber and Graybeal (2018). The testing data provided by Haber and Graybeal (2018) listed deflection at mid-span, applied load, and other associated information which is presented in subsequent sections (Haber and Graybeal, 2018). When the ABAQUS model was processed, data needed to be compiled for the applied load (reaction force) and the midspan displacement in the U2 (y-direction) at each of the 30 steps along the loading history. Additionally, concrete plasticity damage modeling was collected and compared to the crack patterns of the physical tests at ultimate.

3.2.9 Results and Discussion

The data available from the physical lab research by Haber and Graybeal (2018) were examined against the post processing results from the model to assess the accuracy of the analysis. First, the loaded behavior up to ultimate of the model was investigated in multiple approaches versus the data produced from the physical research conducted. From observations of the data compiled in Table 33, both the yield point and ultimate point of the model compared well to the physical lab test. The yield point produced from the model was approximately 12.0 mm, 116 kN compared to the physical test yield point of 13.2 mm, 106 kN (Haber and Graybeal, 2018). Additionally, the ultimate point produced from the model before failure was approximately 51.4 mm, 134 kN in comparison to the ultimate loading result for the lab test specimen U-A of 55.8 mm, 144 kN (Haber and Graybeal, 2018). These variations between the physical test and the model's analysis represent relatively small differences of less than 10 percent at these critical points along the time loading history (Table 33).

Table 33. Summary of results from ultimate loading between the physical specimen and the finite element model.

	Yield Point (Δ_y, P_y) (mm, kN)	Ultimate Point (Δ_u, P_u) (mm, kN)
Physical Lab Test (U-A)	(13.2, 106)	(51.4, 134)
Finite Element Model	(12.0, 116)	(55.8, 144)

Additionally, a moment-displacement chart was generated from the ABAQUS model's analysis from the full set of load-displacement data. The loading data of the model were assembled by analyzing the total reaction force at one support in ABAQUS and multiplying it by the third-point distance ("a") between the support and the adjacent applied load. The dimension "a" was a constant value equal to 0.686 m and is visually defined in Figure 70. This calculation was conducted for each loading increment until all 30 points were produced.

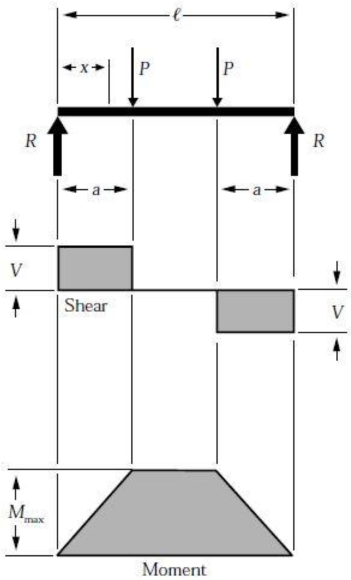

$$R = V \; \ldots\ldots\ldots\ldots \; = P$$

$$M_{max} \text{ (between loads)} \; \ldots\ldots \; = Pa$$

$$M_x \text{ (when } x < a) \; \ldots\ldots \; = Px$$

$$\Delta_{max} \text{ (at center)} \; \ldots\ldots \; = \frac{Pa}{24EI}(3\ell^2 - 4a^2)$$

$$\Delta_x \text{ (when } x < a) \; \ldots\ldots \; = \frac{Px}{6EI}(3\ell a - 3a^2 - x^2)$$

$$\Delta_x \left(\text{when } x > a \text{ and } < (\ell - a)\right) \; \ldots \; = \frac{Pa}{6EI}(3\ell x - 3x^2 - a^2)$$

Figure 70. Third-point loading diagram of a simply supported beam with two equally concentrated loads placed symmetrically (Hibbeler 2017).

The compiled moment-deflection data were organized and plotted against the physical lab test data in Figure 70. Both sets of data compare well to each other, with slight differences between the two. The finite element model within the elastic region of loading was relatively stiffer than the physical test. Additionally, the finite element model within the plastic region of loading produced relatively less strain hardening behavior than the physical lab tests. Overall, the data sets for the loading curve differed within 10 percent difference from each other.

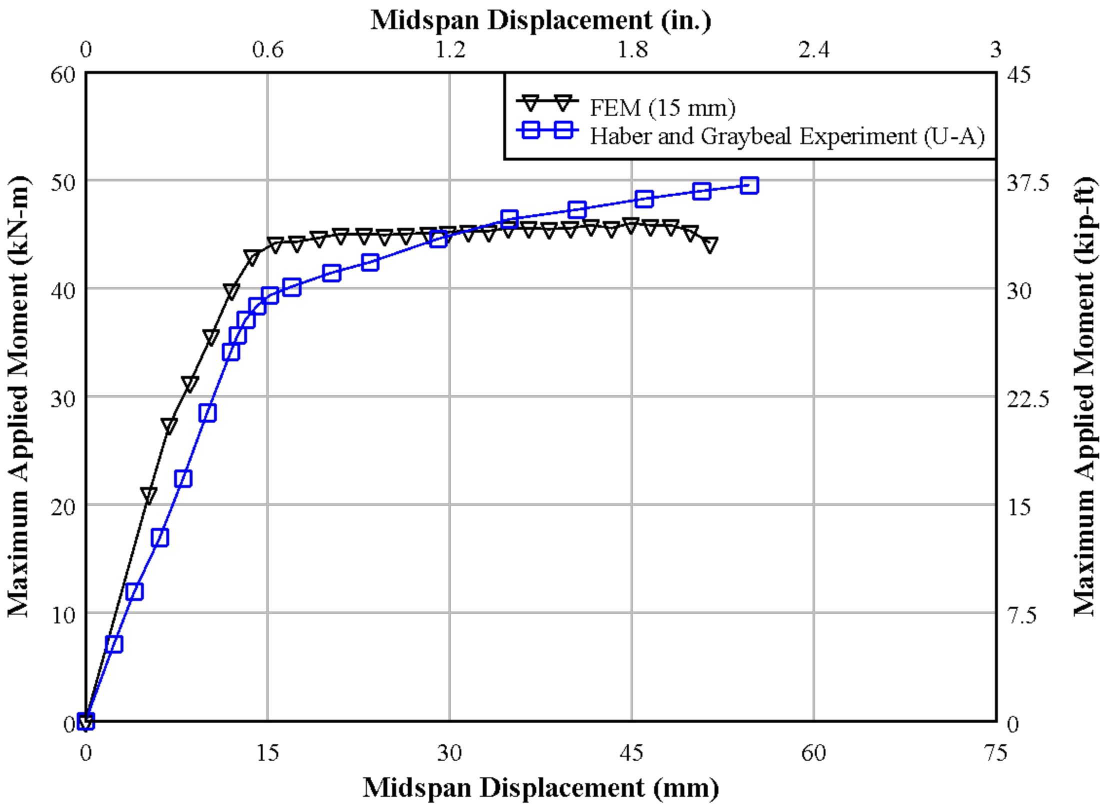

Figure 71. Applied moment versus mid-span displacement for the ABAQUS finite element model with comparison to the physically conducted lab tests by Haber and Graybeal (Haber and Graybeal, 2018).

The last point of comparison between the ABAQUS model and the physical specimen tests involved a visual qualitative inspection of the tensile cracking patterns after failure. These data were generated in ABAQUS through the concrete damage plasticity material modeling option for tensile damage. Figure 71 shows the model's cracking patterns on the tension face at the ultimate, 30th loading increment. Figure 73 was provided by Haber and Graybeal (2018) from their research and shows the cracking patterns from all of the physical specimens they tested. From visual observation between the model and physical tests, they appear to agree in both the concrete crack patterns and damage locations between the two.

Between the agreement of the quantitative load-displacement results and qualitative crack pattern results of the ABAQUS model and the physical tests, it was determined that the model performed satisfactorily. The results conclude that further geometric and material configurations of this type of structural system may be modeled with ABAQUS with varying levels of success depending on the amount of detail provided for the material and spatial properties of the system.

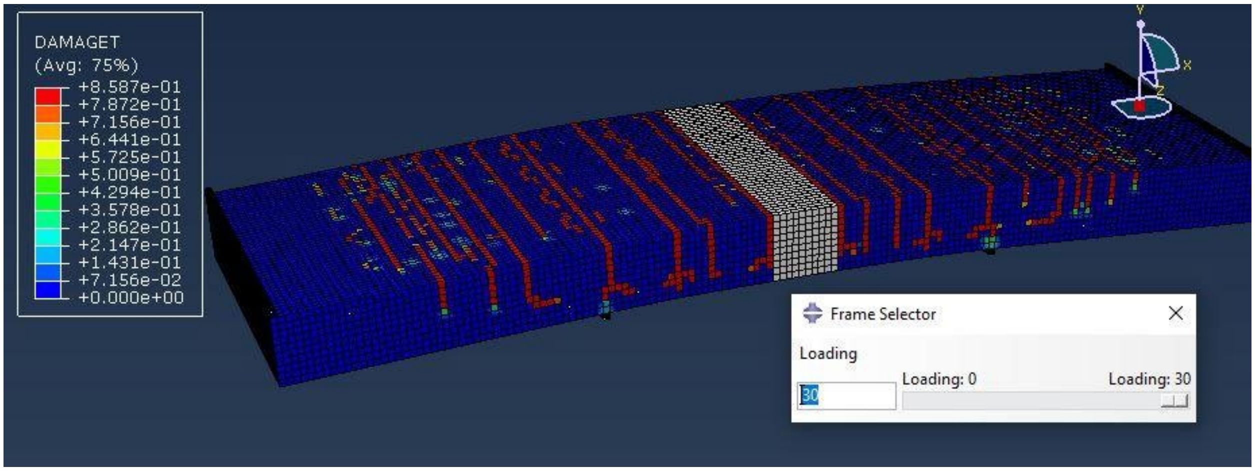

Figure 72. Concrete tensile cracking patterns in the ABAQUS finite element model.

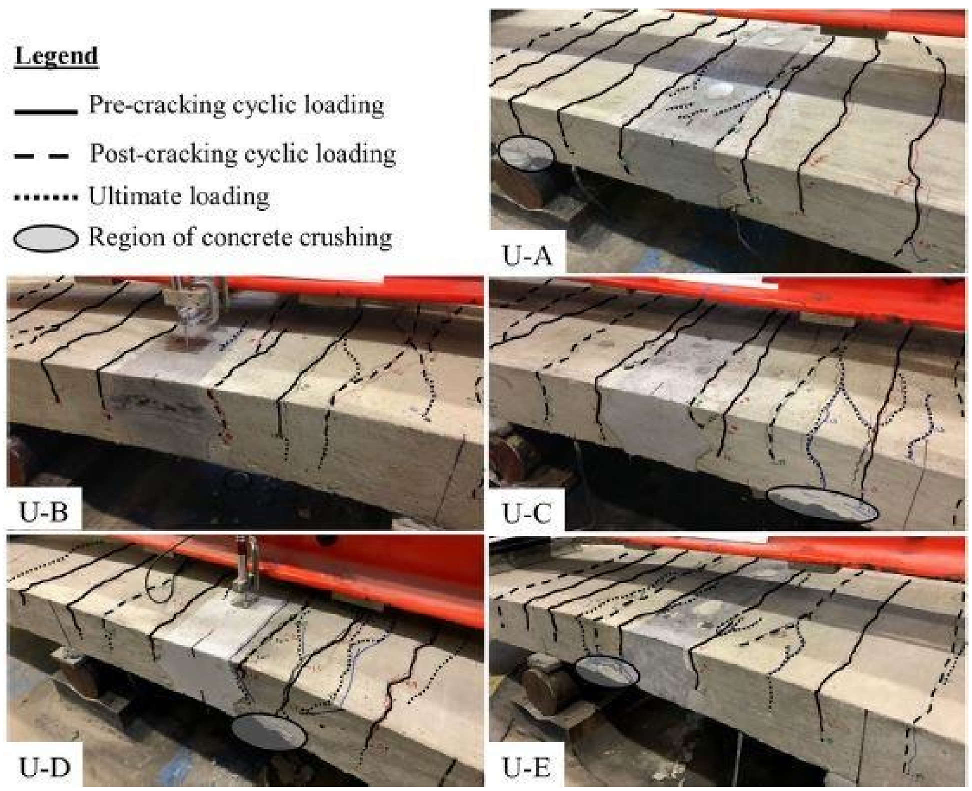

Figure 73. Tensile crack patterns observed from physical test specimens (Haber and Graybeal, 2018).

3.3 LIFE CYCLE COST ANALYSIS

3.3.1 Overview

The life cycle cost analysis (LCCA) aims to show how UHPC can be more cost-effective long-term than other materials, especially when used as overlays. The LCCA compares UHPC, conventional concrete, latex-modified concrete, and a non-proprietary UHPC mix designed by University of Delaware. Each material was analyzed based on a recent project that utilized UHPC in Delaware: Blackbird Bridge in Milford, completed in 2019. Although a smaller project, it had details readily available so that each material could be examined as though it was the overlay used on the project. This allowed a common component to compare each material—square footage of the project—using their respective materials prices and construction timelines. This analysis was performed using the Federal Highway Administration's RealCost software for overlays.

3.3.2 RealCost Software

3.3.2.1 Software Overview

The Federal Highway Administration created a lifecycle cost analysis software for use with project-level pavement design called RealCost (FHWA 2017). RealCost takes user inputs about a project and timeframe to calculate direct expenditures of the activities along with projected user costs that will stem from the project's work zone operations. RealCost compares design strategy alternatives inputted by the user and uses the technique of discounting to get an estimated agency and user cost. The analysis can then be examined by the user to determine which alternative is the most cost-effective for the project.

3.3.2.2 Input Parameters

RealCost involves many project inputs as well as inputs specific to each type of material being analyzed as a potential overlay. Project-level inputs include analysis options, traffic data, value of user time, hourly traffic distribution, added vehicle time and cost, and project details. Each material is input as an "alternative" and has its own alternative-level inputs. Most alternative-level inputs are entered in thousands of dollars, but for simplicity in this section, they will be referred to as their full dollar amount, not the smaller input value. Every input except for the discount rate and the annual growth rate of traffic were entered as normal distributions with a standard deviation of 1.5. Annual growth rate and discount rate stayed as deterministic inputs. After all the inputs listed in the next subsections were entered, a simulation was run with a reproducible seed value of 2,000, tail analysis percentiles of 5th, 10th, 90th, and 95th, and 2,000 iterations.

3.3.2.2.1 Project-Level Inputs

The basis for the project-level inputs come from UHPC. The analysis period was chosen to be 100 years to fully cover the expected lifespan of UHPC. Since the LCCA is based around the Blackbird Station Road bridge in Delaware, the analysis period begins in the year 2019, the year the project was completed. The bridge features traffic in both directions and the LCCA includes four alternatives (conventional concrete, UHPC, latex modified concrete, and a University of Delaware (UD) UHPC mix). The discount rate used was 4%, as various sources used values ranging from 3% to 5%. For the traffic data, an assumed average annual daily traffic (AADT) of 1,060 was pulled from DelDOT's "Vehicle Volume Summary (Traffic Counts)," where the AADT is listed for Blackbird Station Road, maintenance road number N463 (DelDOT 2019). The single unit trucks as a percent of AADT and combination trucks as a percent of AADT were 9.55% and 0%, respectively, and are from DelDOT's 2019 traffic counts (DelDOT 2019). The annual growth rate of traffic was estimated to be 2%. An increase of 1% in the number of licensed drivers, an increase of 3% in vehicle miles traveled, and an average value of 2% was used in the RealCost software. The normal speed limit for Blackbird Station Road is 40 mph, and there is one lane open in either direction. The maximum AADT for both directions is given as 1,700. RealCost uses the proportion of trucks and buses and the size of the roadway to calculate the free flow capacity, which turned out to be 1,995. Using a Google Maps measuring tool, it was estimated that the maximum queue length was 0.0206 miles. The traffic distribution was determined to be rural based on AADT and vehicle types on the road (DelDOT 2019). The queue dissipation capacity was calculated using an equation from CalTrans using a given base capacity of 1,800 pcphpl for a single-lane highway, the 9.55% of heavy vehicles, and a given passenger car equivalent of 1.5 for level terrain. The equation is: QC=(Q*100)/[100+P*(E-1)], where QC=queue dissipation capacity (vhphl), Q=base capacity (pcphpl)=1,800 pcphpl for single-lane highway, P=% of heavy vehicles, and E=passenger car equivalent (pc/heavy vehicle)=1.5 for level terrain. This comes out to a queue dissipation capacity of 1,718 vphpl. The next section of project-level inputs pertains to the value of user time. Using the 1996 numbers from the LCCA in Pavement Design, the values were adjusted to be in 2019 amounts with the use of an inflation calculator (Walls III, J. and Smith, M., 1998). To check that these values made sense, this method was also used to calculate 2010 values of user cost for the example of a prestressed concrete bridge with a 20-year service life in the *RealCost User Manual* (FHWA 2010). The last part of project-level inputs includes traffic hourly distribution and added vehicle time and cost. The traffic hourly distribution was changed to be that of DelDOT's values for all days for a rural road with group 7 traffic, instead of just weekdays or weekend values (DelDOT 2019). The only values changed from default in the added time and vehicle stopping costs were the cost escalations. Per the user manual, Consumer Price Index (CPI) values were used in calculations. The base year was kept as the default 200.8 base component CPI and base year 2011 while the current component CPI was updated to 324.5 for the year 2020, since 2020 data was readily available through the price index (U.S. Bureau of Labor Statistics 2020).

3.3.2.2.2 Alternative-Level Inputs

Alternative-level inputs are tailored to each "alternative" being analyzed in RealCost. In this case, each alternative is a different material as a potential overlay for the Blackbird Station Road bridge. Alternative one is UHPC overlay, alternative two is conventional concrete overlay, alternative three is latex-modified concrete overlay, and alternative four is a University of Delaware non-propriety UHPC mix overlay. Each alternative has specific inputs for its activity cost and service life as well as activity work zone inputs and work zone hours. There are some constants between all four alternatives. All have an estimated agency maintenance cost of $63,000, as MDOT estimates $35 per square foot to maintain overlay and Blackbird Station Road bridge is 1,800 square feet (50 ft by 36 ft of overlay). Also, all have the same work zone length of 0.1 miles, work zone capacity of 1,050 vphpl, work zone speed limit of 35 mph, 1 lane open in each direction during work zone, and use a base of "week day 1" data for the traffic hourly distribution. Work zone capacity was calculated using a CalTrans equation and their base numbers of base work zone capacity and passenger car equivalent along with the percent of heavy vehicles. The equations is as follows: WC=(W*100)/[100+P*(E-1)], where WC=work zone capacity (vhphl), W=base work zone capacity (pcphpl)=1,100 for two-lane highways, P=% of heavy vehicles, and E=passenger car equivalent (pc/heavy vehicle) =1.5 for level terrain. This means that the work zone capacity is estimated at 1,050 vphpl for all four alternatives. All alternatives have inbound and outbound work zone hours from 0 to 24, since this LCCA is based on a bridge overlay for a small bridge. Missouri DOT breaks down an LCCA case study into input data for conventional concrete, latex-modified concrete, and UHPC. In our LCCA, we used their values of re-overlay duration as input for work zone duration, using 7 days for conventional concrete and 6 days for latex modified and both UHPC mixes. Also, from their Table 7-3, are a range of values for the maintenance frequency of each material overlay. Using the low end of the estimates, conventional concrete had a frequency of 15 years, latex modified as 14 years, and both UHPC mixes as 21 years (Khayat, K. and Valipour, M., 2018). The activity service life for the UHPC mixes are 100 years, as it is claimed to be a maintenance-free solution for the next 100 years. Conventional concrete and latex-modified concrete have activity service lives of 40 years (Khayat and Valipour, 2018). The user work zone cost is automatically calculated in RealCost and can be added to each alternative. Latex-modified concrete had a user cost of \$236, while the other three alternatives had a user cost of \$240. Perhaps the most important value for alternative-level inputs is the agency construction cost. Again, using values from Table 7-3 of Missouri DOT's case study data, we can determine the price of each alternative. ***For UHPC***: 1,800 ft.^{2} * (\$30/ft.^{2}) =\$54,000; \$54,000 * 2 in. thick overlay = \$108,000. ***For LMC***: 1,800 ft.^{2} * (\$39/ft.^{2}) = \$70,200; \$70,200 * 2 in. thick overlay = \$140,000. ***For CC***: 1,800 ft.^{2} * (\$12.65/ft.^{2}) = \$22,770; \$22,770 * 2.5 in. thick overlay = \$56,925. For ***UD's UHPC mix:*** price/yd^3 is \$1319 and 1 yd^3 = 27 ft^3. Therefore, the price/ft^3 is \$48.85/ft^3 would, making the cost \$13.36/ft^2. Thus, 1,800 ft.^{2} * (\$13.36/ft.^{2}) = \$24,048. \$24,048 * 2 in. thick overlay = \$48,096 (Khayat and Valipour, 2018).

3.3.3 Results

The deterministic results show both the cost to the agency and to the user for each alternative considered as an overlay on Blackbird Station Road bridge. Alternative 1 is UHPC, alternative 2 is conventional concrete, alternative 3 is latex modified concrete, and alternative 4 is the UD UHPC mix. Since the inputs are in thousands of dollars, the user costs are small values that do not show up adequately on the y-axis but can be read from Table 34.

Table 34. Agency and user cost for different alternatives.

Total Cost	Alt. 1	Alt. 1	Alt. 2	Alt. 2	Alt. 3	Alt. 3	Alt. 4	Alt. 4
	Agency Cost (\$1,000)	User Cost (\$1,000)	Agency Cost (\$1,000)	User Cost (\$1,000)	Agency Cost (\$1,000)	User Cost (\$1,000)	Agency Cost (\$1,000)	User Cost (\$1,000)
Undis-counted Sum	\$360.00	\$0.24	\$182.93	\$0.28	\$266.40	\$0.24	\$300.00	\$0.24
Present Value	\$155.44	\$0.24	\$111.34	\$0.28	\$197.79	\$0.24	\$95.44	\$0.24
EUAC	\$6.34	\$0.01	\$4.54	\$0.01	\$8.07	\$0.01	\$3.89	\$0.01

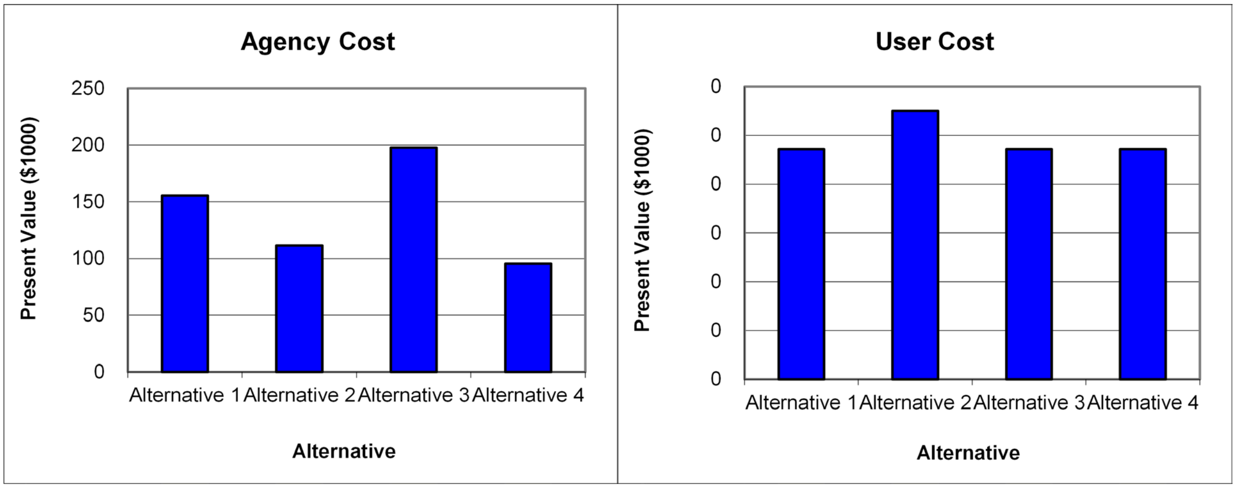

Figure ***74. Agency and user cost for different alternatives.***

The probabilistic results show agency and user cost probabilities for each alternative. These results consider the inputs that were set up as normal distributions with standard deviations of 1.5, and specific output statistical data can be viewed in Table 35.

Table 35. Agency and user cost statistical data for different alternatives.

Total Cost (Present Value)	Alt. 1	Alt. 1	Alt. 2	Alt. 2	Alt. 3	Alt. 3	Alt. 4	Alt. 4
	Agency Cost ($1000)	User Cost ($1000)	Agency Cost ($1000)	User Cost ($1000)	Agency Cost ($1000)	User Cost ($1000)	Agency Cost ($1000)	User Cost ($1000)
Mean	$155.98	$0.24	$113.49	$0.28	$202.33	$0.24	$96.08	$0.24
Standard Deviation	$5.64	$0.06	$8.93	$0.06	$11.25	$0.06	$5.49	$0.06
Minimum	$140.98	$0.05	$80.77	$0.09	$168.67	$0.02	$79.29	$0.02
Maximum	$180.90	$0.42	$161.06	$0.52	$253.45	$0.44	$117.93	$0.50

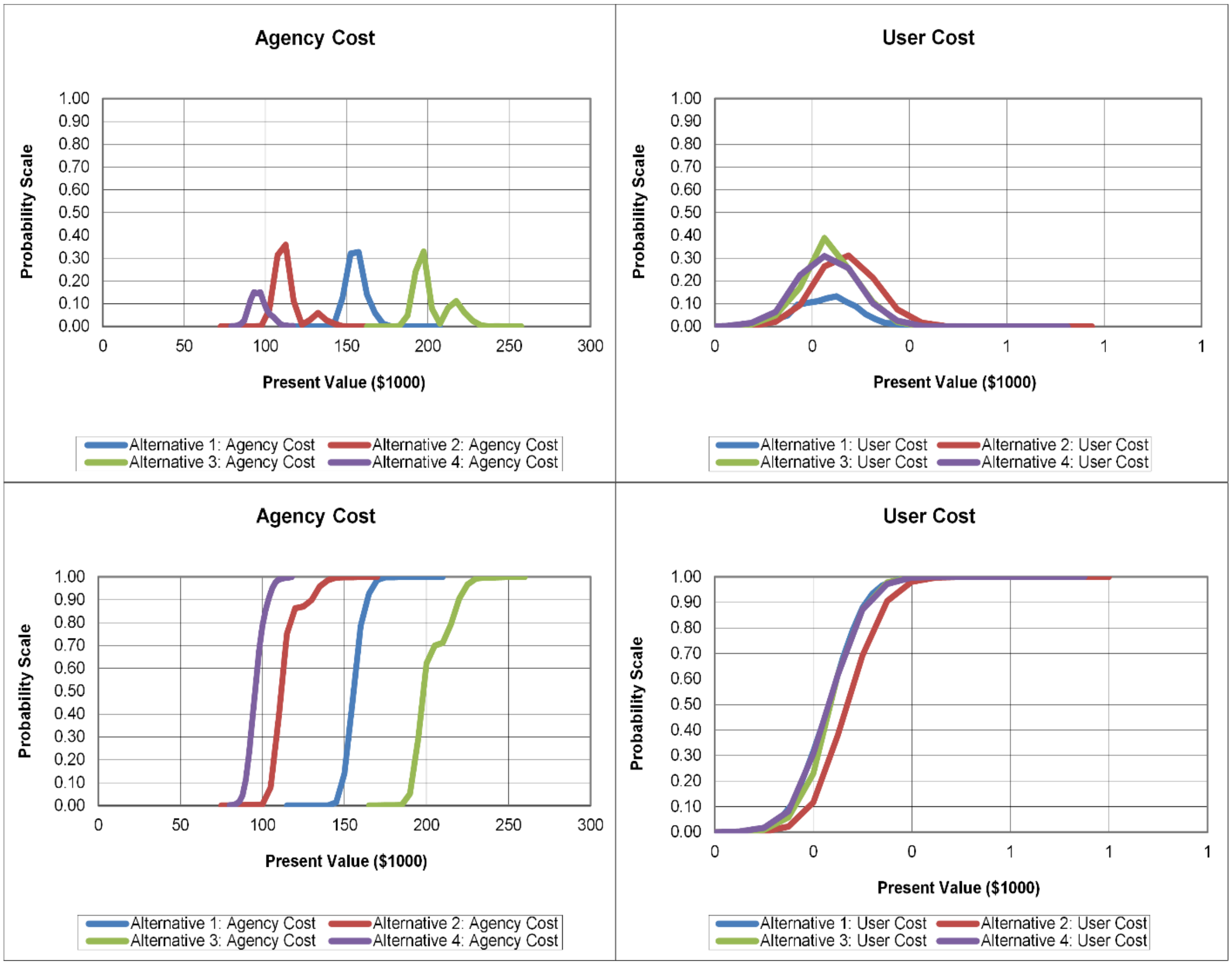

Figure 75. Agency and user cost probabilities for each alternative.

3.3.4 Discussion

In the deterministic results, UD's non-proprietary UHPC mix is the lowest cost to the agency and shares a user cost with UHPC and latex-modified concrete. The user costs do not seem to differ much and are the same for three of the four alternatives. This is most likely due to the similarities in their work zone inputs and the small size of the Blackbird Station Road bridge for which this is based. Latex-modified concrete (LMC) offers the second lowest cost to the agency but the highest user cost, while conventional concrete costs the highest for the agency and is tied for the lowest to the user. Both UHPC mixes (proprietary and non-proprietary) offer middle-of-the-road values for both the agency and the user, with the non-proprietary mix costing the least to the agency out of any alternative. This is due to the accelerated construction time that comes with UHPC, even though it can be associated with a higher upfront cost. The higher upfront costs coupled with a lower maintenance frequency over a longer lifespan than conventional concrete adds to the benefits of using UHPC as overlay material.

In the probabilistic results, the same pattern shows for the agency and user cost graphs. The non-proprietary UHPC mix has the highest probability of being the lowest cost to the agency. Proprietary UHPC has the highest probability of being the second most expensive cost to the agency, although latex-modified concrete, non-proprietary UHPC, and itself are all about the same probability for user cost while conventional concrete is more likely to be slightly higher. Latex-modified concrete has the highest probability of costing the agency the most, despite it having a comparable user cost to the UHPC mixes.

Again, these results show that the UHPC mixes would be the best material for both the agency and user considering the cost against the long lifespan of the material with minimal maintenance.

3.3.5 Summary and Future Work

Although analyzed based on a small-scale project, UHPC could prove to be the best material for overlays. More can be done to analyze UHPC as a repair material and another LCCA using RealCost could be done based on a larger-scale project. Either UHPC mix has a high upfront cost due to the materials involved, but it offers a shorter construction time that benefits both the agency and the user. It also does not require as thick of an overlay as conventional concrete, thus saving on the dead load of a project. The longer service life and lower maintenance frequency of UHPC allow it to be a longer-lasting pavement that could greatly benefit projects that may be harder to access or have high amounts of daily users.

Chapter 4

Recommendations

An experimental investigation was conducted to assess the material performance of a proprietary and non-proprietary UHPC mix specifically as it pertained to connection performance. The four critical tests were fresh property flow testing, compression testing (cubes and cylinders), prism flexural tensile testing, and rebar pull-out testing. All four tests were executed to observe and compare the primary performance gauges of UHPC as a structural connection material. The results showed that a close pull-out response was achieved although the flow, compressive, and tensile responses were not identical between the proprietary and non-proprietary mixes. As such, the following recommendations can be made when considering non-proprietary UHPC mix designs:

- Use FHWA connection guidelines (considering geometric and material properties as well) for steel rebar in non-contact, lap-splice connections to enable adequate structural response.
- Provide minimum development length per FHWA guidelines to achieve adequate bond with minimal slip, which was also verified via pull-out experimental tests and replicated in the finite element modeling efforts.
- Finite element models should include a contact model element to capture the interaction between the rebar and constituent materials.

FHWA EDC-3 (2015) provides a considerable number of resources that have been devoted to UHPC research on the academic, state, and federal level. The research conducted at the University of Delaware and The Pennsylvania State University for this project served to provide a thorough overview on previous impactful research projects while also elaborating and expanding on previous work. This research project was significant because both a proprietary and non-proprietary UHPC mix were laboratory tested using processes to quantify key material performance indicators. The program also highlighted essential material tests to define and categorize UHPC cementitious mixes used for bridge connections. Notably, the research found that rebar pull-out experimental testing performed adequately for both the proprietary and non-proprietary mix when detailed with

Dimensions and minimum UHPC strength and steel fiber quantity in conjunction with minimum development length, lap splice length, rebar cover, and clear space between rebar recommended by the FHWA. However, this research showed that conducting rebar pull-out tests provides the best indicator on how a particular UHPC mixture will perform in a non-contact, lap-splice connection commonly employed in highway bridge construction.

References

AASHTO T363 (2017). *Standard Method of Test for Evaluating Stress Development and Cracking Potential due to Restrained Volume Change Using a Dual Ring Test,* AASHTO.

Abbas, S., Nehdi, M. L., & Saleem, M. A. (2016). Ultra-High Performance Concrete: Mechanical Performance, Durability, Sustainability and Implementation Challenges. *International Journal of Concrete Structures and Materials*, 10(3), 271–295. https://doi.org/10.1007/s40069-016-0157-4

ACI Committee 239, *Ultra-high-performance concrete: An emerging technology report* (ACI 239R-18), n.d.

Ahlborn, T.M., E.J. Peuse, D.L. Misson, M.T. (2008). *Ultra-high-performance concrete for Michigan bridges, material performance: Phase I*. Michigan DOT, MDOT RC-1525.

Arora, A., M. Aguayo, H. Hansen, C. Castro, E. Federspiel, B. Mobasher, N. Neithalath (2018). Microstructural packing- and rheology-based binder selection and characterization for Ultra-high Performance Concrete (UHPC), *Cement and Concrete Research*, 103. doi:https://doi.org/10.1016/j.cemconres.2017.10.013.

ASTM (2017). *Standard Practice for Fabricating and Testing Specimens of Ultra-High Performance Concrete*, ASTM International. doi:10.1520/C1856.

ASTM (2021). *Standard Test Method for Compressive Strength of Cylindrical Concrete Specimens*, ASTM C39/C39M-21.

Azmee, N.M., N. Shafiq (2018). Ultra-high performance concrete: From fundamental to applications, *Case Studies in Construction Materials*, 9. doi:10.1016/J.CSCM.2018.E00197.

Baghaee Moghaddam, T., H. Baaj (2018). Application of compressible packing model for optimization of asphalt concrete mix design, *Construction and Building Materials*, 159 (2018). doi:10.1016/J.CONBUILDMAT.2017.11.004.

Brühwiler, E. (2016). "Structural UHPFRC": Welcome to the post-concrete era!, in: *Proceedings of First International Interactive Symposium on UHPC - 2016*, Des Moines. doi:10.21838/uhpc.2016.key.

Carbonell Muñoz, M.A., D.K. Harris, T.M. Ahlborn, D.C. Froster (2014). Bond performance between ultrahigh-performance concrete and normal-strength concrete, *Journal of Materials in Civil Engineering*, 26. doi:10.1061/(ASCE)MT.1943-5533.0000890.

Chen, Y., F. Matalkah, P. Soroushian, R. Weerasiri, A. Balachandra (2019). Optimization of ultra-high performance concrete, quantification of characteristic features, *Cogent Engineering*, 6 (2019). doi:10.1080/23311916.2018.1558696.

Courtial, M., M.N. de Noirfontaine, F. Dunstetter, M. Signes-Frehel, P. Mounanga, K. Cherkaoui, A. Khelidj (2013). Effect of polycarboxylate and crushed quartz in UHPC: Microstructural investigation, *Construction and Building Materials*, 44. doi:10.1016/j.conbuildmat.2013.03.077.

de Larrard, F. (1999). *Concrete mixture proportioning: A scientific approach*, E & FN Spon.

de Larrard, F., T. Sedran (1994). Optimization of ultra-high-performance concrete by the use of a packing model, *Cement and Concrete Research*, 24. doi:10.1016/0008-8846(94)90022-1.

DelDOT (2019). Replacement of Bridge 1-438 on Blackbird Station Road, Ultra-High Performance Concrete Connections and Deck Overlay. Available at https://www.fhwa.dot.gov/bridge/abc/docs/Blackbird-Station-Road_casestudy.pdf.

Dennis, T. (2022). *Optimized Performance of Ultra-High Performance Concrete Bridge Connections*, Master's Thesis. University of Delaware.

Dils, J., Boel, V., de Schutter, G. (2015). Vacuum mixing technology to improve the mechanical properties of ultra-high performance concrete, *Materials and Structures*, 48. doi:10.1617/s11527-014-0416-2.

El-Tawil, S., Alkaysi, M., Naaman, A.E., Hansen, W., & Liu, Z. (2016). *Development, Characterization and Applications of a Non-Proprietary Ultra High Performance Concrete for Highway Bridges*, USDOT Report No. RC-1637.

Fehling, E., M. Schmidt, J.C. Walraven, T. Leutbecher, S. Fröhlich (2014). *Ultra-high performance concrete UHPC: Fundamentals, design, examples*, Ernst & Sohn.

Feys, D., K.H. Khayat (2015). Comparing Rheological Properties of SCC Obtained with the ConTec and ICAR Rheometers, in: *Proceedings of the Fifth North American Conference on the Design and Use of Self-Consolidating Concrete*, Chicago, Illinois, USA, May 12–15, 2013, Chicago. https://www.researchgate.net/publication/311994191_Comparing_Rheological_Properties_of_SCC_Obtained_with_the_ConTec_and_ICAR_Rheometers (accessed August 5, 2019).

FHWA (2017). Life-Cycle Cost Analysis Software (Realcost). Available at: https://www.fhwa.dot.gov/infrastructure/asstmgmt/lccasoft.cfm

FHWA (2018). *Design and Construction of Field-Cast UHPC Connections* (FHWA-HRT-19-011). Available at: https://www.fhwa.dot.gov/publications/research/infrastructure/structures/bridge/uhpc/19011/index.cfm.

FHWA (2019). *North American Deployments of UHPC in Highway Bridge Construction*. Available at: https://highways.dot.gov/research/structures/ultra-high-performance-concrete/deployments.

FHWA (2020) LTBP Info Bridge: Data. Available at: https://infobridge.fhwa.dot.gov/Data.

Graybeal, B. (2018). *Properties and Behavior of UHPC-Class Materials*, https://www.fhwa.dot.gov/publications/research/infrastructure/structures/bridge/18036/18036.pdf (accessed June 22, 2019).

Graybeal, B., F. Baby (2019). *Tension Testing of Ultra-High Performance Concrete*, FHWA-HRT-17-053.

Graybeal, B., and Z. Haber (2018). *Ultra-High Performance Concrete for Bridge Deck Overlays*, FHWA-HRT-17-097.

Haber, Z., & Graybeal, B. (2018). Lap-Spliced Rebar Connections with UHPC Closures. *Journal of Bridge Engineering*, 23(6), 12. https://ascelibrary.org/doi/10.1061/%28ASCE%29BE.1943-5592.0001239

Haber, Z.B., Jose F. Munoz (2017). *Field Testing of an Ultra-High Performance Concrete Overlay*, FHWA-HRT-17-096.

Hibbeler, RC (2017). *Structural Analysis.* Pearson Prentice Hall.

Hofinger, I., Matthias, O., Hans-Achim, B., Swain, M. (1998). Modified four-point bending specimen for determining the interface fracture energy for thin, brittle layers. *International Journal of Fracture*, 92(3).

Huang, W., H. Kazemi-Kamyab, W. Sun, K. Scrivener (2017). Effect of cement substitution by limestone on the hydration and microstructural development of ultra-high performance concrete (UHPC), *Cement and Concrete Composites*, 77 (2017). doi:10.1016/j.cemconcomp.2016.12.009.

Júlio, Eduardo N.B.S., Fernando A.B. Branco, Vítor D. Silva (2004). Concrete-to-concrete bond strength: Influence of the roughness of the substrate surface, *Construction and Building Materials*, 18(9):675-681, ISSN 0950-0618, https://doi.org/10.1016/j.conbuildmat.2004.04.023.

Kahl, S. (2018). Commercial Production of Non-Proprietary Ultra-High Performance Concrete, USDOR Report No. RC-1670.

Katzer, L. (2006). Steel fibers and steel fiber reinforced concrete in civil engineering, *Pacific Journal of Science and Technology*, 7.

Khayat, K., and M. Valipour (2018). *Design and performance of cost-effective ultra high performance concrete for bridge deck overlays*. MoDOT Report cmr18-006. Available at: dot_36265_DS1.pdf.

Kim, D.J., S.H. Park, G.S. Ryu, K.T. Koh (2011). Comparative flexural behavior of Hybrid Ultra High Performance Fiber Reinforced Concrete with different macro fibers, *Construction and Building Materials*, 25 (2011). doi:10.1016/j.conbuildmat.2011.04.051.

Krauss, P., J. Elstner, A.A. Hanna (2009). *Guidelines for Selection of Bridge Deck Overlays, Sealers and Treatments*, NCHRP Project 20-07, Task 234.

Kumar, D., Ragalwar, K., Williams, B. A., & Ranade, R. (2020). Influence of maximum aggregate size and distribution modulus on UHPC matrix properties. *5th International Symposium: Ultra-High Performance Concrete and High Performance Construction Materials*, March 11-13, 3–4.

Li. Z., Rangaraju, P.R. (2016). Effect of Surface Roughness on the Bond Between Ultrahigh-Performance and Precast Concrete in Bridge Deck Connections. *Transportation Research Record*, 2577(1):88-96. doi:10.3141/2577-11

Li, P.P., Q.L. Yu, H.J.H. Brouwers (2018). Effect of coarse basalt aggregates on the properties of Ultra-high Performance Concrete (UHPC), *Construction and Building Materials*, 170. doi:10.1016/j.conbuildmat.2018.03.109.

Mehdipour, I., K.H. Khayat (2018). Understanding the role of particle packing characteristics in rheo-physical properties of cementitious suspensions: A literature review, *Construction and Building Materials*, 161, 340-353. doi:10.1016/j.conbuildmat.2017.11.147.

Meng, W., K.H. Khayat (2018). Effect of hybrid fibers on fresh properties, mechanical properties, and autogenous shrinkage of cost-effective UHPC, *Journal of Materials in Civil Engineering*, 30, 1–8. doi:10.1061/(ASCE)MT.1943-5533.0002212.

Newtson, C. and Weldon, B. (2018). *Bridge Deck Overlays using Ultra-High Performance Concrete*, Tran-SET Project No. 17CNMS01. Available at: https://digitalcommons.lsu.edu/transet_pubs/8/.

Piekarczyk, A., & Łaźniewska-Piekarczyk, B. (2021). Impact of Self-Compacting Concrete Admixtures on Frost Resistance and Compressive Strength-Commensurability of Frost Resistance Criteria. *Materials* (Basel, Switzerland), 14(11), 2922. https://doi.org/10.3390/ma14112922

Pyo, S., H.-K. Kim, B.Y. Lee (2017). Effects of coarser fine aggregate on tensile properties of ultra high performance concrete, *Cement and Concrete Composites*, 84 (2017). doi:10.1016/J.CEMCONCOMP.2017.08.014.

Russell, H. and Graybeal, B. (2013). *Ultra-High Performance Concrete: A state-of-the-art report for the bridge community*. Report No. FHWA-HRT-13-060. Available at: https://www.fhwa.dot.gov/publications/research/infrastructure/structures/hpc/13060/.

Santos, P.M.D., Ju, E.N.B.S. and Silva, D. (2007), Correlation between concrete-to-concrete bond strength and the roughness of the substrate surface, *Construction and Building Materials*, 21, 1688-1695. https://doi.org/10.1016/j.conbuildmat.2006.05.044.

Shi, C., D. Wang, L. Wu, Z. Wu (2015). The hydration and microstructure of ultra high-strength concrete with cement-silica fume-slag binder, *Cement and Concrete Composites*, 61. doi:10.1016/j.cemconcomp.2015.04.013.

Shi, C., Z. Wu, J. Xiao, D. Wang, Z. Huang, Z. Fang (2015). A review on ultra high performance concrete: Part I. Raw materials and mixture design, *Construction and Building Materials,* 101. doi:10.1016/j.conbuildmat.2015.10.088.

Tayeh, B., Abu Bakar, B.H., Johari, M., and Voo, Y.L. (2013). Mechanical and permeability properties of the interface between normal concrete substrate and ultra high performance fiber concrete overlay. *Construction and Building Materials*, 36: 538-549.

doi:10.1016/J.CONBUILDMAT.2017.11.147.

U.S. Bureau of Labor Statistics (2020). Available at: https://www.bls.gov/.

Walls, J. and M.R. Smith (1998). Life-cycle cost analysis in pavement design-interim technical bulletin. FHWA-SA-98-079. Available at: https://www.fhwa.dot.gov/infrastructure/asstmgmt/013017.pdf.

Wibowo, H. and S. Sritharan (2018). *Use of Ultra-High-Performance Concrete for Bridge Deck Overlays*, IHRB Project TR-683.

Wille, K. (2013). *Development of Non-Proprietary Ultra-High Performance Concrete for Use in the Highway Bridge Sector*, FHWA-HRT-13-100. 59. www.fhwa.dot.gov/research

Wille, K., A.E. Naaman, G.J. Parra-Montesinos (2011). Ultra-high performance concrete with compressive strength exceeding 150 MPa (22 ksi): A simpler way, *ACI Materials Journal*, 108. doi:10.14359/51664215.

Wille, K., C. Boisvert-Cotulio (2015). Material efficiency in the design of ultra-high performance concrete, *Construction and Building Materials*, 86. doi:10.1016/j.conbuildmat.2015.03.087.

Wu, Z., K.H. Khayat, C. Shi (2019). Changes in rheology and mechanical properties of ultra-high performance concrete with silica fume content, *Cement and Concrete Research*, 123. doi:10.1016/j.cemconres.2019.105786.

Xie, T., C. Fang, M.S. Mohamad Ali, P. Visintin Characterizations of autogenous and drying shrinkage of ultra-high performance concrete (UHPC): An experimental study, *Cement and Concrete Composites*, 91:156–173. doi:10.1016/j.cemconcomp.2018.05.009.

Yin, Y., Yanmin Qiao, Shaowei Hu (2019). Four-point bending tests for the fracture properties of concrete, *Engineering Fracture Mechanics*, 211: 371-381.

Yu, R., P. Spiesz, H.J.H. Brouwers (2015). Development of an eco-friendly Ultra-High Performance Concrete (UHPC) with efficient cement and mineral admixtures uses, *Cement and Concrete Composites*, 55, 383-394. doi:10.1016/j.cemconcomp.2014.09.024.

Zanotti, C. and Banthia, N. (2016). Modified Slant Shear Cylinder (MSSC) Test for Inherent Characterization of Bond in Concrete Repairs. *Indian Concrete Journal*, 90(8).

Zhang, L., Miao, X., Kong, X., & Zhou, S. (2019). Retardation effect of PCE superplasticizers with different architectures and their impacts on early strength of cement mortar. *Cement and Concrete Composites*, 104(May), 103369. https://doi.org/10.1016/j.cemconcomp.2019.103369

Zhou, Z., & Qiao, P. (2018). Direct tension test for characterization of tensile behavior of ultra-high performance concrete. *Journal of Testing and Evaluation*, 48(4). https://doi.org/10.1520/JTE20170644